Review Article

Anisotropic nanomaterials: structure, growth, assembly, and functions

Panikkanvalappil R. Sajanlal, Theruvakkattil S. Sreeprasad, Akshaya K. Samal and Thalappil Pradeep*

DST Unit of Nanoscience (DST UNS), Department of Chemistry, Indian Institute of Technology Madras, Chennai, India

Abstract

Comprehensive knowledge over the shape of nanomaterials is a critical factor in designing devices with desired functions. Due to this reason, systematic efforts have been made to synthesize materials of diverse shape in the nanoscale regime. Anisotropic nanomaterials are a class of materials in which their properties are direction-dependent and more than one structural parameter is needed to describe them. Their unique and fine-tuned physical and chemical properties make them ideal candidates for devising new applications. In addition, the assembly of ordered one-dimensional (1D), two-dimensional (2D), and three-dimensional (3D) arrays of anisotropic nanoparticles brings novel properties into the resulting system, which would be entirely different from the properties of individual nanoparticles. This review presents an overview of current research in the area of anisotropic nanomaterials in general and noble metal nanoparticles in particular. We begin with an introduction to the advancements in this area followed by general aspects of the growth of anisotropic nanoparticles. Then we describe several important synthetic protocols for making anisotropic nanomaterials, followed by a summary of their assemblies, and conclude with major applications.

Contents

Panikkanvalappil R. Sajanlal received his M.Sc. degree in chemistry from the University of Calicut, India, in 2004. He is currently working toward his PhD in chemistry under the supervision of Prof. T. Pradeep at the Indian Institute of Technology Madras, India. His current research focuses on the shape-controlled synthesis, characterization, and applications of anisotropic meso/nanomaterials.

Theruvakkattil S. Sreeprasad received his M.Sc. degree in chemistry from the School of chemical sciences, M. G. University, India, in 2004. He is currently working toward his PhD in chemistry under the supervision of Prof. T. Pradeep at the Indian Institute of Technology Madras, India. His current research focuses on the post-synthetic tuning of size, shape, composition and properties of one and two dimensional nanosystems.

Dr. Akshaya K. Samal received his M.Sc. degree in chemistry from the Sambalpur University, India and Ph. D degree in chemistry under the supervision of Prof. T. Pradeep from the Indian Institute of Technology Madras, India. His current research focuses on synthesis, characterization and properties of one dimensional nanostructures.

Thalappil Pradeep is a Professor of Chemistry at the Indian Institute of Technology Madras, Chennai, India. He earned his PhD from the Indian Institute of Science in 1991 and had post doctoral training at the Lawrence Berkeley Laboratory, University of California, Berkeley and Purdue University, West Lafayette. He held

visiting positions at many leading universities and institutes in Asia and Europe. He is a recipient of several awards including the prestigious Shanti Swaroop Bhatnagar Prize and is a Fellow of the Indian Academy of Sciences. He has authored over 200 scientific papers in journals and is an inventor of more than 15 patents. Professor Pradeep's research interests are in nanomaterials, molecular surfaces, monolayers, ion-surface collisions, clusters, spectroscopy, electronic structure, and instrumentation. His other interests include education, popularization of science, and development of advanced teaching aids. He has authored a few popular science books as well.

ratio. When compared to macrostructures, larger proportions of constituent atoms or molecules lie at the surface of nanomaterials, leading to large surface to volume ratio, which can influence their reactivity, hardness, as well as magnetic, catalytic, and opto-electronic properties.

Restricted motion of electrons, holes, excitons, phonons, and plasmons with respect to the physical shape of an object is the reason for the change in properties of typical nanosystems. The most important change that is manifested is in color, due to the confinement of electrons and consequent changes in electronic energy levels. In the case of isotropic or 0D particles (e.g. sphere), because of the confinement of electrons to the same extent in all the three dimensions, properties will be more or less the same regardless of directions. In this case, all the three dimensions are the same for the object under study. Tuning the properties of these particles will be difficult compared to other materials that show direction and dimension dependent physical and chemical properties, generally named as anisotropic nanomaterials. They are coming under the category of 1, 2, and 3D nanostructures, wherein the electron motions are possible in these many dimensions. A pictorial representation of isotropic and anisotropic nanomaterials, categorized based on the dimensionality, is shown in Fig. 1. A diverse spectrum of anisotropic nanomaterials are reported in the literature such as nanorods (10–14), nanowires (15–21), nanotubes (22), and so on belonging to 1D; triangles (23–26), plates and sheets (27–33), ribbon (34), and so on belonging to 2D; and pyramids (35–38), stars (39–42), flowers (43–50), multi-pods (51–58), nanourchins (59), tadpole (60), nanocages (61), nanorice (62, 63), nanocorns (64), nanoboxes (65, 66), nanocubes (67), triangular nanoframes (68), nanodumbbells (69), and so on belonging at 3D nanostructures. Since there has been an explosion of research in the area of anisotropic nanomaterials, several reviews are available in the literature (70–78) and presenting a comprehensive review of research work is not an easy task. Here we plan to present only a glimpse into this fascinating area.
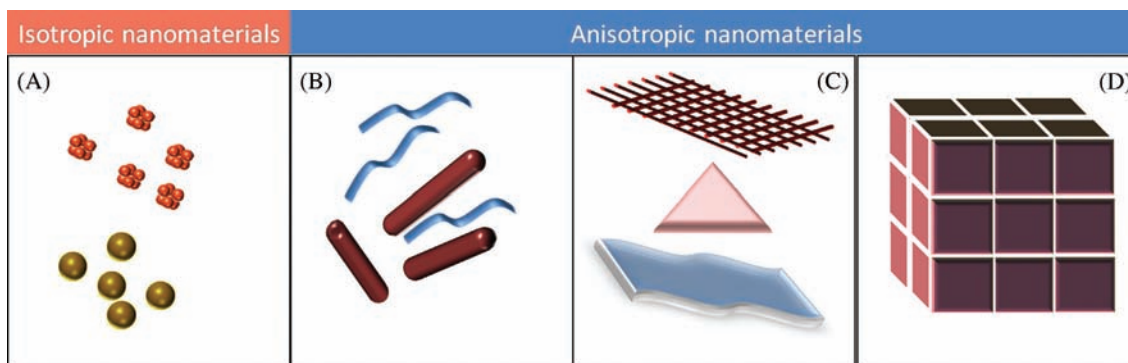
One of the fascinating aspects of science at the nanoscale is the size and shape-dependent variation in properties of matter. Due to this reason, systematic efforts have been made to find various parameters that directly affect the intrinsic properties of materials at this length scale (1–7). Among these, shape was found to play an important role in determining the properties of nanomaterials (8). After the discovery of carbon nanotubes (9), a 1D nanostructure, being considered as a standard example of nanomaterials exhibiting unique physiochemical properties, considerable attention has been paid on the shape-dependent synthesis of diverse nanomaterials. Many unusual properties of such materials arise due to spatial confinement of electrons, phonons, and electric fields around the particles as well as due to their large surface to volume

Fig. 1. Various kinds of nanomaterials. (A) 0D spheres and clusters. (B) 1D nanofibers, wires, and rods. (C) 2D films, plates, and networks. (D) 3D nanomaterials.

Particle anisotropy offers features and functions that are difficult to obtain simply by size-tuning of spherical nanoparticles. For example, a slight change in particle geometry can produce great changes in the surface plasmon peak position of a metallic nanoparticle, which can hardly be achieved in the spherical nanosystems through a similar change in diameter. In addition, the optical properties of anisotropic gold or silver nanorods (NRs) or prisms are tunable throughout the visible, near-infrared (NIR), and infrared regions of the spectrum, as a function of their aspect ratios. Even though isotropic gold nanoparticles show intense surface plasmon resonance (SPR) absorption with good absorption coefficient comparable to or larger than organic dye molecules, the strength of absorption is weakly dependent on its size, which limits its application in sensing. When anisotropy is added to the nanoparticles, such as NRs or prisms, the SPR is not only enhanced but also becomes strongly tunable as a function of aspect ratio. One reason for this is perhaps that these structures of well-controlled size and shape possess different surface areas and crystallographic facets. Introducing anisotropy into the nanoparticles can also make a substantial change in their magnetic properties. The coercive field of ferromagnetic particles can be increased considerably by introducing shape anisotropy (79). Bio-compatibility (80, 81), large extinction cross-sections (compared to spherical nanoparticles and organic dyes), optical absorption in the near-infrared region (the wavelength region where blood and tissues are relatively transparent to the radiation) (82, 83), and enhanced photothermal heating capacity (84–89) enables them to be good candidates for diagnosis and therapeutic medical applications (90–92). The utility of anisotropic nanomaterials in photothermal cancer diagnosis and treatment of tumor cells have been well-documented in the literature (82, 90–98). Localized electric fields generated near these nanoparticles have been exploited for the chemical and biological detection of molecules (99–103) and surface-enhanced Raman spectroscopy (SERS) (104–117). The strong electromagnetic fields at the surfaces of anisotropic metallic nanostructures make them useful for non-linear optical (NLO) applications in photonics as well as chemical and biological detection (118). This method has specific advantages over the other existing methods with a capability of detecting toxins in different environments. A considerable amount of effort has been devoted from 1998 onward for developing various nanomaterials with high second-order NLO properties (119–124).

Anisotropic nanomaterials are a good candidate for biomolecule detection. Though spherical noble metal nanoparticles-based label-free biochip shows good sensitivity for the detection of trace biomolecules, anisotropic nanoparticles with novel properties allow their detection with improved sensitivity (125–127). Surface plasmon resonance of colloidal nanocrystals has been used to study specific sequences, hybridization, and single-base mutations of DNA (128–130). Gold nanorod (GNRs) have been used to image *Bacillus subtilis spores* (a simulant of *Bacillus anthracis*) using two-photon luminescence (TPL) microscopy. An enhanced image contrast in photoacoustic imaging has been achieved due to their NIR absorption property (131–134). Even though plenty of such applications in diverse areas are possible with anisotropic nanomaterials, some of the important applications are only highlighted in this review.

The explosion of anisotropic nanomaterials research (135) is reflected in the graph shown in Fig. 2, which summarizes a literature search of papers having selected keywords (nanotubes, nanowires, nanorods, nanoplates, and nanoflowers) in their titles over the past 10 years.

The degree of anisotropy in a nanosystem can be enhanced by the incorporation of lower dimensional nanostructures into the same or higher dimensional nanosystems. These hybrid nanosystems show novel properties due to the effective coupling of different domains. Large numbers of hybrid- multi-dimensional systems are available in the literature and some such systems have been presented in Table 1 (136–149). Fabrication of nanoparticles into 1, 2, or 3D functional
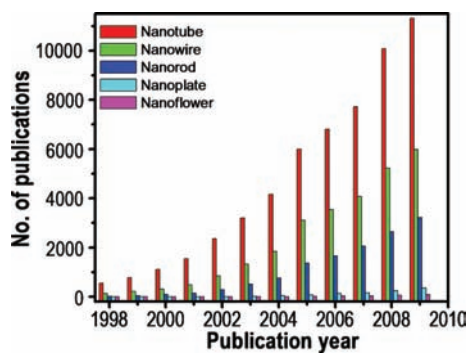
Fig. 2. Number of papers published during the last decade (1998–2009), including certain keywords (as indicated) in their title. Source: ISI Web of Science.

structures is necessary to utilize their collective properties (150). Assembling nanoparticles is another way to improve the properties and performance of anisotropic nanoparticles (151, 152). Controlled organization of such nanomaterials brings novel properties into the resulting system that would neither be the properties of individual nanoparticles nor those of its bulk entity (153, 154). Assembly of nanomaterials into 2 or 3D lattices largely depends on their shape, surface properties, charge, polarizability, magnetic dipole moment, mass, and so on. The added advantage of anisotropic nanoparticle assembly is that the same nanomaterial can interact and assemble in different ways due to its inherent anisotropy in the structure. So, from the same building blocks, we can create assemblies having different properties depending on the dimensionality as well as the nature of interaction between the building blocks. Such

Table 1. Hybrid heterostructures of multi-dimensional nanocomposite materials

System	Schematic	Example	Reference
0D in 1D		$SiND/SiO_2NW$	117
0D on 1D		AuND/SiNW	118
1D on 1D (radial heterostructure)		SiNW/CNT	119, 120
1D on 1D (axial heterostructure)		SiNW/CNT	121
1D on 1D (biaxial heterostructure)		$SiNW/SiO_2NW$	122
1D on 1D (branched)		CdS/ZnS	123
0D on 2D		AuND/Si	124
1D on 2D		SiNW/Si	125
2D on 2D (quantum well)		$Si/Si_{1-x}Ge_x$	126–129

systems can be tentatively called as 'anisotropic super-structures'.

In this review, we summarize various existing synthetic protocols for making anisotropic nanomaterials and highlight the importance of morphology on the dependence of their physical and chemical properties. As a wide range of synthetic protocols are available in the literature, we will be reviewing only selected common chemical routes for their synthesis. Discussion will highlight some important aspects of shape evolution of these materials. Due to the magnitude of the literature, we restrict our discussion mainly to noble metals. At the same time, we have touched upon certain aspects of other nanosystems as well to make this review all-round. Because of the importance of assembled nanostructures in tuning the collective properties of nanomaterials, assemblies of various anisotropic nanoparticles have been included. By taking NRs as an example, we present an overview of the various assemblies made. This review ends with the various applications of anisotropic nanomaterials and their assembled structures, followed by a summary and future outlook.

2. General aspects of anisotropic nanoparticle growth

Since sphere is the lowest-energy shape, simple reduction of metal salts generally results in the formation of spherical nanoparticles (155). By suitably controlling the experimental parameters such as concentration of the metal precursor, reducing agents, and stabilizers and reaction conditions such as temperature, time, and so on, it is possible to tune the shape of the nanoparticles. The exact role of these parameters in determining the morphology of the crystals is not yet fully understood. At the same time, it has been proposed that synergistic effect of each one of these parameters has substantial influence on the final shape of the nanocrystal. Many techniques, including both top-down and bottom-up approaches, have been developed and applied for the synthesis of anisotropic nanoparticles. As nanoparticles produced by top-down approaches have a relatively broad size distribution, varied particle shape or geometry, and use expensive synthetic pathways that are industrially non-scalable, bottom-up approaches are far more popular in the synthesis of nanoparticles. Wet chemical synthesis is a potential bottom-up method to produce anisotropic nanoparticles in high yield and structural purity with varying size, shape, structure, composition, and surface chemistry.

Generally, nanoparticle growth can happen either in a thermodynamically controlled or kinetically controlled manner (156). Thermodynamic growth often results in uniform growth of all crystal facets and subsequent formation of spherical or near-spherical structures. In the case of kinetically controlled growth, preferential and

directional growth happens that in turn results in the anisotropic growth. The synergistic effects of both thermodynamic and the kinetic aspects play a critical role in determining nanoparticle shape. However, a general mechanism for the formation of these morphologies has not been fully understood yet. Preferential adsorption of capping molecules to specific facets can hinder or enhance the crystal growth in some directions. In certain cases, formation of surfactant micelles or structural defects would physically direct the anisotropic growth (157). Under specific conditions, capping agents also play an important role to increase the yield of a particular structure with high monodispersity. Aforementioned reasons are unable to address experimental observations since formation of similar shapes was observed even in the absence of capping agents (vapor phase synthesis) (158). The anisotropic interactions of different facets with surfactant and solvents will result in the formation of twinned morphology with lower energy. These aspects make solution-based synthesis more powerful and versatile than vapor-phase methods for the synthesis of anisotropic noble metal nanoparticles. Other aspects such as oxidative etching and control of the nucleation can also induce the anisotropic growth of the nanoparticles. According to Lofton and Sigmund, formation of twin planes in the seed particles promotes the creation of favorable sites for the anisotropic growth of nanoparticles (159). The strategies to control the kinetics and formation of desired nuclei with twin planes during the nucleation provide better ways to produce anisotropic noble metal nanoparticles. The energetic aspects can also play an important role in determining the anisotropic growth of nanoparticles. The formation of anisotropic structures is a direct consequence of the energetics being dominated by surface energy in nanometer regime. Anisotropic nanoparticles have higher surface to volume ratios than spheres and, consequently, higher energy per atom, even though they can expose facets with lower surface energies ((111) in face-centered cubic, fcc, metals, for example).

3. Synthesis of anisotropic nanomaterials

3.1 Seed-mediated synthesis

Even though a large number of methods have been used for making anisotropic nanostructures, the seed-mediated growth process is a widely used method that can yield various nanostructures such as rods, wires, triangles, stars, flowers, and so on. This method is a modified form of Zsigmondy's 'nuclear' method, which involved a two-step process for making nanoparticles (160). In 2001, Jana et al. produced NRs in good yield by the seed-mediated method (161). This method involves two steps. The first step is the synthesis of 'seed nanoparticles' by simple reduction process in which the metal salt is

reduced by reducing agents in the presence of stabilizing agents. Sodium borohydride is the commonly used reducing agent. The seed need not always be a metal nanoparticle. Growth of seed nanoparticles into the desired shape is the second step of this process. The growth solution contains surfactant or shaping agent and a mild reducing agent. In this process, metal salts will get reduced on the surface of the seed nanoparticles. The surfactant molecules will form suitable templates that facilitates the growth process to yield nanoparticles of desired morphology. The size of the nanoparticles can be tuned by changing the amount of seed nanoparticles added. In the case of GNRs, the size can be reduced by increasing the amount of seed particles. External agents such as various molecules or ions can alter the growth direction of the nanoparticles and can result in the formation of variously shaped nanoparticles. With the addition of a small amount of iodide ion in a growth solution used in the GNR synthesis, the shape of the resultant nanoparticles can be changed into triangular nanoprisms (162). Here, the iodide ion adsorption appears to suppress the crystal growth along the Au(111) direction, resulting in Au(111)-faced triangular nanoprisms. When the counter anions of the surfactant cetyltrimethylammonium bromide (CTAB) were replaced with chloride ions, a drastic change in the morphology from rod to rice-shape was observed, which demonstrates the effectiveness of the adsorption of halide ions.

There are other factors that influence the size and shape of the nanostructures. The concentration of surfactant molecules is one parameter that plays an important role in the shape determination, since the shape of the micelles formed by the surfactant during the growth varies with the concentration. The synthetic method of gold nanoprism developed by Millstone et al. (23) is an example for the dependence of surfactant concentration on the morphology determination. In this approach, small gold seed nanoparticles of ~5 nm are subjected to a three-step growth process in an aqueous solution containing the capping agent CTAB, gold ions, reducing agent (ascorbic acid), and NaOH, resulting in the formation of gold nanoprisms in very good yield. Nanoprisms were formed only when saturated CTAB solution was used, which is a clear indication of the concentration dependence on the morphology of the nanoparticles. Transmission electron microscopy (TEM) image corresponding selected area electron diffraction (SAED) patterns of the nanoprisms synthesized by this method is shown in Fig. 3A. The UV-vis absorption spectrum of nanoprisms (Fig. 3B) shows three different absorptions. The peak in the NIR region is attributed to in-plane SPR of nanoprisms and that at 540 nm is due to their out of plane SPR. Broad band in the UV-vis-NIR spectrum at 800 nm is assigned to the in-plane quadrupole mode of the nanoprisms (Fig. 3B). This assignment is based upon the characterization of these prisms by electron microscopy and discrete dipole approximation (DDA) calculations, which predict plasmon bands that match the experiment. The observed absorption spectrum of the nanoprisms was in good agreement with the theoretical spectrum. The edge length of these Au nanoprisms can be controlled while preserving their original shape, crystal properties, and thickness. Importantly, edge length control is a way of tailoring the optical properties of these structures. For that, the prisms have been used as seeds, and reinitiated the particle growth by exposing them to Au ions in the presence of a reducing agent in a step-by-step manner (163). By this method, the edge length of the nanoprism has been varied from 100 to 300 nm without changing their crystallinity and thickness.

An aligned array of the nanotriangles on the indium tin oxide (ITO) surface (164) has been made using the seed-mediated approach at low temperature. Here, 4 nm gold seed nanoparticles attached to the conducting glass
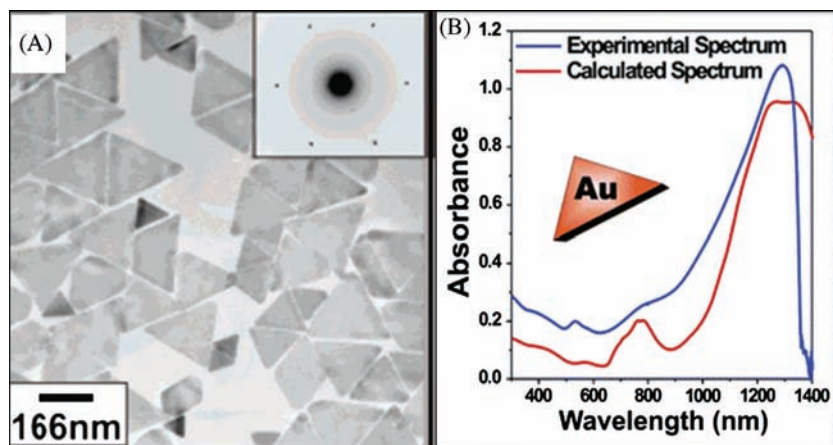

Fig. 3. (A) TEM image of Au triangular nanoparticles. The inset is the SAED pattern taken from individual nanoprism. (B) UV-vis-NIR spectra of purified Au nanoprisms (blue trace) and DDA calculation (red trace). Reproduced with permission from Reference (23). American Chemical Society, Copyright (2005).

surface were grown into gold nanotriangles by applying an electric potential. In this case, low temperature and electric field were found to be the critical factors that favor the nanotriangle growth. Silver nanoplates with sizes of 40–300 nm have been synthesized via a simple room-temperature solution-phase chemical reduction method in the presence of dilute CTAB and ~15 nm Ag@citrate seed particles (165). The interesting finding in this case is that the size of nanoplates can be easily controlled by using a CTAB solution of 10 to 15 times dilution of that normally used in the seed-mediated synthesis (100 mM). Structure and surface analysis data revealed that the selective adsorption of CTAB on the (111) plane of silver seeds and the formation of silver bromide in contact with the seeds play critical roles in the nanoplate formation.

Another variety of nanomaterial, core-shell nanocube, made of Au and Pd (Au@Pd nanocubes) has been synthesized using a modified two-step seed-mediated growth method (166). Au nanoparticles of about 3 nm in diameter were first synthesized as the seeds for growing about 30 nm Au nano-octahedra that acts as the core. Then the uniform Au@Pd nanocubes were overgrown on the octahedral Au cores in high yield by reducing H_2PdCl_4 with ascorbic acid under the assistance of a surfactant CTAB (Fig. 4A–C). Another two kinds of binary metal core-shell nanoparticles, Au@Ag nanocubes and Au@Pt nanospheres, were also synthesized in the similar reaction conditions as shown in Fig. 4. It was found that Au@Ag nanoparticles exhibit uniform cubic shape and are well monodispersed. In the case of Au@Pt, uniform nanospheres with a rough surface were observed. This dramatically different morphology suggests a 3D heterogeneous nucleation and growth, rather than the layer-by-layer epitaxial growth for Pt shells on Au seeds. The growth of heterogeneous metal shells on the gold core presents two different forms, the conformal epitaxial growth for Au@Pd and Au@Ag nanocubes (Fig. 4D) and the heterogeneous nucleation and island growth for Au@Pt nanospheres (Fig. 4E). In order to achieve epitaxial layered growth of heterogeneous core-shell nanocrystals, the following rules have to be taken care of: (1) the lattice constants of two metals should be comparable with the lattice mismatch, smaller than about 5%. The shell metal with smaller atom radius is easier to grow epitaxially on the core as it could uniformly release the lattice strain resulting from the lattice mismatch. (2) The electronegativity of the shell metal is to be lower than the core metal in order to avoid the displacement reaction and to easily wet the surface of the core. Otherwise, the shell metal intensively tends toward galvanic displacement of the core metal instead of epitaxial growth. Recently, Cho et al. have demonstrated a simple and versatile method for generating core-shell, bimetallic nanocrystals with GNRs as the seeds for epitaxial growth. The resultant Au@Ag nanocrystals were mostly octahedral in shape, while their sizes could be controlled by using GNRs with different aspect ratios (167). Apart from this, a fine control of the nanoparticle shape can be
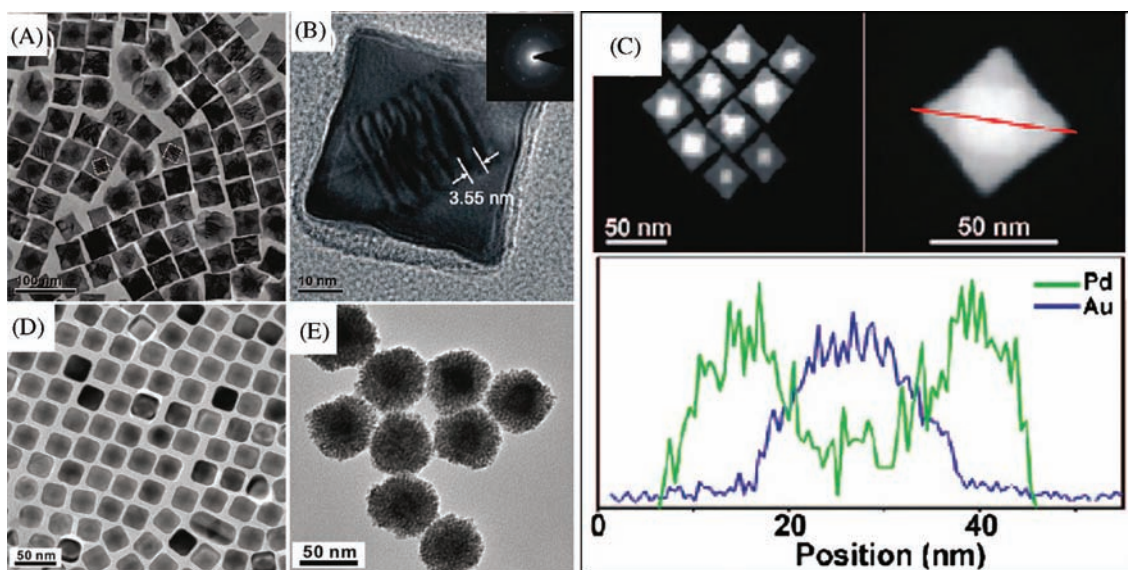
Fig. 4. (A) TEM image of Au@Pd nanocubes. (B) TEM image of a single Au@Pd nanocube at high magnification. The inset is the SAED pattern taken from individual nanocube. (C) STEM images of the octahedral Au seed within a cubic Pd shell and cross-sectional compositional line profiles of a Au@Pd nanocube along the diagonal (indicated by a red line). D and E are TEM images of Au@Ag nanocubes and Au@Pt nanoparticles, respectively. Reproduced with permission from Reference (166). American Chemical Society, Copyright (2008).

achieved by the systematic variation of the experimental parameters (168).

In Fig. 5, the table shows the various experimental conditions at which gold particles of different shapes can be formed. Corresponding TEM images of these structures are presented in Fig. 5A–D. This solution-based chemical route produces a number of structural architectures from rod-, rectangle-, hexagon-, cube-, triangle-, and star-like Au particles in high yield at room temperature in the presence of a single surfactant in aqueous solution. With an altered order of reactant mixing and by the addition of NaOH, seed nanoparticles can grow into gold nanostars of size less than 100 nm (Fig. 6A and B) (39). Even though the exact mechanism of formation of gold nanostars is unclear it is believed that the addition of NaOH may lead to more rapid growth due to forced reduction of gold ions. Single particle spectroscopy revealed that these nanoparticles have multiple plasmon resonances resulting in polarization-dependent scattering with multiple spectral peaks, which correspond to the different tips on the nanostar (Fig. 6C). The gold nanostars described here provide a multi-spectral signal

| [CTAB]/M	[Au]$_{seed}$/M	[Au^{3+}]/M	[AA]/M	Shape/Profile	Dimension§	% Yield
1.6×10^{-2}	1.25×10^{-8}	2.0×10^{-4}	6.0×10^{-3}	Cube	66 nm	~ 85
1.6×10^{-2}	1.25×10^{-8}	2.0×10^{-4}	3.0×10^{-3}	Hexagon	70 nm	~ 80
1.6×10^{-2}	1.25×10^{-7}	2.0×10^{-4}	6.0×10^{-3}	Triangle	35 nm	~ 80
1.6×10^{-2}	1.25×10^{-8}	4.0×10^{-4}	6.4×10^{-4}	Cube^{a}	90 nm	~ 70
9.5×10^{-2}	1.25×10^{-7}	4.0×10^{-4}	6.0×10^{-3}	Tetrapod^{a}	30 nm	~ 70
1.6×10^{-2}	1.25×10^{-8}	4.0×10^{-4}	1.2×10^{-2}	Star	66 nm	~ 50
5.0×10^{-2}	$6.25 \times 10^{-7 \, b}$	5.0×10^{-4}	3.0×10^{-3}	Tetrapod	293 nm	~ 75
9.5×10^{-2}	2.5×10^{-7}	4.0×10^{-4}	6.4×10^{-4}	Branched^{a}	174 nm	~ 95
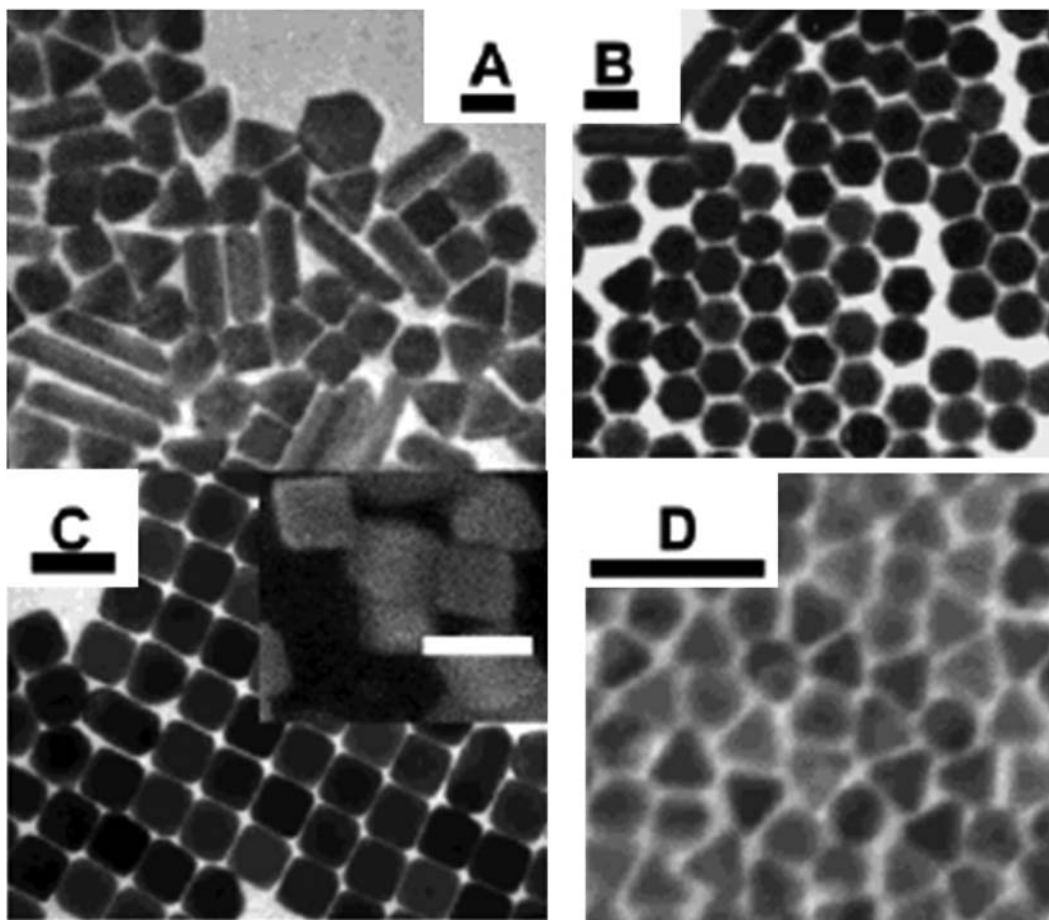
Fig. 5. Table shows the shapes of gold particles and corresponding reaction conditions. A–D are the TEM images of various anisotropic Au nanoparticles synthesized under different conditions. Inset of C shows the corresponding SEM image. Scale bars are (100 nm). Reproduced with permission from Reference (168). American Chemical Society, Copyright (2004).
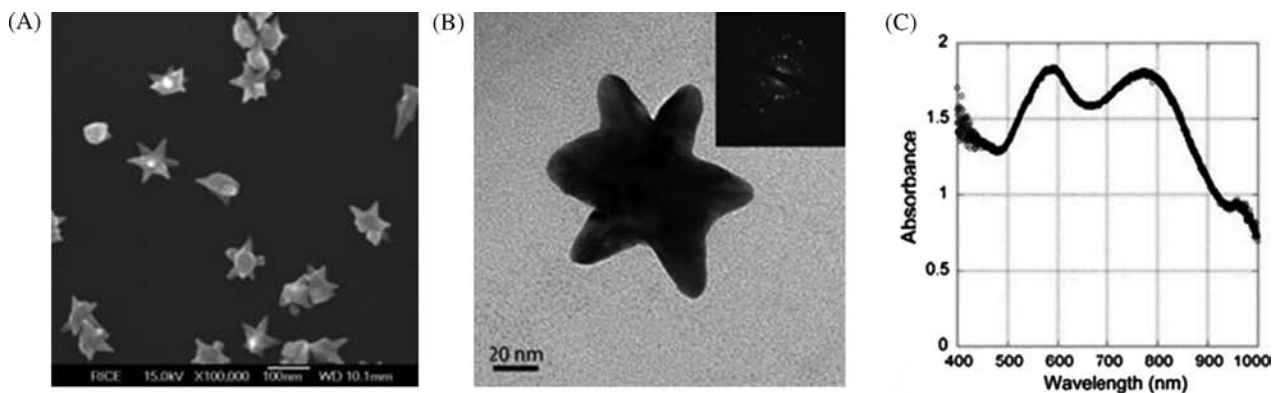
Fig. 6. A and B are SEM and TEM images of star-shaped gold nanocrystals, respectively. Inset of B shows the SAED pattern taken from a single nanostar. An extinction spectrum of the nanostar solution exhibits broad visible and NIR peaks (C). Reproduced with permission from Reference (39). American Chemical Society, Copyright (2006).

from a single nanoparticle that could be used to detect 3D orientations of molecules by exploiting their multi-directional polarized scattering. Gold nanostars (Fig. 7) with single crystalline tips can be synthesized in extremely high yield through the reduction of $HAuCl_4$ in a concentrated solution of poly(vinylpyrrolidone) (PVP) in N,N-dimethylformamide (DMF), in the presence of preformed Au nanoparticle seeds (42).

The morphology of the seed particle is one important parameter that decides the anisotropic growth. Beautiful gold mesoflowers (MFs) (Fig. 8A and B) can be synthesized in large quantity by the seed-mediated method from an oligoaniline capped Au nanoparticle seeds at 80°C (169). These MFs are made up of a large number of spiky stems projecting outward from a core in all directions (Fig. 8B). The stems are bearing high
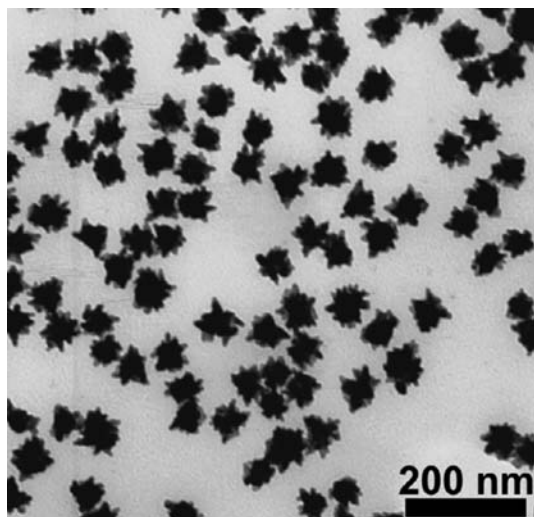

Fig. 7. TEM image of Au nanostars synthesized through reduction of $HAuCl_4$ in a PVP/DMF mixture, in the presence of preformed Au seeds, using 10 mM PVP. Reproduced with permission from Reference (42). Institute of Physics, Copyright (2006).

resemblance to a hierarchical array of scales or plate-like subunits, which themselves have the shape of stars forming a pyramid of stars (Fig. 8C). Each stem has ridges along its corners that give a unique morphology. The presence of five edges is giving a star-shaped appearance to the stem as it is viewed from the top and ridges along the corners of the stems give a stacked appearance (Fig. 8D). In this case, presence of multiple twinning in the seed particle leads to anisotropic growth at high temperature. By stopping the reaction at a predetermined time or by controlling the amount of seed nanoparticle, it is possible to tune the size of the MFs from 100 to 4000 nm. One of the important aspects of this synthesis is the high degree of shape purity in the synthesis. It is possible to create these materials in gram scale without any other shapes.

In certain cases, it is possible to synthesize 3D nanoparticles even in the absence of surfactant using this approach. Here, Au^{3+} and NH_2OH were added to a chosen amount of $AgNO_3$ solution. Under vigorous stirring, colloidal gold seeds were added rapidly resulting in the formation of 3D nanothorns. The formation and structural changes of these 3D thorny gold nanoparticles can be explained by the site specific deposition of AgCl on the surface of gold nanoparticle seeds (51).

Knowledge of the crystal structure of the resultant nanoparticles is crucial for understanding its growth mechanism. Murphy et al. (170) and Johnson et al. (171) suggested a mechanism for the growth of NRs based on preferential surfactant binding to certain facets of the seed particle. The preferential binding of CTA^+ head group to certain crystal faces of the face-centered cubic (*fcc*) seed causes symmetry breaking and this leads to the formation of NRs. Crystal structure of gold contains 5 side-faces containing (100) surfaces and 10 end-faces containing (111) surfaces as shown in Fig. 9A. The surface energy of (100) plane is higher than that of (111) plane. The preferential binding of side-faces, which
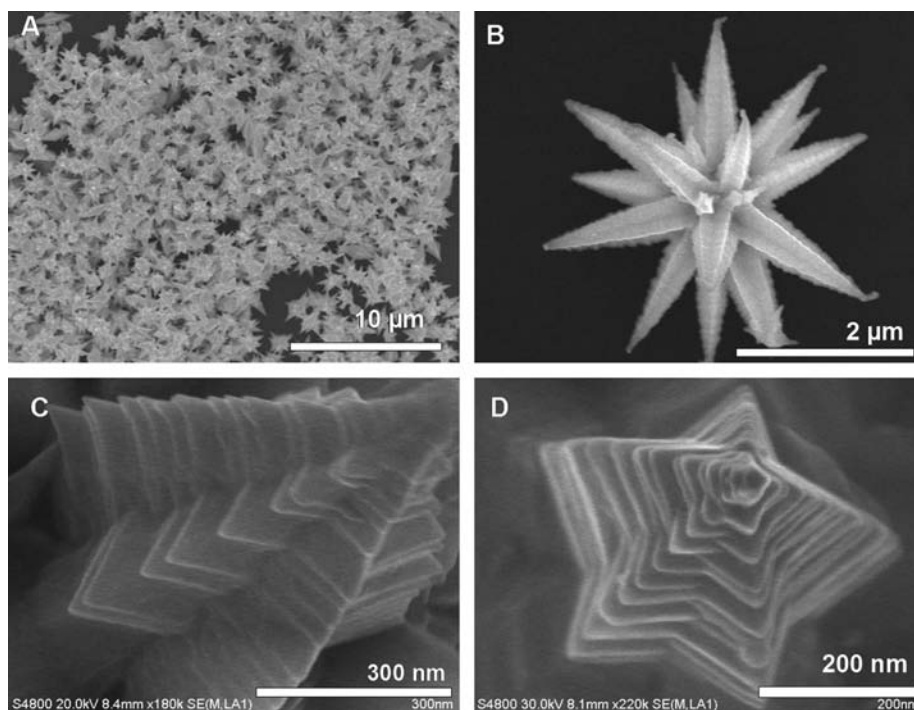
Fig. 8. Large area (A) and corresponding single particle. (B) Field-emission scanning electron microscopy (FESEM) images of gold MFs. (C) An enlarged FESEM image of a single stem of the MF showing ridges along the edges. (D) Top view of a single stem of the MF showing the pentagonal structure. Reproduced with permission from Reference (169). Springer, Copyright (2009).

is more comparable in size with CTA^+ head group than end-faces, stabilizes the high energy side-faces. Due to the preferential binding of CTA^+ head group on side-faces, the nucleation of gold is inhibited there. Therefore, the growth of NRs happens along the (110) common axis on (111) faces, which do not contain the CTA^+ head groups. The surfactant CTAB has a hydrophobic as well as a hydrophilic group. The quaternary ammonium ion present on the hydrophilic surface forms a covalent bond with the gold surface thereby opening the hydrophobic group outward. The hydrophobic group of another CTAB molecule forms a bilayer with the outward projecting hydrophobic group of the attached CTAB molecule; the hydrophilic group of the second CTAB molecule interacts with water leading to stabilization of GNR in an aqueous medium. The free energy of bilayer stabilization between CTAB molecules is found to be approximately 6 kJ/mol per two methylene groups; this energy is higher than the energy available at the room temperature ($\sim$2.5 kJ/mol). The bilayer formation on gold surface through alkyl groups can be visualized in a zipper fashion (Fig. 9B). Due to inhibited growth on the side-faces, the reduction of Au^{+1} followed by nucleation happens on the end-faces. Therefore, by controlling the ratio of seed to growth solution, the elongation of GNR can be controlled.
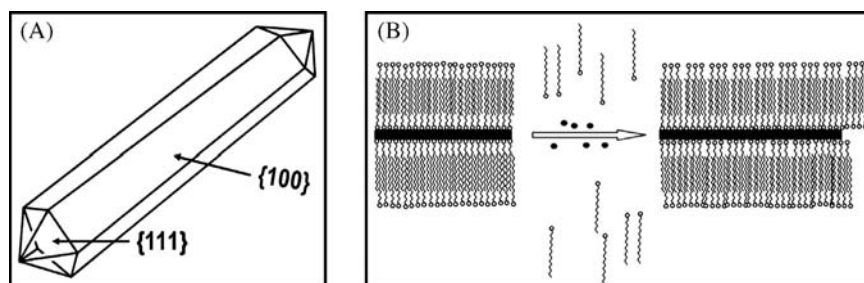
Fig. 9. Cartoon representation of (A) 3-D morphology showing (111) end-faces and (100) side-faces. (B) Illustration of 'zipping' mechanism for the formation of the bilayer of CTAB (squiggles) on the NR (black rectangle) surface may assist NR formation as more gold ion (black dots) is introduced. Reproduced with permission from Reference (170). American Chemical Society, Copyright (2005 and 2003).

In a separate study, Perez-Juste et al. proposed the electric-field-directed growth mechanism of GNRs (172). In this mechanism, it is suggested that ascorbic acid reduces $AuCl_4^-$-CTAB complex to $AuCl_2^-$-CTAB through the following reaction (I).

$$AuCl_4^- + 2e^- \rightleftarrows AuCl_2^- + 2Cl^- \qquad (I)$$

$$AuCl_2^- + e^- \rightleftarrows 2Au^0 + 2Cl^- \qquad (II)$$

The reduction of Au^{+1} occurs through electron transfer at the surface of the electron-rich CTAB capped seed particles via reaction II. The rate of nanorod formation depends on the collision of $AuCl_2^-$-CTAB complex and CTAB capped seed particles, which is controlled by the electrical double layer interaction between the CTAB and gold rods.

Though the growth mechanism of GNRs has been investigated extensively by different groups, the exact mechanism is still uncertain. Recent studies suggest that even in the absence of external addition of seed, GNRs can be made by following the same procedure. In 2010, Samal et al. synthesized GNRs through one-step process, whereby the use of seed particles was eliminated (173). The study suggests that the nature of metal seed (seeds made by various metals having different crystal struc-tures) doesn't affect the formation and monodispersity of GNRs. Further investigations revealed that sodium bor-ohydride present in the seed solution played a critical role in the formation of GNRs; that is, GNRs can be synthesized by direct addition of sodium borohydride to the growth solution. In this method, various metal seed particles with a size 3–5 nm of different crystal structures such as Fe (body centered cubic, *bcc*), Ru, and Cd (hexagonal close packing, *hcp*), Cu, Pb, Ag, and Au (cubic close packing, *ccp*), Hg (rhombohedral), In (tetra-gonal), and Sb (trigonal) were prepared from their salts by reduction with $NaBH_4$ and added to the growth solution. All the seed particles produced the NRs of the same structures. High-resolution transmission electron micro-scopy (HRTEM) image of the GNRs synthesized by various metal seeds of different crystal structures showed only *fcc* gold (Fig. 10). This suggests that the seed particles may not be directly affecting the growth of GNR.

The GNRs exhibit two surface plasmons in the absorption spectrum when electromagnetic radiation interacts with the length and width of the NRs. Interac-tion of electromagnetic radiation leads to the excitation surface plasmons along the long axis of the NRs (long-itudinal surface plasmon, LSP) or along the short axis of
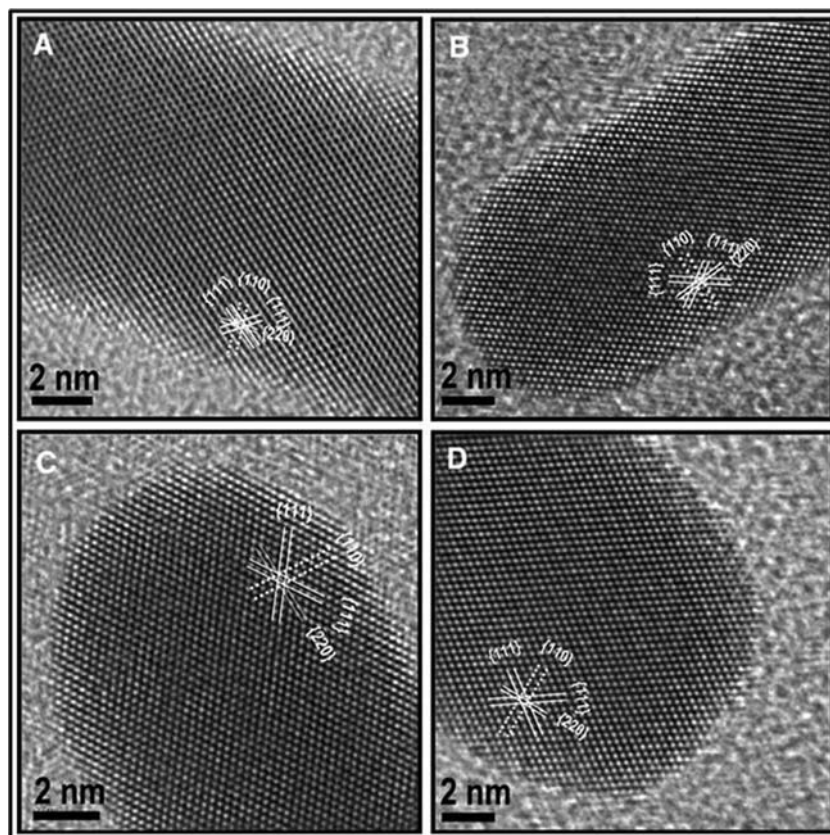
Fig. 10. HRTEM images of NRs formed using different seed particles: (A) Fe (*bcc*), (B) Cd (*hcp*), (C) Sb (trigonal), and (D) In (tetragonal). Although the metals are of different crystal structures, the GNRs formed are *fcc*. Reproduced with permission from Reference (173). Springer-Netherlands, Copyright (2010).
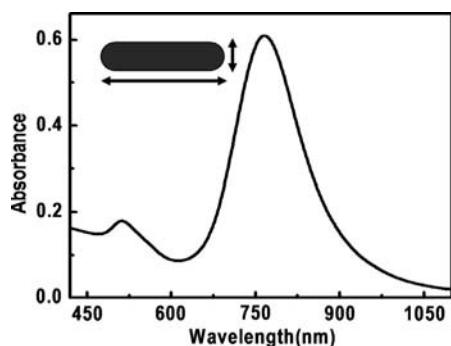
Fig. 11. Absorption spectrum of GNRs. The arrows correspond to the electron motions.

the NRs (TSP). Transverse surface plasmon (TSP) and LSP of the NRs appear in the visible and near NIR region in the absorption spectrum, respectively (Fig. 11).

As the length of the NRs increase, the LSP of the NRs red shifts to the NIR region. Typical synthesis does not produce much change in the width of the NRs and TSP stays close to 520 nm. But systematic change in LSP is easily achievable.

3.2 Polyol synthesis

Polyol synthesis is a simple and versatile route, developed in 1989 by Fievet et al. (174) and Viau et al. (175), to make colloidal particles of various shapes and sizes made of metals and their alloys. The present form of the polyol synthesis was developed by Sun et al. (176) and Wiley et al. (177). They have made a number of modifications to the conventional protocol. The polyol synthesis involves the reduction of an inorganic salt precursor by polyol at an elevated temperature. Polyol refers to alcohols containing multiple hydroxyl groups. Ethylene glycol, propylene glycol, pentane diols, glycerols, and so on are commonly used polyols. Many precursor salts can easily dissolve in polyol. Apart from this, temperature-dependent reducing power and relatively high boiling points make polyols suitable solvents for making anisotropic nanoparticles. Upon heating in the presence of air, ethylene glycol will get converted into glycolaldehyde, which acts as a dominant reductant for polyol syntheses of Ag nanostructures. Poly(vinylpyrrolidone) is commonly used as stabilizer to prevent agglomeration of the colloidal particles in polyol synthesis. It has been demonstrated that this method is good for making nanostructures of Ag, Pd, and Pt, as polyols have relatively high dielectric constant and can serve as a good solvent for both metal precursors and PVP. At elevated temperatures, ethylene glycol can reduce Ag^+ ions into Ag atoms, and thereby induce the nucleation and growth of silver nanostructures in the solution phase. Due to the presence of oxygen and nitrogen atoms in the pyrrolidone unit, PVP can adsorb onto the surface of silver and can stabilize the resulting structure. Moreover,

the extents of interaction strengths of PVP with different crystallographic facets of a silver lattice are different and could, therefore, induce anisotropic growth of silver.

It has been established that the morphology of final nanoparticles is mainly determined by the number of twin defects present in the initial seed that is shown in the schematic illustration in Fig. 12 (178). For making silver nanostructures by using polyol synthesis, first anhydrous ethylene glycol was heated at 160°C for 1 h. Then, separate solutions of $AgNO_3$ and PVP in ethylene glycol were simultaneously injected into the reaction flask by using a two-channel syringe pump. The first step of the growth is the reduction of $AgNO_3$ by ethylene glycol at an elevated temperature and the formation of elemental silver. In the subsequent steps, these silver atoms nucleate and form clusters (fluctuating structures) and nearly spherical particles. Once the nuclei attain a certain size, they become seeds: either a single-crystal, singly twinned, or multiply twinned particle. In the next step, silver atoms generated from the reduction of $AgNO_3$ get diffused to the surface of the nuclei and will deposit at active surface sites, forming metallic bonds with their neighbors. By adjusting the molar ratio between PVP and $AgNO_3$, the thickness of PVP coating and the location of PVP chains on suitable crystal planes can be modified. This modification alters the resistance of each facet to growth (addition of silver atoms), and lead to the formation of silver nanostructures with distinct shapes.

Most silver nuclei incorporate twin boundary defects as such defects enable a lower surface energy. As the growth proceeds, changes in the defect structure of the nuclei become too costly relative to the available thermal energy and they become trapped in a given morphology. As illustrated by Fig. 12, this process results in various kinds of seeds such as multiply twinned, singly twinned, and single-crystal seeds, with the fivefold symmetry. Multiply twinned decahedra are the naturally abundant seed morphology and are also the most reactive. Silver atoms preferentially add to the twin defects of decahedra, leading to the formation of nanowires (NWs) (Fig. 13A). Nanowire formation also requires the presence of NaCl and iron salt. In the absence of chloride ions, the seeds rapidly aggregated to form irregular particles. The Cl^- ions absorbs on seeds and electrostatically stabilize them against aggregation (179).

In order to retard the growth of NWs, one must prevent the formation of decahedral seeds. Monodispersed nanocubes (180) of silver have been synthesized in large quantities by introducing a small amount of hydrochloric acid to the conventional polyol synthesis (Fig. 13B) (181). Hydrochloric acid plays an important role in selectively etching and dissolving twinned decahedral seeds. The presence of protons slows down the reduction reaction and thereby facilitates the formation of single-crystal seeds and nanocube formation.
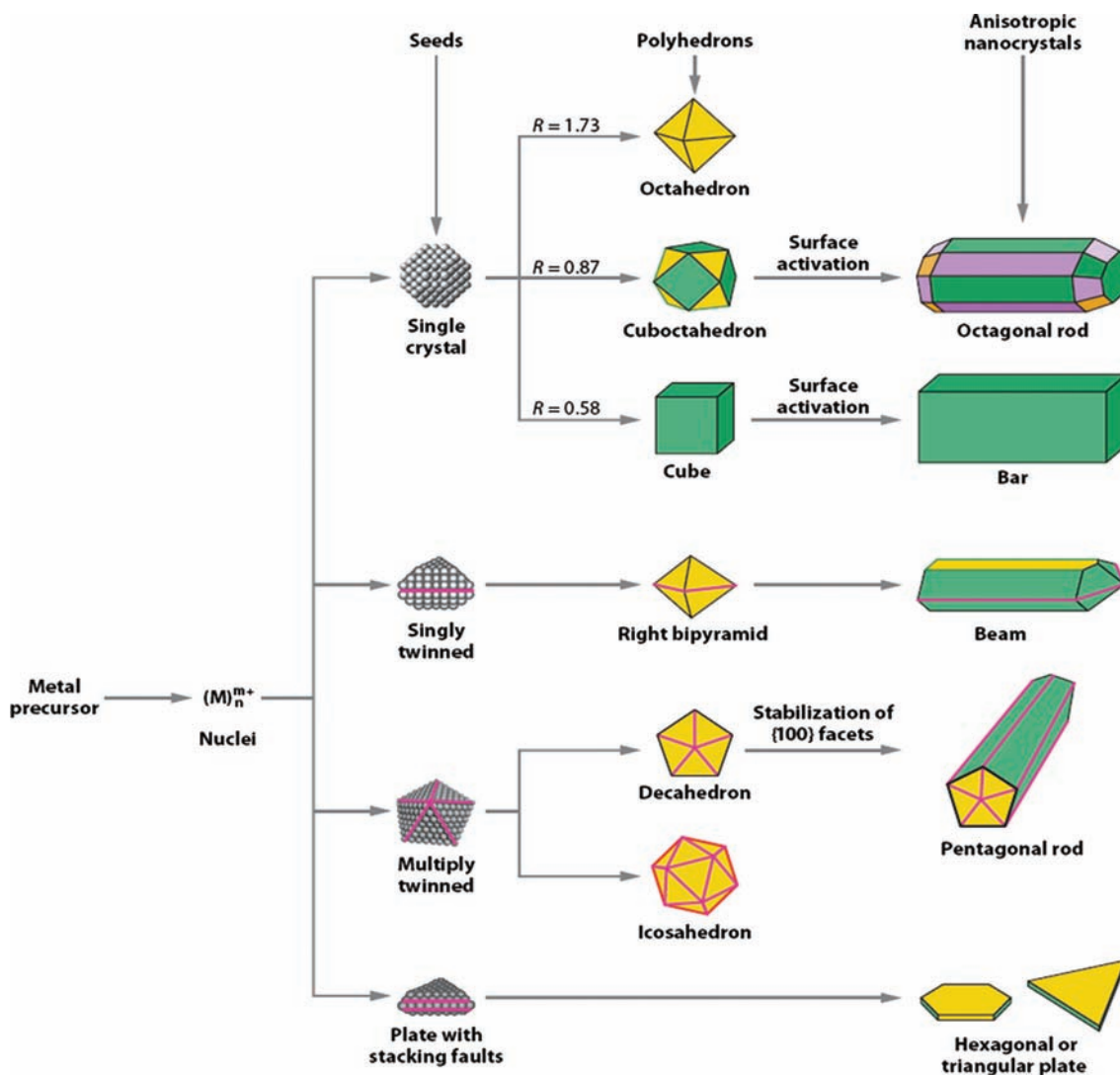
Fig. 12. A schematic illustrating various stages of the reaction that leads to the formation of noble-metal nanoparticles with different shapes. After the formation of nuclei (small clusters), they become seeds with a single-crystal, singly twinned, or multiply twinned structure. Stacking faults in the seeds results in plate-like structures. Green, orange, and purple represent the (100), (111), and (110) facets, respectively. The parameter R is defined as the ratio between the growth rates along the (100) and (111) directions. Twin planes are delineated in the drawing with magenta lines. Reproduced with permission from Reference (178). Wiley-VCH, Copyright (2004).

Even though the role of chloride ion is not completely understood, it is likely that the corrosive effect of Cl^- can etch twinned seeds as in the case of corrosion of steel.

If NaCl was substituted with 60 μM NaBr and the temperature was lowered to 155°C, the reaction produced silver nanobars in 1 h (Fig. 13C). Storage of nanobars in a 5 wt% aqueous solution of PVP for 1 week resulted in their transformation into single-crystal nanorice with rounded corners and edges (Fig. 13D). Seeds with single twin planes are necessary to produce Ag bipyramids (Fig. 13E). To produce such seeds, the extent of etching must be moderated so that the most reactive multiply twinned seeds can be etched away. This is achieved by reducing the amount of bromide by half relative to the nanobar reaction. Bromides enable sufficient etching to remove the multiple twined seeds but not so much as to eliminate singly twinned seeds.

Singly twinned seeds could also be grown slowly over 24 h to form silver nanobeams. Silver nanobeams are so named because they have a cross-sectional aspect ratio similar to that of a beam of wood. In comparison to the synthesis of right bipyramids, here, the concentrations of $AgNO_3$ and PVP were doubled and the temperature was lowered by 12°C, while the concentration of NaBr was kept the same. Although the concentration of the silver precursor was doubled, the lower reaction temperature resulted in a slower reduction rate.
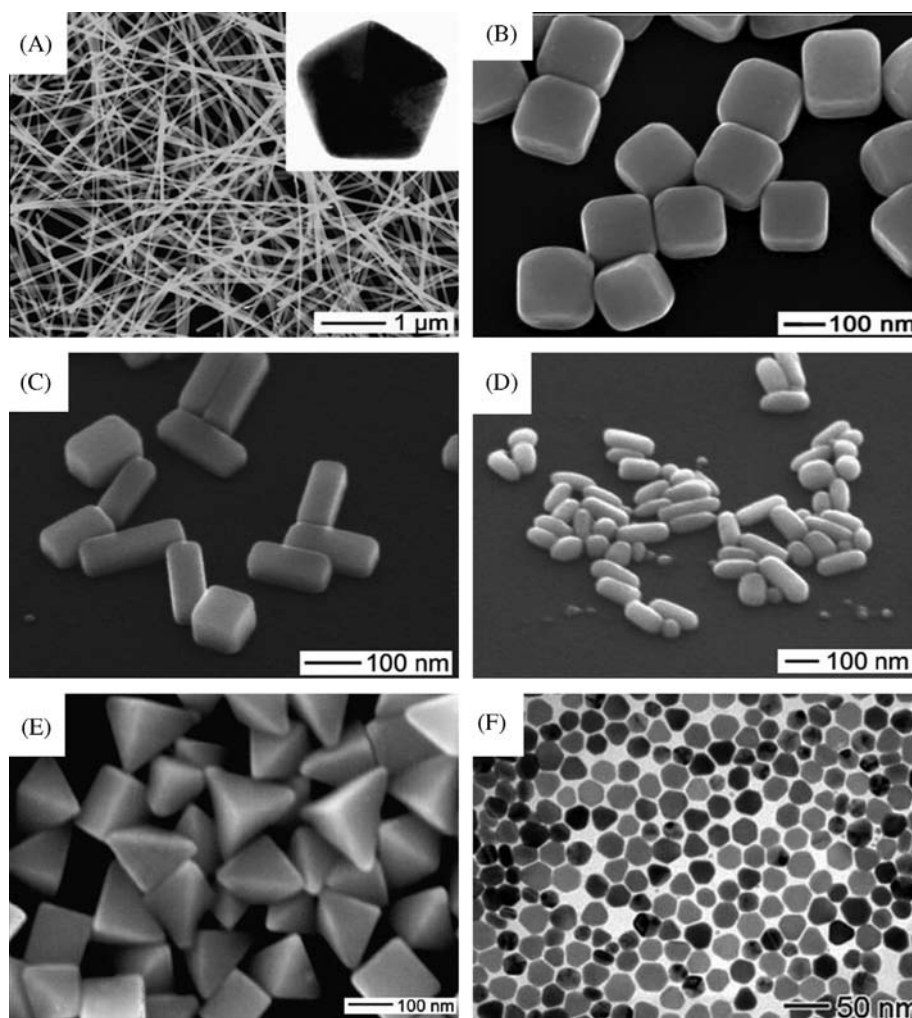
Fig. 13. (A) Large area SEM image of Ag NWs. Inset shows a cross-sectional TEM image of a microtomed NW, revealing its fivefold twinned crystal structure and pentagonal profile Reproduced with permission from Reference (179). American Chemical Society, Copyright (2008). (B) SEM image of Ag nanocubes. Reproduced with permission from Reference (180). American Association for the Advancement of Science (AAAS), Copyright (2002). (C) SEM image of the Ag nanobars produced when NaCl was substituted with NaBr (181). (D) SEM of nanorice at a 45° tilt. (E) SEM images of bipyramids approximately 75 and 150 nm in edge length (159). (F) SEM images of silver nanoplates prepared in the presence of PAM at 135°C for 3 h. Reproduced with permission from Reference (182). Royal Society of Chemistry, Copyright (2007).

In certain cases, polymers can alter the growth rate of the nanoparticles during polyol synthesis. Ag nanoplates (Fig. 13F) can be obtained in high yield by introducing polyacrylamide (PAM) into a polyol synthesis (182). Here, PAM serves as a dual-functional agent in the synthesis. It can act as both a steric stabilizer to prevent the agglomeration of nanoparticles and can form complexes with Ag^+ ions. This coordination effect can slow down the reduction rate to enable kinetic control.

The rapid reduction of gold precursors in refluxing 1,5-pentanediol results in a series of gold nanocrystals in the shape of octahedra, truncated octahedra, cuboctahedra, cubes, and higher polygons by incremental changes of silver nitrate concentration, which may be attributed to the selective deposition of silver species on the seed surface during the reaction (183). In this case, silver species generated from $AgNO_3$ during the growth process determine the morphology of final nanocrystal by the selective growth of (111) and/or the restriction of (100). Single crystalline Au octahedral nanoparticles can also be synthesized in an ethylene glycol solution by a straight forward poly-(diallyldimethylammonium) chloride (PDDA)-mediated polyol route (184). Formation of Au nano-octahedra was attributed to the preferential adsorption of PDDA molecules on the (111) planes of Au nuclei that inhibit the growth rate along the (111) direction. By adjusting the pH of the solution, Au octahedra with different dimensions can be synthesized
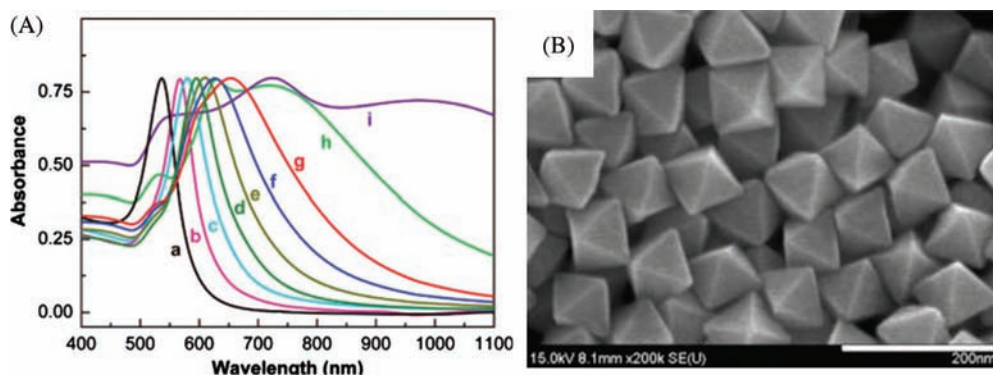
Fig. 14. UV-vis absorption spectra for Au octahedra with different edge lengths dispersed in water (A). The edge lengths of Au octahedra from curve 'a' to curve 'i' were 20, 50, 63, 80, 95, 110, 125, 160, and 230 nm, respectively. SEM images of Au octahedra with average edge lengths of 63 nm synthesized at 195°C by introducing 1 M HCl solution to the initial gold precursor. Scale bars: 200 nm. Reproduced with permission from Reference (184). American Chemical Society, Copyright (2008).

(Fig. 14B). A systematic increase in the UV-vis absorption maximum was observed as the edge length of the octahedra increases (Fig. 14A). The synthetic strategy has the advantage of one-pot and requires no seeds, no foreign metal ions, and no pretreatment of the precursor so that this is a practical method for controllable synthesis of Au octahedra.

3.3 Biological synthesis

Biological systems are capable of making functional superstructures of inorganic nanomaterials such as amorphous silica, magnetite (magnetotactic bacteria), and calcite (185). In biological systems, shape controlled synthesis of nanomaterials has been achieved either by growth in constrained environments such as membrane vesicles or through functional molecules such as polypeptides that bind specifically to crystallographic planes of inorganic surfaces. Single crystalline equilateral triangles (Fig. 15A–C) and hexagonal silver nanoparticles have been synthesized biologically using Pseudomonas stutzeri AG259 (186), a bacterial strain that was isolated

from a silver mine. Flat, triangular gold nanocrystals have been made using specific polypeptide repeat sequences in proteins secreted by the bacterium *Escherichia coli* (187).

Triangular gold nanoprisms (Fig. 16A) can be synthesized biologically (188) in high yield at room-temperature by the reduction of aqueous chloroaurate ions ($AuCl_4^-$) by the extract of the plant lemongrass (Cymbopogon flexuosus). During the reaction, a visible color change occurred from pale yellow to a ruby red, indicating the formation of gold nanoparticles. The reducing sugars (aldoses) present inside the lemongrass extract were found to reduce the Au^{3+} into nanoprisms. By simple variation in the concentration of the lemongrass extract in the reaction medium, it is possible to vary the size of the nanoprisms (189) thereby the longitudinal SPR band in the NIR region can be easily tuned (Fig. 16B). It is reported that tamarind leaf extract can also be used as the reducing agent for making gold nanotriangles (190). On treating aqueous Au^{3+} solution with tamarind leaf extract, rapid formation of flat and thin single crystalline
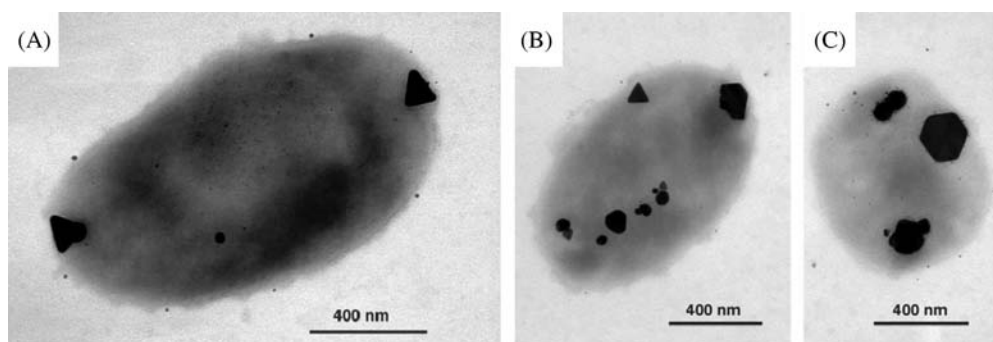
Fig. 15. (A) TEM image of large, triangular, Ag-containing particles at both poles produced by P. stutzeri AG259. An accumulation of smaller Ag-containing particles can be found all over the cell. (B and C) Triangular, hexagonal, and spheroidal Ag-containing nanoparticles accumulated at different cellular binding sites. Reproduced with permission from Reference (186). Proceedings of National Academy of Science, Copyright (1999).
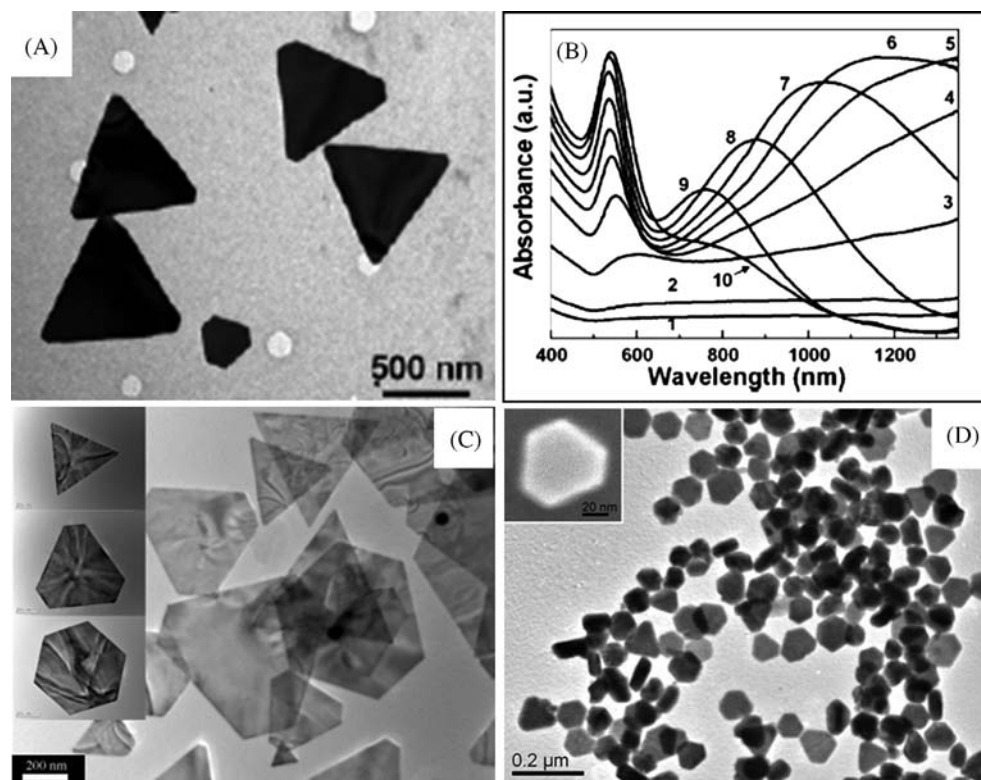
Fig. 16. (A) TEM image of gold nanotriangle synthesized by the reduction of aqueous $HAuCl_4$ solution with lemon grass extract. Reproduced with permission from Reference (189). American Chemical Society, Copyright (2005). (B) UV-vis-NIR spectra of gold nanoparticles synthesized by adding different amount of lemongrass leaf extract to 5 mL of 10^{-3} M $HAuCl_4$ solution. Curves 1–10 correspond to solutions with 0.2, 0.3, 0.4, 0.5, 0.6, 0.7, 0.8, 1.0, 1.2, and 1.6 mL of lemongrass leaf extract in 5 mL of 10^{-3} M $HAuCl_4$ solution, respectively. (C) TEM images of gold nanoplates synthesized by the reduction of aqueous $AuCl_4^-$ by seaweed extract. Reproduced with permission from Reference (192). American Chemical Society, Copyright (2005). Single-crystalline Ag nanoplates synthesized in aqueous medium at room temperature using an extract of the unicellular green alga Chlorella vulgaris (Fig. 13D). Inset shows the SEM image of a single Ag nanoplate. Reproduced with permission from Reference (193). American Chemical Society, Copyright (2007).

gold nanotriangles was observed. The effect of different organic solvent vapors like methanol, benzene, and acetone on the conductivity of these gold nanotriangles was investigated by measuring the I–V characteristics. The results suggest that these nanotriangles can be used as vapor sensors.

Cinnamomum zeylanicum leaf broth is another reducing agent that can reduce Au^{3+} into gold nanoprisms (191). Nanoparticles of diverse shapes such as hexagon, truncated triangle, and triangle can also be synthesized by reducing aqueous chloroauric acid solution with the extract of seaweed, Sargassum sp., at room temperature (192) (Fig. 16C).

Here, the seaweed acts both as the reducing agent and as the capping agents necessary for the gold nanoplate formation. During the nanoparticle growth, the capping agents may assist to limit the size and control the shape. It would bind non-specifically on all exposed surfaces of gold and lead the anisotropic growth. An extract of the unicellular green algae Chlorella vulgaris is also found to reduce Ag^+ into single-crystalline gold nanoplates in

aqueous medium at room temperature (Fig. 16D) (193). Proteins in the extract reduce the Ag ion into various nanoparticles. Hydroxyl groups in Tyr residues and carboxyl groups in Asp and/or Glu residues were identified as the most active functional groups for the reduction Ag ion and the anisotropic growth of Ag nanoplates, respectively. Chlorella vulgaris green alga can also reduce Au^{3+} ions into single-crystalline gold nanoplates at room temperature (194). A cell-free extract of Rhodopseudomonas capsulata has been used to synthesize Au NWs with network structures (195). Nanoparticles formed in bacteria are typically observed in aggregated state and, in several cases, polyhedral shapes are seen. Synthesis of such structures of gold and silver was reported by Nair and Pradeep (196).

### 3.4 Hydro/solvothermal synthesis

In this method, nanoparticles are synthesized in hot water/solvent in an autoclave under high pressure. Here, H_2O serves both as a catalyst and occasionally as a component of solid phases. The synthetic method is also

categorized as solvothermal (197), since various solvents can also be used, in accordance with the general process principle. It is also possible that additives are employed to modify the initial properties of pure hydrothermal water. In order to widen the range of applicability of this synthesis method, polar solvents (e.g. aqueous solutions containing hydrofluoric acid [HF], or other acids or bases to trim pH) or non-polar solvents (e.g. pure, supercritical) can be used for the dissolution–recrystallization process. Up to date, hydrothermal synthesis has been demonstrated for a number of different materials.

Ultralong ZnO NW/nanobelt arrays with honeycomblike micropatterns on zinc substrates were made under hydrothermal conditions in large scale (198). Novel Pd-Cd nanostructures with a high capacity for hydrogen storage were synthesized by this method. In this method, a series of Pd-Cd nanostructures with varying concentrations of Cd were directly grown onto Ti substrates using a facile hydrothermal reduction method (199). Uniform Cryptomelane-type manganese oxide (OMS-2) 3D dendritic and spherical nanostructures were synthesized under mild and organic template-free hydrothermal

conditions. In this case, by suitably adjusting the temperature, the shape evolution of OMS-2 was achieved (200). In the presence of an electric field, hydrothermal synthesis can yield hierarchical Co-doped ZnO hexagonal ring-like superstructures (Fig. 17A–C) composed of NRs (201). Here, the electric dipole interaction of NRs plays an important role in the alignment of NRs. Other interesting structures such as nanorings and microloops (Fig. 17D–F) of $Ag_2V_4O_{11}$ can also be synthesized by this method. In a particular synthesis, $AgNO_3$ and V_2O_5 powders were treated with distilled water at 170°C for 12 h in a hydrothermal bomb (202). Self-coiling of $Ag_2V_4O_{11}$ nanobelts happens during this hydrothermal process without the use of any template or organic surfactant and results in nanorings and loops.

Nanomaterials made of Bi_2S_3 of various morphologies, including NRs, dandelion-like nanostructures, nanoleaves, nanoflowers, and nanocabbages were successfully synthesized from a single-source precursor, $Bi(SCOPh)_3$ or multiple-source precursors by using a colloidal solution method or hydrothermal method (203).
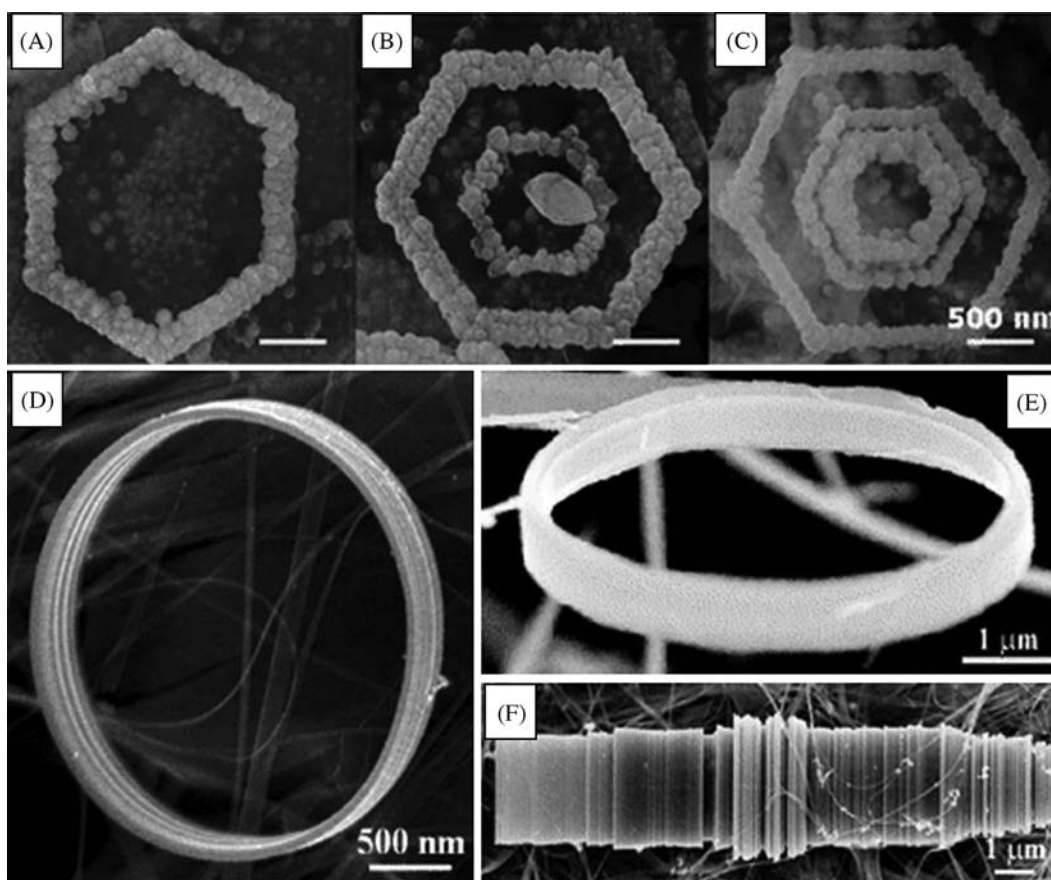
Fig. 17. SEM images showing (A) single-, (B) double-, and (C) triple-turn hexagonal ring-like superstructures of hexagonal single-crystals of Co-doped ZnO NRs. Reproduced with permission from Reference (201). American Chemical Society, Copyright (2008). D and E are SEM images of the $Ag_2V_4O_{11}$ nanorings (f) SEM images of the $Ag_2V_4O_{11}$ microloops formed by rolling of several nanobelts. Reproduced with permission from Reference (202). American Chemical Society, Copyright (2006).
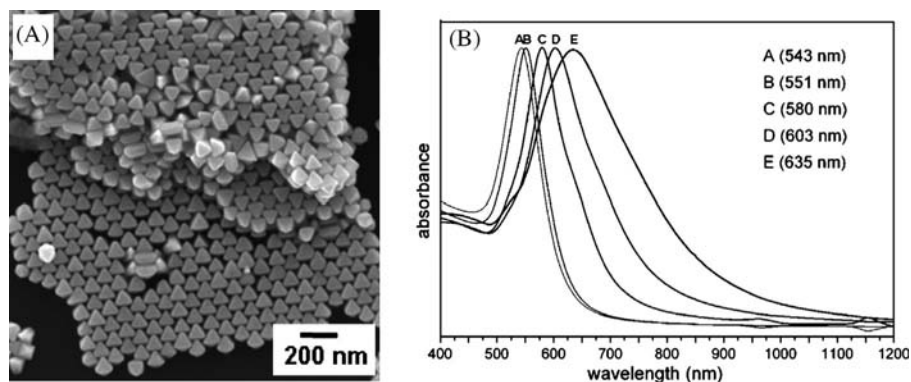
Fig. 18. (A) SEM image of the octahedral gold nanocrystals. The imaged regions show extensive self-assembled structures. (B) UV-vis absorption spectra of octahedral nanoparticles of different sizes. Maximum absorbance of the spectra has been normalized. Reproduced with permission from Reference (204). American Chemical Society Copyright (2008).

Octahedral gold nanocrystals (Fig. 18A) were synthesized via a hydrothermal method from an aqueous solution of $HAuCl_4$, trisodium citrate, and the surfactant, CTAB (204). These mixtures were heated at 110°C for 6, 12, 24, 48, and 72 h to obtain gold octahedra with approximate average sizes of 30, 60, 90, 120, and 150 nm, respectively. From the structural characterization, it was confirmed that the octahedra are bounded by (111) faces. The SPR were red-shifted from 543 to 635 nm (Fig. 18B) as the size of the nanoparticle increases.

Single-crystalline tellurium NWs were synthesized by the biomolecule-assisted reduction method under hydrothermal conditions (205). The biomolecule, alginic acid is used as both reducing agent and directional template. Wang et al. synthesized hexagonal tellurium nanotubes in poly(ethylene glycol) (PEG)-mediated hydrothermal method using tellurium powder as the tellurium source (206). The growth of nanotubes occurred through a dissolution–recrystallization process. Poly(ethylene glycol) was used to enhance the dissolution of tellurium powder into water and control the morphology to form nanotubes. They proposed that formation of tellurium nanotubes can happen by the combined effect of the selective adsorption of PEG on different crystal faces of tellurium and the insufficient feeding of tellurium atoms or atom clusters for the growth.

The hydrothermal method is an interesting synthetic protocol in various aspects since it is a low cost, environmentally friendly technique that can be used on large area as well as fabrication of many nanostructures. The low substrate temperature enables this method to create various nanostructures on temperature sensitive substrates.
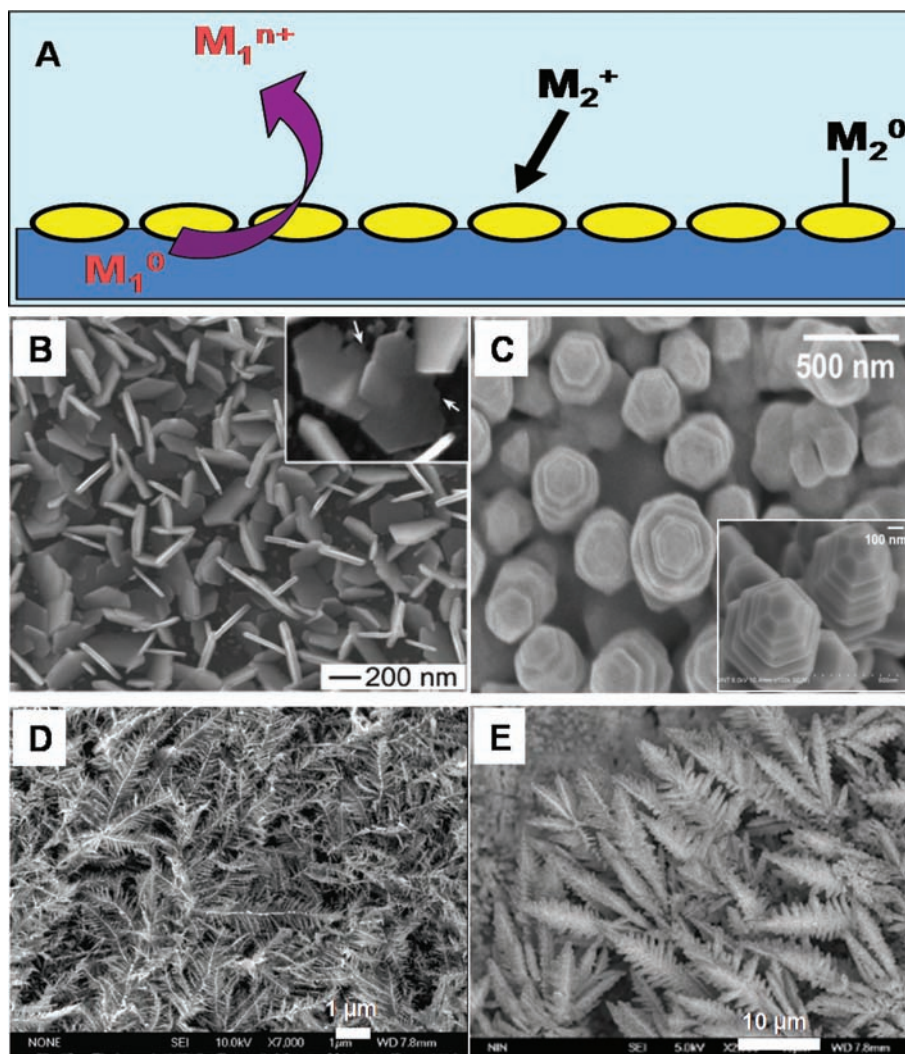
3.5 Galvanic replacement reactions

'Electroless' plating is a method introduced by Brenner and Riddell (207) to describe the spontaneous reduction of metal ions to metallic particles and films in the absence of an external electric field. This method has attracted attention due to its simplicity of operation, cost effectiveness, and it requires only simple equipment. This method is applicable to make a wide range of metal/substrate combinations including metal-on-metal, metal-on-semiconductor, and metal-on-insulator types. This is particularly important in the area of electronics with regard to metal deposition on a circuit board, for example. The process 'electroless deposition' includes three fundamentally different mechanisms such as auto-catalytic, substrate catalyzed, and galvanic displacement (immersion) processes in which galvanic displacement reaction proceeds in an entirely different manner and the deposition is carried out in the absence of an external reducing agent. Galvanic replacement reactions are single-step reactions that work based on the differences in the standard electrode potentials of various elements, leading to deposition of the more noble element and dissolution of the less noble component. The reducing electrons are derived from the valence band electrons of the substrate (Fig. 19A). The process will continue as long as oxidized substrate ions are able to pervade through the metal film into solution, or until a dielectric layer of oxidized substrate forms thereby arresting electron transfer.

A replacement reaction is a basic and simple method to synthesize nanostructured materials in a number of different systems. This method has advantages over other synthetic methods. For example, even though surfactant-based approaches have been used for preparing anisotropic nanostructures with smooth surfaces, the attachment of surfactant molecules present on the surface are not desirable for many applications. These can increase electrical resistance when the nanoparticles are used as conductive components in electronics. On the other hand, electroless deposition can avoid the use of surfactant molecules to produce metal nanostructures with various non-spherical shapes.

A simple method to synthesize nanoplates (Fig. 19B) of pristine Ag on semiconducting GaAs wafers has been

Fig. 19. (A) Schematic of galvanic displacement reaction. (B) SEM image of Ag nanoplates formed on the surface of n-type (110) GaAs wafer. Reproduced with permission from Reference (208). American Chemical Society, Copyright (2007). (C) Silver nano-inukshuks prepared by immersing n-type Ge(100) in aqueous AgNO₃ solution. Inset shows the close-up view of facets on the tips of silver metallic nano-inukshuks. Reproduced with permission from Reference (209). American Chemical Society, Copyright (2005). SEM images of silver (D) (Reproduced with permission from Reference (210). American Chemical Society, Copyright (2007)) and gold (E) (Reproduced with permission from Reference (211). Institute of Physics, Copyright (2006)) dendrites formed on zinc plates.

reported (208) through the galvanic reaction between an aqueous solution of AgNO₃ and GaAs (Equation III). In a typical synthesis, onto the GaAs wafer that is treated with aqueous hydrofluoric acid solution, a droplet of aqueous solution of AgNO₃ was placed to initiate the growth of silver nanostructures (and microstructures) via the galvanic reaction:

$$12AgNO_3 + 2GaAs + 6H_2O$$
$$\rightarrow 12Ag + Ga_2O_3 + As_2O_3 + 12HNO_3. \qquad (III)$$
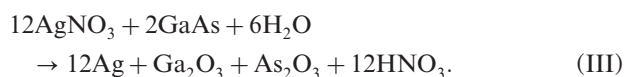
The morphologies and lateral parameters of Ag nanoplates can be successfully tuned by suitably adjusting the concentration of AgNO₃. At a high concentration of AgNO₃, an increase in the thickness of the as-grown Ag nanoplates was observed. In this case, germanium–germanium bonds in the crystal lattice provides the electron for the reduction of Ag^+ ions in solution, leading to Ag(s) and subsequent oxidation of Ge(s) into Ge^{4+} in a spontaneous redox reaction. The resulting Ge^{4+} product, germanium oxide, can be removed easily as it is soluble in water.

Silver nano-inukshuks (Fig. 19C), an unusual variety of Ag nanostructures, can be synthesized by immersing n-type Ge(100) in aqueous AgNO₃ solution (209). Silver nano-inukshuks are formed at concentrations around 10^{-3} M of aqueous AgNO₃ solution at room temperature on flat or rough, native oxide-capped germanium surfaces. The nano-inukshuks had 300 nm diameter

stacked hexagons with facets, and can grow perpendicular to the (111) planes of the silver hexagons. Different Ag salts such as $AgClO_4$ and $Ag(CH_3CO_2)$ can also yield nano-inukshuks. $AgSO_4$ consistently produces more flat dendritic structures. Inset of Fig. 19C shows the close-up view of facets on the tips of silver metallic nano-inukshuks. Through a simple electroless metal deposition route, gold dendritic nanostructures can be synthesized using $HAuCl_4$, H_2O, and zinc. The zinc plate was immersed in the container with $HAuCl_4$ solution, at room temperature and ambient pressure, resulting in dendritic nanostructures (Fig. 19E) (210). The same approach can be extended to make Ag dendritic nanostructures (Fig. 19D) (211).

Galvanic replacement reaction can be used as a versatile route to make metal nanostructures with controllable hollow interiors and porous walls. The replacement reaction between metal nanoparticle and a salt precursor containing a relatively less active metal plays an important role in this type of reaction. This method has been widely used to produce gold-based hollow nanostructures with different morphologies including cubic nanoboxes, cubic nanocages, nanorings, nanoboxes, single-walled nanotubes, and multiple-walled nanoshells or nanotubes (212–216). In addition to gold, hollow platinum and palladium nanostructures have also been synthesized by using appropriate salt precursors for the replacement reaction. These hollow and porous metal nanostructures show fascinating physical and chemical properties, which can be used for biological applications.

Ag nanocubes with truncated corners undergo replacement reaction, to form pores at the corners by the addition of Au^{3+} ions (212). A wet etchant such as $Fe(NO_3)_3$ or NH_4OH has been used for the selective removal of Ag from the Au/Ag alloy nanostructures after thin layers of Au have been deposited onto the Ag nanocube surface.

Au-based nanoboxes and nanocages can be synthesized by a template-engaged hollowing-out mechanism by the titration of an aqueous suspension of Ag nanocubes with an aqueous solution of Au^{3+} (212). Here, the Ag nanocubes act as a sacrificial template. During this process, $AuCl_4^-$ oxidizes the Ag template to AgCl. This is highly soluble in water at the elevated reaction temperature. The electrons generated in the oxidation process migrate to the Ag nanocube surface, which reduces Au^{3+} to Au atoms. The Au atoms can grow epitaxially over the Ag nanocubes since Au and Ag are having the same face-centered cubic structure with closely matched lattice constants. In the initial stage of the reaction, small pits are generated on the surface of each nanocube. This allows the ionic species to diffuse continuously in and out of the oxidation sites. As the reaction proceeds, this pit evolves into a deep hole, with
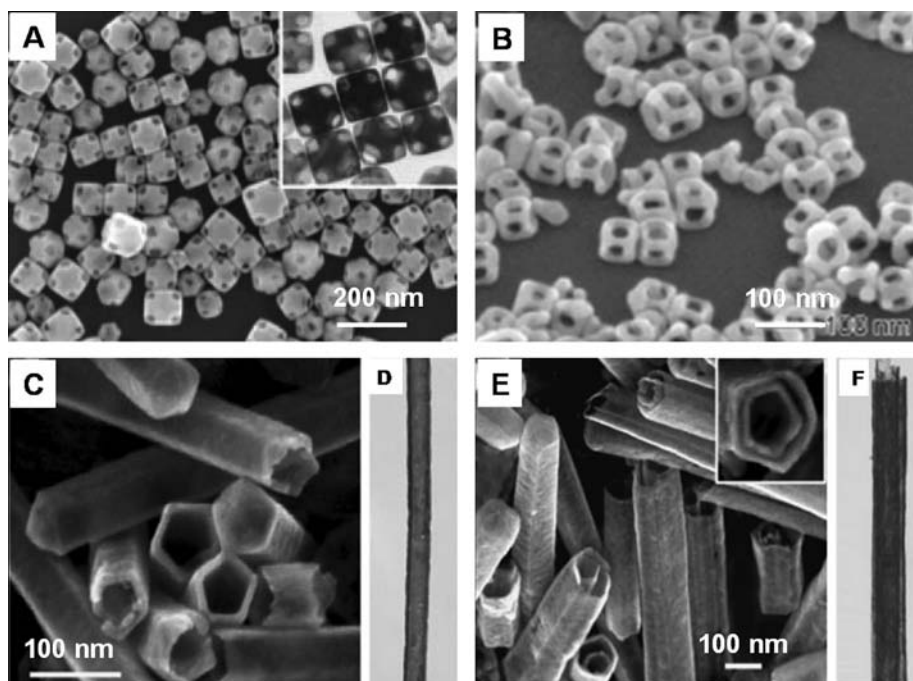
Fig. 20. (A) SEM and TEM (inset) images of Au nanocages. Reproduced with permission from Reference (212). American Chemical Society Copyright (2004). (B) SEM image of the Au nanoframes. Reproduced with permission from Reference (213). Copyright (2008) Springer. C, E are SEM images, and D, F are TEM images of single-walled nanotube of Au/Ag alloy and double-walled nanotube of Au/Ag alloy, respectively. Reproduced with permission from Reference (216). Wiley, Copyright (2008).

its opening at the surface eventually being closed, resulting in a seamless nanobox composed of Au/Ag alloy. Upon adding more amounts of Au^{3+}, dealloying of the nanobox happens that leads to the formation of Au-based nanocages with porous walls (212) (Fig. 20A).

Au nanoframes (213) (Fig. 20B) were obtained in high yield through a facile galvanic replacement reaction between Ag nanocubes and $AuCl_2^-$. Cubic nanoframes of Pd and Fe have also been reported (214). Here, Pd nanocubes were synthesized by reducing Na_2PdCl_4 in ethylene glycol, water, and PVP. The resultant solution then aged in an oxidizing environment that corroded the structures to form nanoframes. In the case of iron, nanoframes were synthesized from the thermal decomposition of a Fe(II)-stearate complex in the presence of sodium oleate and oleic acid (215).

The unique combination of the galvanic replacement reaction and the electroless deposition of Ag can also be extended to prepare metal nanotubes with single and multiple walls (Fig. 20C and E). Here, Ag NWs act as the sacrificial template (216). When Ag NWs were treated with aqueous solution of Au^{3+}, the galvanic replacement reaction generates a tubular sheath of Au, whose morphology is complementary to that of the Ag NW. Following the same procedure for multi-walled nano-shells, coaxial nanotubes with more than two walls can be synthesized.

3.6 Photochemical synthesis

It has been found that the reduction of metal salt precursors can also be done by radiolytic and photochemical methods. The main advantages of such a technique include the reduction of metal ions without using excess reducing agents. In this case, radiation is absorbed regardless of light-absorbing solutes and products. Also the rate of reduction reaction is known, since the number of reducing equivalents generated by radiation is well defined. Apart from this, photochemical synthesis does not require a specific and costly instrument.

Rod-like gold colloids were synthesized by the reduction gold salt by UV irradiation (217). In this method, gold salt ($AuCl_4^-$) binds to the rod-like micelle hexadecyltrimethylammonium chloride. The reduction of gold ion to Au^0 is achieved through photochemical reduction ($\lambda_{max} = 253.7$ nm). Synthesis of uniform rods and controlling the aspect ratio is apparently difficult in this method because an increase in the length of NRs also increases the concentration of spherical particles. Well-controlled aspect ratio and uniform NRs were synthesized using a photochemical method suggested by Kim et al. (218). This method is similar to the electrochemical method and used concepts from template-assisted synthesis. The solution contains a surfactant CTAB and tetradodecylammonium bromide and precursor HAuCl$_4$.3H$_2$O. The reduction of gold salt is achieved by

photo-irradiation for 30 h ($\lambda_{max} = 254$ nm, I $= 420$ μW/cm^2). Acetone and cyclohexane are used for loosening the micellar structure. The novelty of this method is in the use of silver nitrate for controlling the aspect ratio of the NRs. It is suggested that an increase in the silver ion concentration leads to a decrease in the aspect ratio of the NRs; in the absence of silver ion, the number of spherical particles was predominant.

Using a photochemical route, electrically conductive CdS NWs have been fabricated on DNA scaffolds. In this process, UV light was irradiated on a mixture, which contains cadmium perchlorate ($Cd(ClO_4)_2$) and thioacetamide (TAA). Obtained NWs were found to be electrically conductive and stable for more than 3 months without any changes in their optical properties (219). Crown-shaped platinum nanoparticles can be synthesized under UV-light irradiation in the presence of fourth generation NH$_2$-terminated (G4-NH$_2$) PAMAM (polyamidoamine) dendrimers. Aggregates of the G4-NH$_2$ PAMAM dendrimers formed in the aqueous solution served as templates for the formation of such crown-shaped nanoparticles (220).

A photo-induced method has been reported for synthesizing large quantities of silver nanoprisms in high yield in the form of a colloidal suspension (26). This photo-mediated route has led to a colloid with distinctive optical properties that directly relate to the shape. The initial step of the reaction includes the synthesis of spherical silver particles by the injection of NaBH$_4$ solution to an aqueous solution of AgNO$_3$ in the presence of trisodium citrate. Subsequently, as a stabilizing agent, Bis(p-sulfonatophenyl) phenylphosphine dihydrate dipotassium (BSPP) was added drop-wise. The system is then irradiated with a conventional fluorescent light. It is possible to tune the edge lengths of these nanoprisms to 30–120 nm range (221). The growth process can be controlled using dual-beam illumination of the nanoparticles, and appears to be driven by surface plasmon excitations. Depending on the illumination wavelengths, the plasmon excitations lead the fusion of nanoprisms. The observed bimodal growth process occurs through an edge-selective particle fusion mechanism, with four type-1 nanoprisms coming together in step-wise manner to form a type-2 nanoprism (Fig. 21). Gold nanorods with controlled aspect ratios have also been synthesized via a simple photochemical process in the presence of silver ions. In the photochemical approach, it has been noted that the amount of Ag^+ ions play a critical role in the formation of NRs with controllable aspect ratios instead of spherical NPs. The gold nanoparticles of various morphologies such as triangular or hexagonal shapes can be generated using the photoreduction method by mixing Au^{3+} with sodium oxalate and a reducing agent in aqueous solution under illumination of a mercury lamp for more than 10 min. The size of
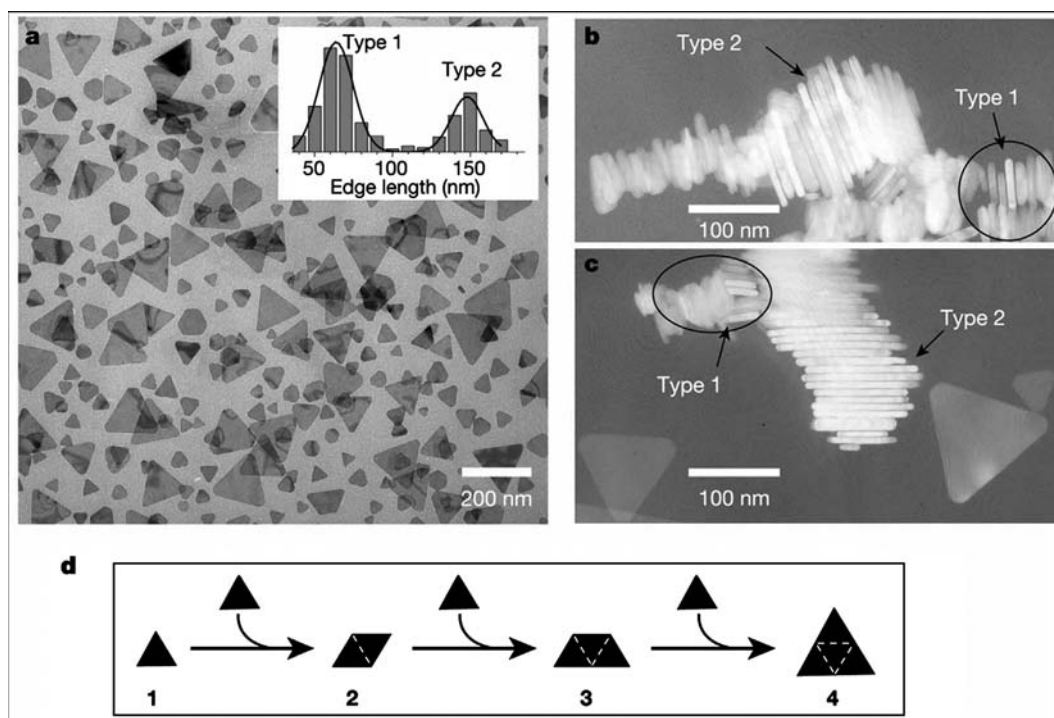
Fig. 21. The bimodal growth of Ag nanoprisms. (a) TEM image of a sample of Ag nanoprisms formed using single-beam excitation; inset, histograms used to characterize the size distribution as bimodal. B and C are the TEM images of nanoprism stacks showing that nanoprisms have nearly identical thicknesses. (d) Schematic diagram of the proposed light-induced fusion growth of Ag nanoprisms. Reproduced with permission from Reference (26). American Association for the Advancement of Science, Copyright (2001).
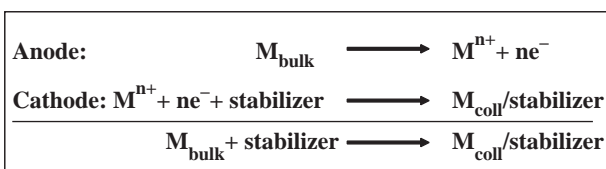
the gold nanoparticles varies from 25 to 200 nm, which mainly depends on the duration of light illumination and the concentration of sodium oxalate (222).

3.7 Electrochemical synthesis

Electrochemical methods have been widely used for making various nanoparticles, especially of noble metals. This technique has many advantages over other approaches since it has a lower processing temperature, high-quality products, use of modest equipment, and low-cost. In 1994, Reetz and Helbig showed that the electrochemical reduction method can be used for making highly size-selective nanoparticles by adjusting the current density (223). The experimental set-up contains a two-electrode setup for 50–250 mL electrolyte solutions in which the sacrificial anode consists of the bulk metal to be transformed into a metal colloid. In the overall process, the bulk metal is oxidized at the anode. At the

$$\text{Anode:} \quad M_{bulk} \longrightarrow M^{n+} + ne^-$$

$$\text{Cathode: } M^{n+} + ne^- + \text{stabilizer} \longrightarrow M_{coll}/\text{stabilizer}$$

$$M_{bulk} + \text{stabilizer} \longrightarrow M_{coll}/\text{stabilizer}$$

Scheme 1. Electrochemical synthesis metal colloids.

same time the metal cations migrate to the cathode, and reduction takes place with the formation of metal colloid in presence of a stabilizing agent (Scheme 1).

Gold nanocubes of uniform size can be synthesized by an electrochemical method using a surfactant solution and acetone (224). A two-electrode set-up can be used for this synthesis. The experimental set-up contains a gold plate and a platinum plate as the anode and cathode, respectively. These electrodes were placed vertically face-to-face inside the cell, which were separated by Teflon spacers. An aqueous solution of CTAB and a much more hydrophobic cationic co-surfactant tetradecyltrimethylammonium bromide were used as the growth solution. Apart from this, acetone was also added during the growth reaction. The electrolysis was carried out by constant ultrasonication, which resulted in the formation of Au nanocubes. During the reaction, gold at the anode was oxidized to gold cations, which is then migrated to the cathode where reduction occurs with the formation of gold adatoms (Fig. 22A). These adatoms were trapped by the surfactant to form nanocubes (Fig. 22B). The surfactant as the electrolyte and the stabilizer is generally regarded as a micelle template to control the size and shape of the nanoparticles. It was found that the shape of the gold nanoparticles can be changed by altering the rate of injection of acetone. At a lower concentration of acetone, spherical nanoparticles

Fig. 22. (A) Schematics of the electrochemical set-up used for the synthesis of gold nanocubes. (B) TEM images of gold nanocubes. Inset shows a SAED pattern taken from any individual nanocube by directing the electron beam perpendicular onto one of its square faces. (C) UV-vis absorption spectra of various gold nanoparticles obtained with different injection rates of acetone. Reproduced with permission from Reference (224). American Institute of Physics, Copyright (2008).

were formed. The UV-vis absorption spectra (Fig. 22C) of gold nanostructures were red-shifted as the amount of acetone injected was increased.

Gold nanorods have been synthesized via an electrochemical method using a simple two-electrode cell (225). Here, a gold metal plate is used as the anode and a platinum plate is used as the cathode. These electrodes are immersed in an electrolytic solution consisting of a cationic surfactant, CTAB, and a rod-inducing co-surfactant, resulting in the formation of GNRs. Using a standard three-electrode cell with a potentiostat, a platinum foil counter electrode and a saturated calomel electrode, platinum nanothorns were synthesized electrochemically at room temperature (226). Here, platinum nanothorns (Fig. 23) were electrodeposited on glassy carbon substrate in 2 mM K_2PtCl_6 and 0.5 M H_2SO_4 solution by applying a square wave potential between –0.20 and 0.80 V at 10 Hz for 20 min.

Single-crystalline Ag dendrites can be fabricated on the Ni/Cu substrate by using a templateless, surfactantless, electrochemical method (227, 228). The morphology and geometry of the Ag particles were controlled by the applied potential. When the potential was decreased from –0.4 to –2.0 V, the morphology of the resulting product was changed from Ag polyhedrons to Ag dendrites. These

dendrites grow preferentially along the (232) directions in a fractal mode.

3.8 Template-mediated synthesis

In recent years, the template-mediated method has become one of the most popular methods for the fabrication of 1D nanostructures with uniform size and controllable physical dimensions. This method has some obvious advantages over other methods such as easy fabrication (can be done in normal atmosphere), low cost, high-through-put, and adaptability to various compositions of materials (229–232). In this method, nanoporous polycarbonate or alumina is used as a template. The protocol is based on electrochemical deposition of metals such as Au in the template structure. To begin with, a small quantity of Ag or Cu is sputtered on the template in order to make a conductive film for electrodeposition. Thereafter, Au is electrochemically deposited on the conductive alumina template. The conductive film, based on Ag or Cu and the template, is removed by selective dissolution in the presence of a polymeric stabilizer (e.g. PVP). Finally, NRs are dispersed either in water or organic medium by means of sonication. Fig. 24 describes the template-mediated synthesis for the GNRs.
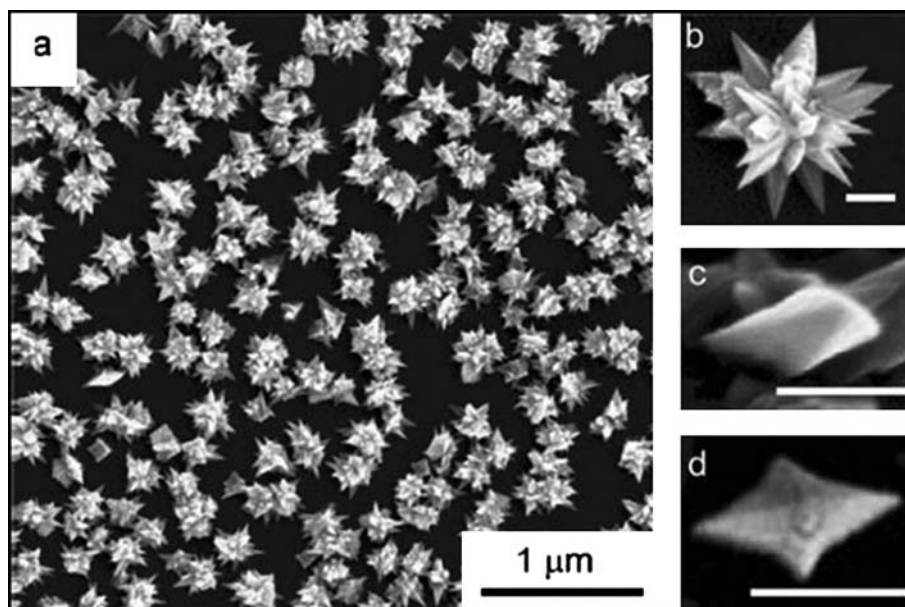
Fig. 23. SEM images of platinum nanothorns. (a) Large area SEM image; (b) high magnification SEM image of a platinum nanothorn; (c) side view of a nanothorn; (c) top view of a nanothorn. The scale bar in (b), (c), and (d) is 100 nm. Reproduced with permission from Reference (226). Royal Society of Chemistry, Copyright (2006).

The NRs of different diameters can be synthesized using this method by controlling the pore size of the template (233). Likewise, the length of the NRs is controlled by controlling the amount of gold deposited in the template (234).

4. Properties of anisotropic nanoparticles

The physical and chemical properties of nanoparticles depend on the type of motion its electrons can execute, which is dictated by the degree of their spatial confinement. The optical properties of colloidal nanoparticles in the UV-vis-NIR spectral range are mainly determined by the so-called localized surface plasmon resonance (LSPRs) (77, 235, 236). The optical features such as absorption, peak width, and so on depend on the shape, size, composition, surface charge, interparticle interactions, surface-adsorbed species, and the refractive index of the surrounding medium (237). Noble metal NRs are better examples to demonstrate the shape-dependent LSPR properties. The optical spectrum of rod-shaped anisotropic nanoparticles does not show only one well-defined resonance peak as in the case of nanospheres. They exhibit two bands in the vis-NIR spectral range. Theoretical studies suggest that the band near 530 nm is due to transverse LSPR, which is polarized across (corresponding to electron oscillation perpendicular to) the long axis of the NR, and the other one, appearing at a longer wavelength, has been assigned to a longitudinal LSPR mode, which is polarized along (parallel to) the long axis. For other anisotropic nanoparticles such as disks and triangular prisms, the LSPRs are typically split into distinctive dipole and quadrupole plasmon modes (238).

The plasmonic coupling between nanostructures in their assemblies gives rise to characteristic changes in the UV-vis spectrum. Unlike spherical nanoparticles, depending on the type of interaction, specific peaks change to different extent depending on the type of interaction.

The localized electromagnetic field surrounding the metal nanoparticles, generated by the excitation at their LSPR, is the direct consequence of the polarization associated with the collective oscillation of their electrons. In the case of a spheroid, the field enhancement will be higher at the tip (240, 241). Anisotropic metal nanoparticles show 'lightning-rod effect', another kind of field enhancement refers to an enhanced charge density localization at a tip or vertex of a nanoparticle. When an electromagnetic field (e.g. laser light) excites the free electrons of a metallic tip, a highly localized, strong electric field develops at these sharp tip or vertex with large curvatures, leading to large field enhancement in those regions (242, 243). This is the reason for the high SERS activity of an anisotropic nanoparticle.

The large surface area of anisotropic nanoparticles influences its chemical reactivity. It has been found that the rate of photochemical reaction of the molecules adsorbed on Ag nanoparticle can be controlled by the surface geometry of nanoparticles (244). During galvanic replacement reaction between nanoparticles and metal ions, shape anisotropy plays an important role in their chemical reactivity (245, 246).
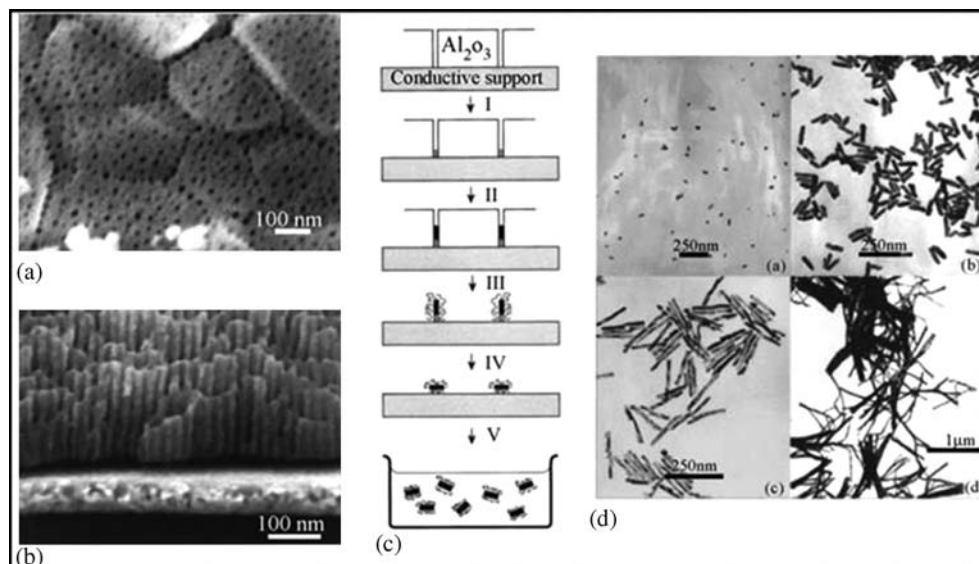
Fig. 24. (A and B) FESEM images of an alumina membrane. (C) Schematic representation of the successive stages during formation of GNRs via the template method. (D) TEM micrographs of GNRs obtained by the template method. Reproduced with permission from Reference (234). American Chemical Society, Copyright (2000).

Increasing the anisotropic nature of the nanoparticle can enhance its catalytic activity. Large surface areas for a given quantity of materials make them good for adsorption at specific sites. Studies on the platinum nanoparticles showed enhanced and selective catalytic activities for different morphologies compared to spherical nanoparticles (247, 248). Increasing the number of edges, crystallographic facets, corners, and faces are of critical importance in controlling the catalytic activity and selectivity of metal nanoparticles. It has been shown that cubic Pd nanoparticles had higher turnover frequencies compared to their spherical counterparts for the hydrogenation of butyne-1,4-diol and of styrene oxide (249).

5. Assembly of anisotropic nanostructures

Many of the properties of nanomaterials cannot be used for fruitful applications without assembling them properly. For spherical particles, since the interactions are the same in all directions, the collective effect and the resultant property of the assembly will be the same; only the extent of effect will vary depending upon the dimensionality of the assembly. But in the case of anisotropic nanoparticles, the inherent anisotropy makes the assembly and the interactions between nanoparticles direction-dependent. Various parameters play an important role in assembling nanoparticles in an ordered manner, without the formation of complex 3D aggregates. An overview of assemblies of various nanostructures and various forces inducing such assemblies has been presented in the following section.

5.1 Assembly of gold nanorods

Crystal structure has a crucial role in determining the assembly of nanoparticles. The surface structure of spherical gold nanoparticles are isotropic, mostly consisting of either (111) or (100) planes. The surface structure of GNRs is well studied (Fig. 25A and B) (170, 171). The side-faces of GNR are composed of (110) and the tips are composed of either (111) or (100). So, by the attachment of CTAB on to (110) due to its affinity, the conventionally less stable (110) gets extra stability and, hence, this facet becomes prominent in GNRs. Also the CTAB bilayer coverage on the side-faces will be thicker. Since CTAB has a lesser affinity to (111)/(100) faces, the amount of it present on the tip is lesser compared to the side-faces. Fig. 25B shows a lattice resolved image of a GNR showing the specific planes.

Due to the anisotropic crystal structure and the resultant difference in surface reactivity, anisotropic nanoparticles can be selectively functionalized to bring forth specific interactions between the constituent nanostructures giving different types of assembled structures. The amount of CTAB covering being less in the end-faces, functionalizing this facet is easy and specific functionalization of the end-faces can trigger the interaction of ends of NRs resulting in their end-to-end assembly. Another kind of interaction possible is in which the sides of the NRs are interacting with each other. The removal of CTAB from the side-faces comprising of (110) facet is considered to be difficult (the free energy of bilayer stabilization between CTAB molecules is found to be approximately 6 kJ/mol per two methylene groups). So functionalization of this face is done through rigorous procedures. This functionalization results in the side-to-
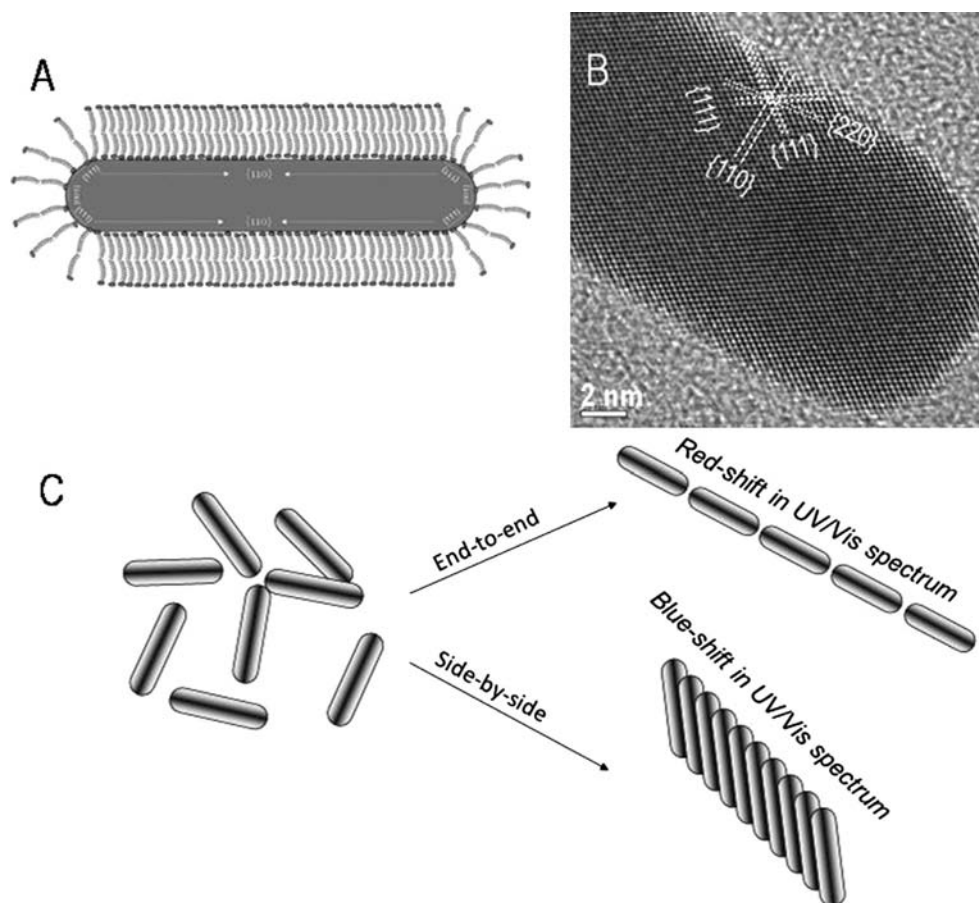
Fig. 25. (A) Schematic of a single GNR. (B) HRTEM showing the different crystal planes and lattice structure. (C) Schematic showing the different ways of arranging the NRs.

side assembly. The different interactions as well as different kinds of resultant assembly are depicted in Fig. 25C. It has been proven that a side-by-side assembly leads to a blue shift in the UV-vis spectrum whereas the end-to-end assembly gives rise to a red-shift (252). The extent of shift in the spectra depends on the extent of assembly also. In a 2D or 3D assembly where multiple interactions can be there, the resultant shift can be a combination of all these interactions.

When assembly happens without any external aid, it is called self-assembly. The GNRs are known to self-assemble under optimum conditions like concentration, pH, ionic strength, and so on. Self-assembly can be modified by controlling the interactions between the constituents. This is usually done by regulating the environmental conditions such as pH and ionic strength. This is often referred to as 'programmed self-assembly'. Chemical modifications or functionalization are usually done in order to control the assembly. Surface-functionalized GNRs, with specific molecular groups can lead to precisely controlled self-assembled structures. It is generally observed that programmed self-assembly with functionalized NRs can be an efficient means of nanofabrication owing to its simplicity, versatility, and low

cost. But this method normally provides ordered structures with a lesser area, and do not allow us to control over the design or interparticle distance in the NR architecture. The manipulation of the assembly after initiation is also very difficult normally. But with the advent of new techniques and with a better understanding of the system, these limitations are slowly getting negated. Depending upon the functionalizing molecule, the assembly can be formed through a wide variety of operating forces. The operating forces can be covalent, hydrogen bonding, electrostatic, biochemical interaction, van der Waals and dipole interactions, and so on. A brief discussion about different kinds of assemblies reported is presented in the following section.

5.1.1 Self-assembly of gold nanorods upon solvent evaporation

Since GNRs are covered with a stabilizing bilayer of CTAB, the suspension gets stabilized devoid of any tendency to aggregate due to the electrostatic repulsion between the head groups of CTAB on adjacent rods. But, when the excess surfactant is removed by centrifugation and the conditions like concentration, pH, ionic strength, and so on are optimum, there can be a situation where
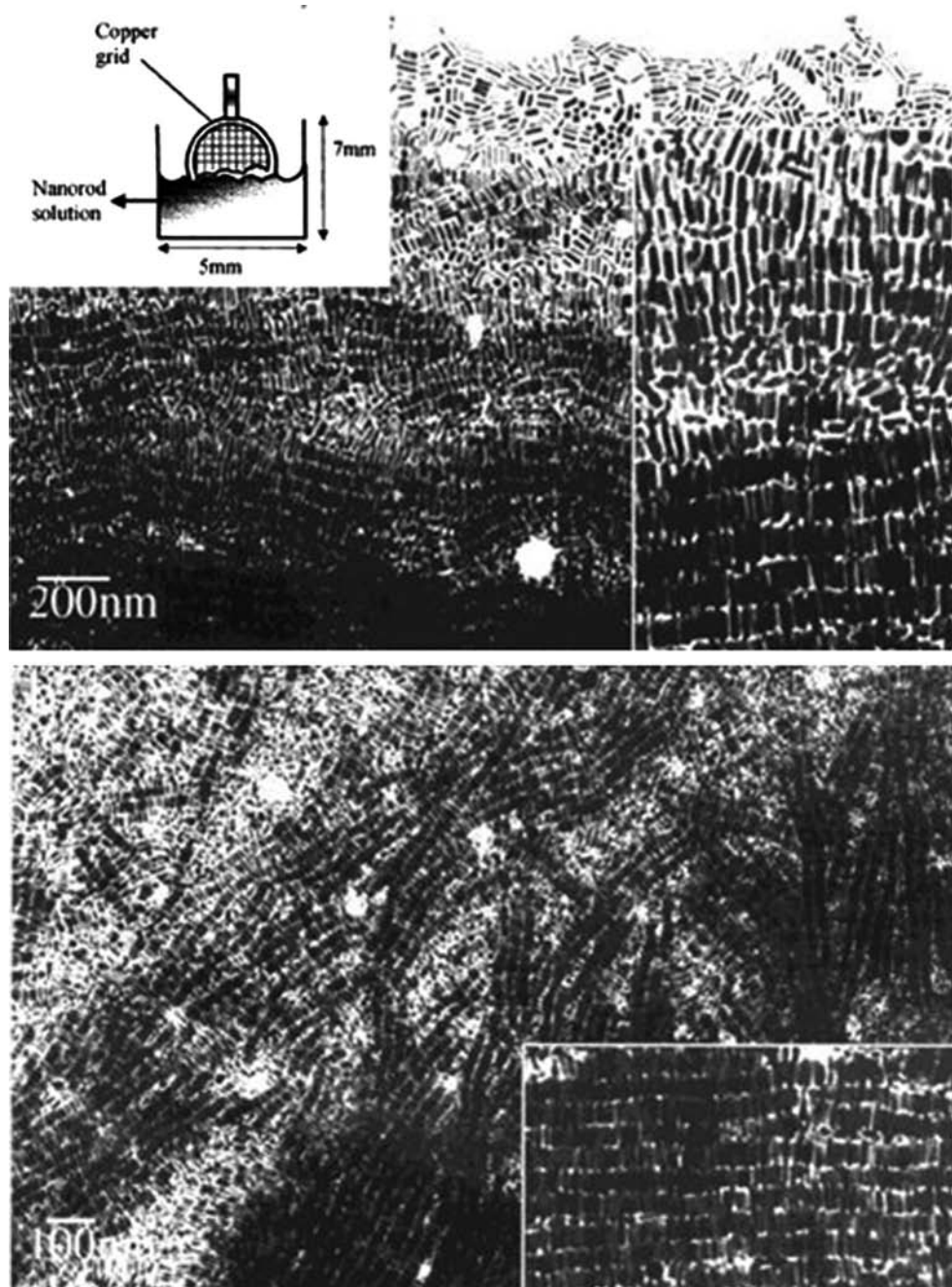
Fig. 26. Electron micrograph showing the border of the self-assemblies. The thickness increases from top to bottom. The inset shows a magnified part of an assembly. Scheme of the deposition method is also shown in the figure. Reproduced with permission from Reference (250). American Chemical Society, Copyright (2000).

the electrostatic repulsion is being compensated by the hydrophobic–hydrophobic interaction between the CTAB tails. This will facilitate the assembly of NRs where the distance between the NRs depends on the compensation of the above-mentioned interactions. So, upon solvent evaporation, the NRs tend to assemble at an optimum distance between each other where all the forces are compensated. One of the first attempts to study the self-

assembly of GNRs was by Nikoobakht et al. in 2000 (250). Electrochemically prepared GNRs (aspect ratio ∼4.6) were centrifuged at 14,000 rpm and were resuspended in water. It was diluted to an optical density of 1.5-1.7. Drop-casting of a 1:1 solution containing the above suspension and 0.1 M NaCl solution on the TEM grid was done in the way shown in the inset of Fig. 26. Upon solvent evaporation, they got long range 1, 2, and 3D

assemblies of GNRs over micrometer areas of the grid. Factors that can affect the assembly were also studied. The effect of free surfactant concentration, ionic strength, particle concentration, particle shape, size distribution, and the position of the grid in the solution were looked at.

The formation of assembly in the interface was explained by a theory originally explained by Dimitrov and Nagayama (251) According to this theory, the lateral immersion and/or capillary forces may be one of the main factors causing the self-assembly of particles confined in thin films. The operating force is believed to be dependent upon the interparticle separation, particle radius, and surface tension of the liquid and the corresponding meniscus deformation around the participating particles. The self-assembly process involves the convective transfer of particles from the bulk solution to the thin film due to the evaporation of solvent from thin film and the interaction between the colloidal particles in the thin film that lead to the formation of assembled structures. The driving force for the convective transfer is the evaporation of water from the film. One explanation given to the parallel assembly of NRs is that the higher capillary forces along the length of the NRs compared to those along the width. Lateral capillary forces are proportional to R^2, where R is the diameter of the particle. So, there is anisotropy in the interaction between the NRs and it may be an important driving force for the parallel assembly.

Later it was found that the removal of excess CTAB and at appropriate NR concentrations, they self-assemble without the addition of electrolyte (252). Large aspect ratio GNRs form liquid crystalline assembly when the as-prepared rods are centrifuged to remove the associated spherical particles and were redispersed in an optimum concentration of CTAB (1–100 mM). The assembly was proved using UV-vis and small-angle X-ray scattering (SAXS) measurements. With the same aspect ratio GNRs, different kinds of assemblies were found at different places on the grid. The reason behind this may be the difference in local concentrations created by inhomogeneities of the thin solvent film before the complete evaporation of water, creating unsymmetrical sections on the grid. The interparticle distance between the NRs was also found to be varying. This was explained to be due to the involvement of CTAB in facilitating this kind of assembly. When the solvent was evaporated, CTAB draw the nanocrystals closer and can either share a common layer or can interdigitate CTAB tails from neighboring nanocrystals. Therefore, the distance between the nanocrystals was found to be varying. Here, CTAB can act both as the protecting agent as well as the 'glue', facilitating the assembly. Self-assembly being a natural process may not have perfect long range order. As explained earlier, this can be overcome in assemblies by functionalizing the NRs in a desired manner.

5.1.2 Assembly involving biological interaction and biorecognition

In biology almost all functional entities are assembled structures. The operating forces in biology are very specific. Such interactions have been utilized to assemble GNRs. One of the first efforts in this direction was done by Dujardin et al. (253). The NRs were functionalized with thiolated DNAs in two different ways. In one case, two non-complementary strands of DNA were immobilized on the surface of two batches of GNRs. When they were mixed, no assembly was formed. But a third strand, half complementary to each of the grafted sequences, induced hybridization. In the second case, two directly complementary strands of thiolated DNA were anchored on to GNR. When they were mixed, through biorecognition between the complementary pairs, an assembly was formed. Fig. 27A and B shows the TEM images of the assembled structures and the associated UV-vis spectral changes during the assembly (Fig. 27C and D).

The GNRs, surface-functionalized with mercaptoalkyloligonucleotide, were assembled preferentially in an end-to-end fashion by the addition of a target oligonucleotide (254). Here, the thiol groups in the mercaptoalkyloligonucleotide binds to the ends of the NRs, which further assembles in an end-to-end fashion through hybridization with the target oligonucleotide. Oriented assembly of GNRs in solution by a biomolecular recognition system, where antigens specifically bind to antibodies was reported by Chang et al. (255). Thioctic acid (TA) was used as a binding agent in this work. The TA molecules were made to self-assemble onto GNRs. The rigid conformation of TA containing a disulfide and a ring structure facilitates the preferential binding of TA molecules to the ends of GNRs. The TA monolayer containing a terminal carboxyl group at the end surface of GNR opens up conjugation with various immunoglobulins (Ig), or other biomolecules. A similar approach to detect a protein like IgG was demonstrated by Wang et al. (256). They reported an enhanced detection limit of 60 ng mL^{-1} compared to that reported based on spherical gold nanoparticles, with a detection limit of 0.1 μg mL^{-1}. They observed aggregation of GNRs, oriented preferentially in a lateral (side-to-side) fashion, driven by the bio-recognition process. This was reflected in the LSPR bands. This makes them extremely sensitive reporters of molecular binding events with excellent biosensing capability. In principle, this method may be extended to act as a platform for using GNRs with various aspect ratios to develop multi-plex assays for the detection of molecular binding events (256).
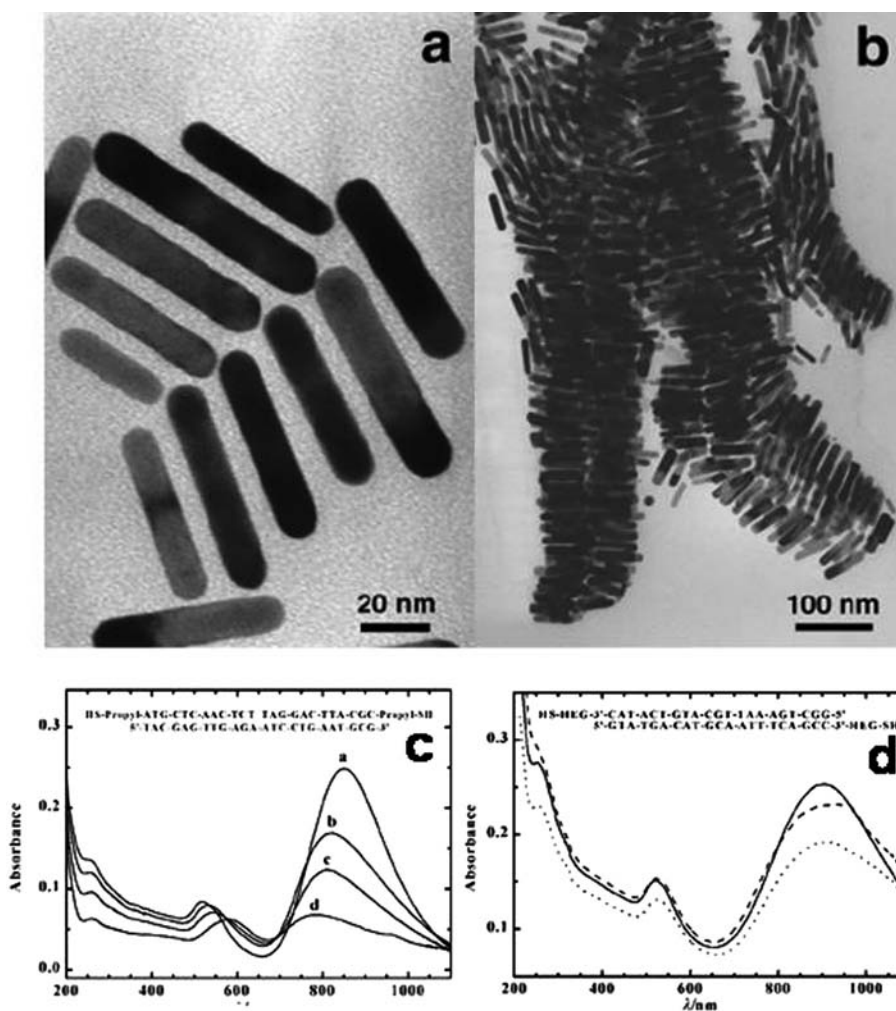
Fig. 27. TEM images of bundles of DNA-linked GNRs. (A) The three-strand (B) two-strand DNA linking systems. UV-vis spectra of (C) a suspension of non-complementary DNA functionalized NRs and (D) the two-strand NR system before (—) and after (····) duplexation at 25°C. Reproduced with permission from Reference (253). Royal Society of Chemistry, London, Copyright (2001).

Biotin-streptavidin interaction is one of the most common and strong non-covalent interactions known in biology. This interaction was utilized for the preferential end-to-end assemblies of GNRs. The GNRs were surface-functionalized with biotin disulfide and upon the addition of streptavidin linker; they assembled preferentially in an end-to-end fashion (256). Recently, Wang et al. reported a simple and versatile approach for the end-to-end assembly of GNRs through the specific molecular recognition between thymine rich (T-rich) oligonucleotides and mercury (II). Because of the specificity of the oligonucleotide, the process was found to be highly selective (258).

5.1.3 Assembly involving covalent bonding
The interactions between Au NRs and α,ω-alkanedithiols of varying chain lengths leading to the longitudinal assembly of GNRs was investigated using absorption spectroscopy and transmission electron microscopy by

Shibu Joseph et al. (259). The mechanism of the end-to-end assembly was investigated as well. They observed a decrease in the longitudinal plasmon absorption after the addition of dithiols. Simultaneously, a new red-shifted band appeared above the critical concentrations of dithiols due to the interplasmon coupling in assembled NRs. Below this concentration, no appreciable change was observed indicating that no assembly happens below this concentration. At the incubation step, one of the thiol groups of α,ω-alkanedithiols preferentially binds onto the edges of the NRs, leaving the other thiol group free. Above the critical concentration, through the inter-locking of NRs, the latter become initially dimers and subsequently oligomers, which results in longitudinal inter-plasmon coupling. This happens through the covalent binding of two thiol groups to form a disulphide. A clear isosbestic point was observed in the time-dependent absorption spectrum and TEM investigations proved the

formation of dimers and this confirmed the involvement of the dimerization step in the chain-up process. The study revealed that the process is not diffusion controlled but activation controlled with large activation energy (259).

5.1.4 Assembly through hydrogen bonding

The formation of cooperative intermolecular hydrogen bonding between two thioacids anchored on to the end-faces of GNRs were utilized to precisely control the longitudinal assembly and modulate the plasmon coupling. It was found that the plasmonic positions can be modulated by the concentration of thioacids added into the mixture. As the concentration increased, the plasmon shifted to a higher and higher wavelength. This

approach for connecting nanomaterials into desired shapes can be useful in tuning optoelectronic properties (260). Recently, Ni et al. investigated hydrogen-bonding-directed assembly of GNRs in aqueous solution (261). The mechanism behind the formation of end-to-end assembly of GNRs modified with bi-functional linking molecules was probed experimentally and theoretically.

5.1.5 Assembly through electrostatic forces

Electrostatic forces are one of the most common forces operating in the living world and in assemblies. Electrostatic interactions between the amino acids anchored onto the gold nanorod surfaces were utilized to assemble NRs (262). Two amino acids, namely cysteine and glutathione containing thiol moieties, when added into
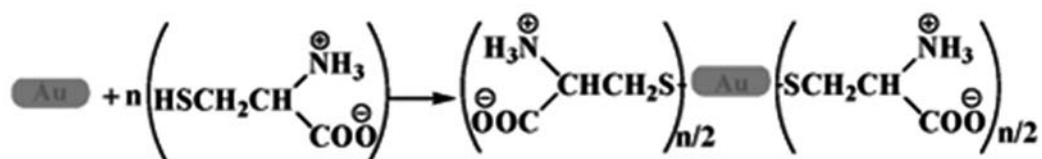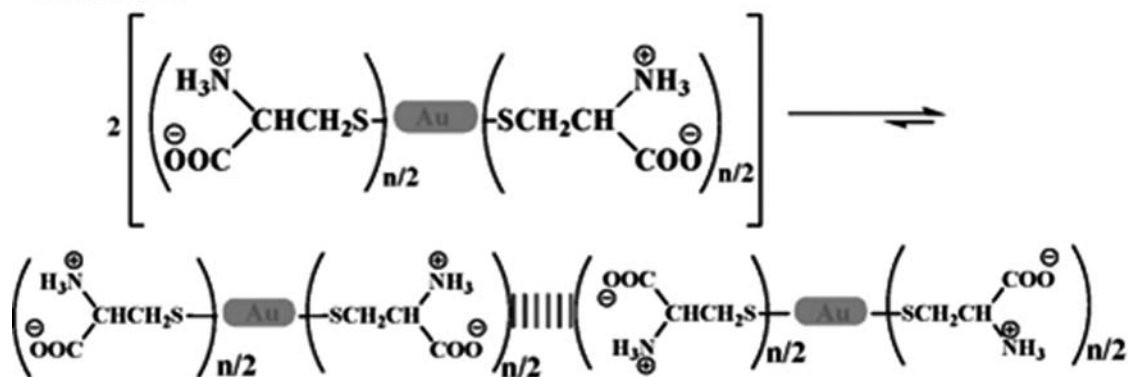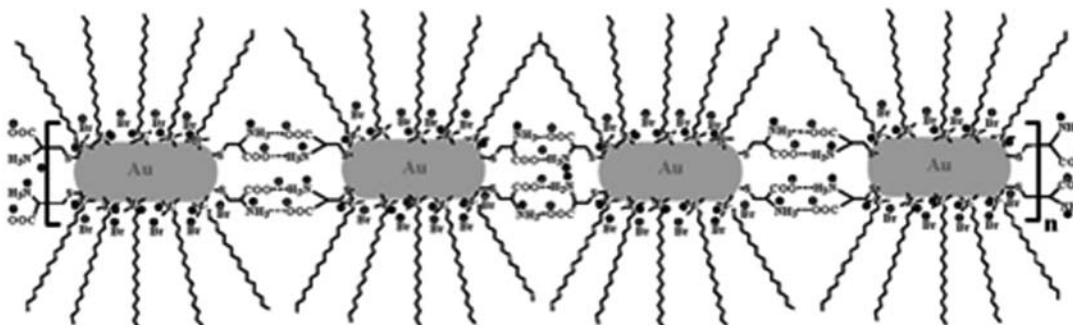
Fig. 28. (A) Schematic of the general mechanism of GNR nanochain formation due to electrostatic interaction due to cysteine and glutathione. Reprinted with permission from Reference (262). American Chemical Society, Copyright (2005).

the GNR solution gets anchored on to the GNR end-faces and because of the electrostatic interaction between the aminoacids, a preferential longitudinal assembly gets formed (Fig. 28). This results in the red-shift of the LSP. The change in the plasmonic characteristics was used for the specific detection of cysteine and glutathione in the micromolar concentrations in the presence of other aminoacids. Zhang et al. reported the assembling of bipyramids and rods into different types of nanoneck-laces using a similar approach (263).

For a particular concentration of assembly-inducing agents, the time-dependent shift in LSP was constant and was not controllable in any of the reports discussed above. A more controllable fabrication of GNRs in which the shift in the LSP can be stopped at the desired point to get a stable suspension with desired absorption regime was reported by Kawamura et al. (264). They found that the addition of sodium citrate into GNRs results in the gradual red-shift of LSP, which can be stopped at any point simply by the addition of CTAB into the reaction mixture. Added citrate anions get adsorbed onto the end-faces of GNRs preferentially, and will neutralize the surface charge of the GNR ends that results in the end-to-end assembly of the GNRs. Gold nanorods with an aspect ratio of 16 were found to be assembling in an end-to-end fashion upon decreasing the CTAB concentration
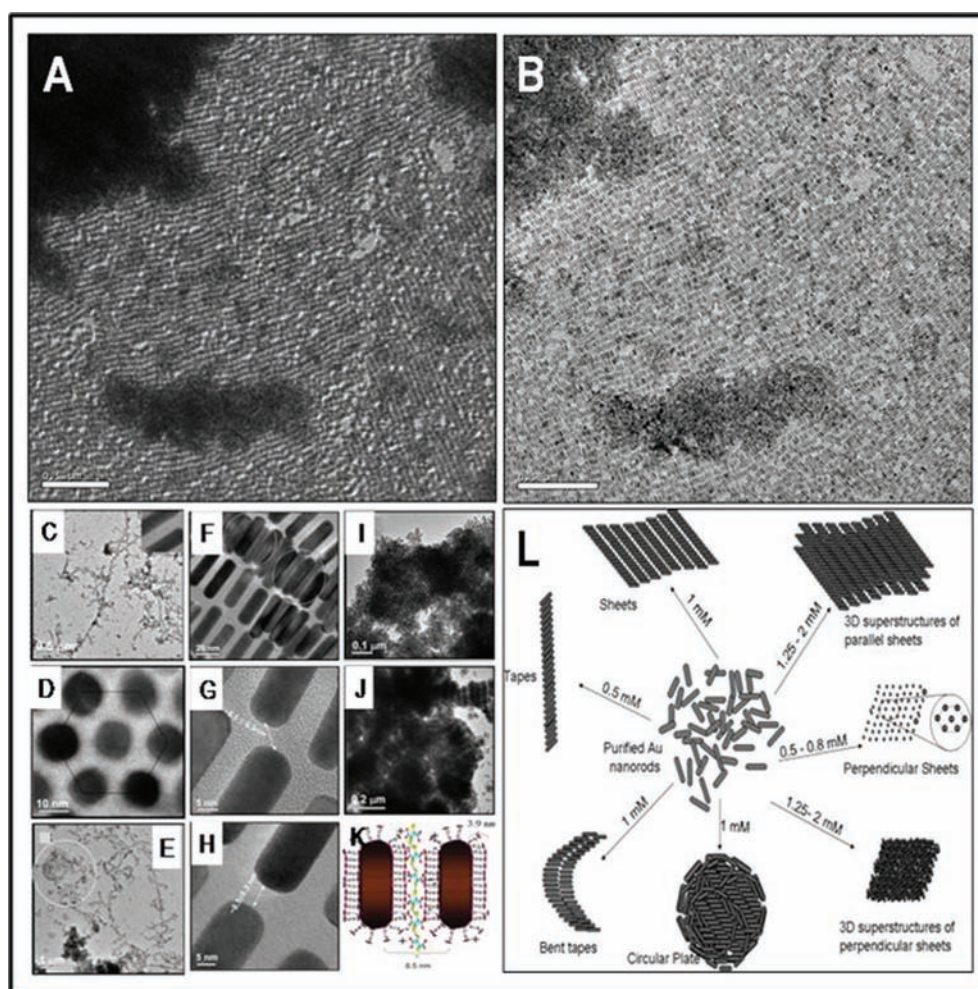
Fig. 29. TEM images taken in the (A) low MAG and (B) MAG I modes of the same area, showing self-assembly of NRs, induced by DMSA. Different self-assembled structures obtained at different concentration of DMSA; (C) a parallel assembly of NRs leading to a tape-like structure; (D) high-magnification image of perpendicularly oriented assembly showing the hexagonal nature of the rods, (E) circular structures and bent tapes; and (F) magnified portion of the same assembly showing the staggered configuration of NRs in the same plane. The NRs in the top layer (circled) are located in the grooves of the bottom layer. (G) and (H) High magnification images showing the spacing between the NR in a monolayer. TEM images of 3D superstructures formed by (I) perpendicular orientation and (J) parallel orientation with respect to substrate. (K) Schematic showing the mechanism of the self-assembly. (L) Cartoonic representation of various superstructures formed from Au NRs in the presence of different concentrations of DMSA. Reprinted from Reference (266). American Chemical Society, Copyright (2008).

in the solution. On further decreasing the CTAB concentration, the assembled GNRs were welded at their connecting points (264).

A pH-dependent self-assembly of GNRs of aspect ratio 3.3 ± 0.3 (20.6 ± 5.5 nm width) into ordered structures using adipic acid was reported by Orendorff et al. (265). Here, the electrostatic interactions between the cationic surfactant bilayer around the NRs and the negatively charged deprotonated adipic acid results in the pH-dependent self-assembly of NRs into 2D ordered structures. A similar method was adopted by Sreeprasad et al. (266) to assemble GNRs into 1, 2, and 3D super-structures (Fig. 29). They found that the addition of dimercaptosuccinic acid (DMSA) into the NR solution was found to induce self-assembly of the latter to 1D 'tape-like', 2D 'sheet-like', and 3D 'superlattice-like' structures depending on the DMSA concentration. A smectic structure where the NR long axes are parallel to each other was found to be followed all through the assembly. The effect of the DMSA concentration as well as the pH of the medium was also studied. The UV-vis spectral changes were visible immediately after the addition of DMSA into the NR solution. The peak position was found to be stable (after the initial shift) even after 24 h of incubation. A gradual shift was observed for LSP while TSP remained unchanged. The red-shift continued to increase as the concentration of DMSA in the solution increases. The width of LSP was also found to increase slightly. At lower concentrations, a longitudinal assembly formed that changed to lateral assembly upon increase of DMSA concentration. As the concentration was increased, the assembly changed from 1D 'tape-like' to 2D 'sheet-like' and finally to 3D 'superlattice-like' structures. At certain places the NRs were found to be arranging perpendicular to the substrate (TEM grids). Assembly was not observed at lower pH, lesser than the pKa of DMSA, where they are not ionized and hence cannot facilitate the assembly. On the basis of several control experiments utilizing similar molecules,

charge neutralization of the NRs by the carboxylic group of DMSA was found to be the principal reason for such an assembly, while the mercapto groups render additional stability to its structure. A mechanistic model of the assembly was also proposed (266).

5.1.6 Gold nanorod assembly involving van der Waals and dipole interaction

The GNRs, which are hydrophilic in nature, can be made hydrophobic by treating with mercaptopropyltrimethoxysilane (MPS) and subsequently octadecyltrimethoxysilane (ODS). Mitamura et al. found that such hydrophobic NRs can be arranged into well-ordered 2D or 3D structures on a substrate by solvent evaporation (267). The hydrophobization was done in three steps: (1) binding MPS onto the NRs, (2) hydrolysis of methoxysilanes, and (3) immobilization of ODS by dehydration condensation through which a hydrophobic covering was created on the NR surface. Two-dimensional assemblies were dependent on the concentration of the NRs. At a low concentration, the NRs assembled parallel to the substrate, whereas they stood on the substrate at a high concentration (Fig. 30). In vertical assembly of the NRs, they arranged in a hexagonal array. When the NRs were in solid state, it was observed that they formed a 3D assembly, where the GNRs were arranged in a hexagonal close-packed structure by their side-by-side interaction leading to a lamellar structure over small regions. The assembly was believed to be initiated by the interaction between NRs caused by the induced dipole moment, in addition to the steric hindrance. The induced dipole moment that gets generated by the instantaneous polarization or fluctuation of electron density in the NR induces oppositely directed polarization in the adjacent NRs. This results in the generation of a dipole–dipole interaction between adjacent NRs. Since the induced dipole moments can be more effectively compensated in the side-by-side interaction, this leads to an assembly that is preferentially side-by-side. A surface-directed, lateral or
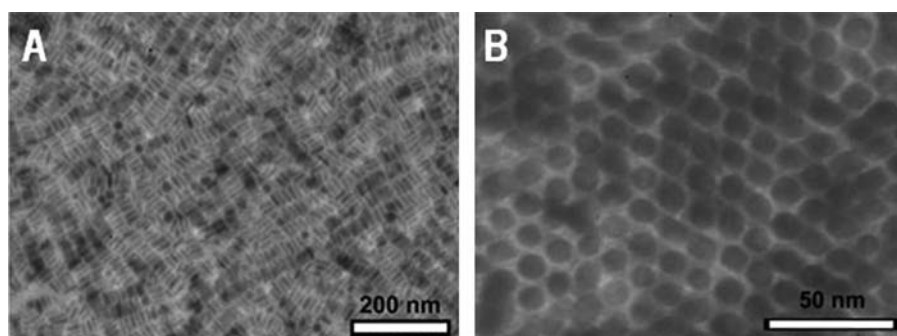

Fig. 30. TEM images of assemblies of hydrophobic GNRs arranged (A) parallel (B) perpendicular to substrate. Reprinted with permission from Reference (267). American Chemical Society, Copyright (2007).

perpendicular assembly of GNRs was reported by Nakashima et al. (268). A peptide called 1,2-dipalmi-toyl-sn-glycero-3- phosphothioethanol (DPPTE) was synthesized, and anchored onto GNR surface. The self-assembled superstructures of the complex were dependent on the drying method and the hydrophilic or hydrophobic nature of the Si surface. The GNR-DPPTE complex formed characteristic 1D and 2D self-assemblies induced by intermolecular interactions of surface-anchored lipids via a controlled drying process. The combination of solvent evaporation from the sample drop and interfacial hydrophilicity or hydrophobicity led to a variety of self-assembled features. A pH-dependent reversible end-to-end assembly of GNRs functionalized with disulfide-modified poly(L-glutamic acid) was reported by Walker and Gupta (269). The changes were induced by changes in the secondary conformation of the peptide with changes in pH.

Recently, through bis(terpyridine)–metal connectivity, GNRs were assembled, disassembled, and reassembled by Chan et al. (270). Using ((disulfide-modified terpyridine)$_2$–M(II)) (M = Fe or Cd) interconnectors, end-to-end linear and branched assembly of GNRs into multi-component structures were made. The prepared ((terpyridine)$_2$–M(II) complexes were unstable in basic conditions and hence the addition of NaOH resulted in disassembly. When the metal used for assembly was Cd, which forms labile complexes with bis(terpyridine), the assembly was found to be labile. In the presence of small concentrations of Cd, assemblies get formed. In the presence of excess Cd(II) ions they disassemble. When Fe(II) was added into this disassembled system, they again reassembled into end-to-end chains. This assembly can be again disassembled by a mere change in pH as mentioned above (270).

5.1.7 Assembly on templates

The GNRs have been arranged over templates as well. The first work in this direction was done by Correa-Duarte et al. (271). They have used multi-walled carbon nanotube (MWNT) as templates. They first interchanged the CTAB covering on GNRs with PVP. The MWNTs were coated with a polyelectrolyte, mainly polystyrene sulfonate (PSS), followed by PDDA. This wrapping produces adsorption sites on the carbon nanotube (CNTs) on which GNRs can get deposited electrostatically. This resulted in a preferential end-to-end assembly of GNRs forming a string-like alignment (Fig. 31). The resulting nanocomposites showed broadened absorption features, because of the end-to-end plasmon coupling between neighboring NRs in the string-like alignment. They also proved that these NRs can serve as a label to monitor the alignment of carbon nanotubes within polymer films (271, 272).

Rings of nanorods, where the drying droplet acts as the template, was demonstrated by Khanal and Zubarev (273). They described a simple and quantitative method to form rings of GNRs. A spontaneous assembly of hybrid gold/polymer core-shell NRs into ring-like arrays was seen where the rings are templated by water droplets that condense on the surface of non-polar solvents from humid air (273).

A solution phase method for assembling NRs into a hexagonal pattern using microgels was reported by Kumar et al. (274). The GNR-coated poly(N-isopropyl acrylamide) (PNIPAm) microgels were synthesized. Here, microgels were loaded with CTAB-coated gold nanoparticles of 4–5 nm size, which were used as seed particles and GNRs were synthesized via seed-mediated growth method. By this method, the required population of NRs on the microgels was achieved (Fig. 32A and B). These NR-loaded microgels were allowed to self-assemble and they formed a hexagonal pattern (Fig. 32C and D). Similar experiments were done with nanoparticle-coated or prefabricated NR-coated microgels, which did not give such hexagonal patterns because of the reduced number density of the nanoparticles. The interpenetration and interlocking of the NR structures were thought to be the reason for the formation of these patterns (274). The affinity of NRs for PNIPAm-based microgels allows their sequestering by cationic, anionic, and close-to-neutral-state microgels as reported by Das et al. (275). They made
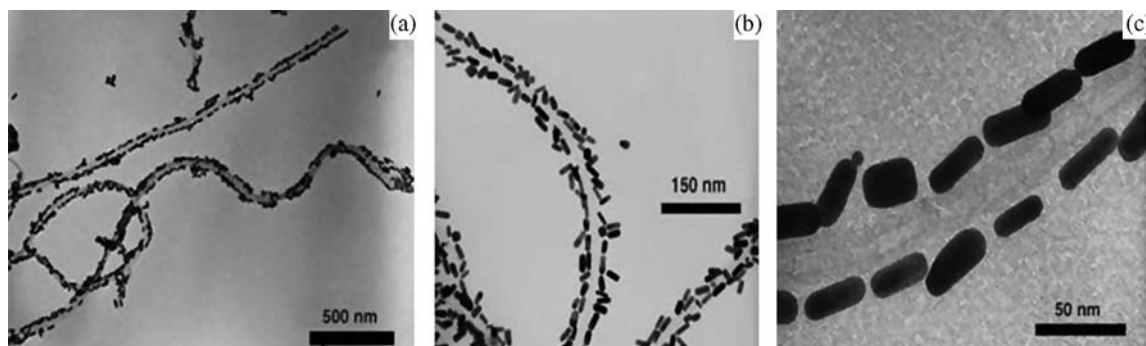
Fig. 31. TEM images of Au NRs (average aspect ratio 2.94), assembled on MWNTs (average diameter 30 nm) at various magnifications. Reproduced with permission from Reference (271). Wiley-VCH, Copyright (2005).
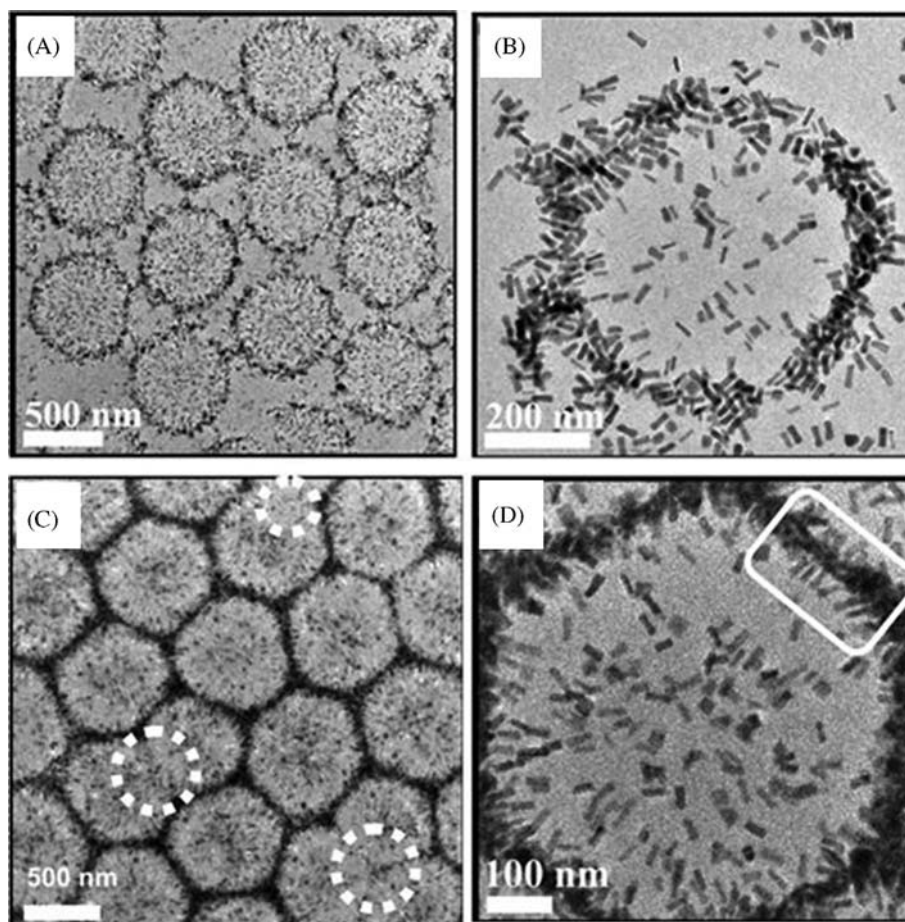
Fig. 32. (A) and (B) TEM images of the GNR-PNIPAm composite. (C) Large-area image of the hexagonal pattern with defect sites marked with dashed circles. (D) Higher magnification image of the one cell of hexagonal pattern confirming that the anisotropic structures sitting on the microgels are GNRs. Reproduced with permission from Reference (274). American Chemical Society, Copyright (2008).

the prepared microgels cationic, anionic, or near-neutral by adjusting the pH of the solution. The GNR got sequestered independent of the charge of the microgel when added into the above solution. Their results suggest that electrostatic interactions alone are not governing the loading of microgels with NRs. By the assembly of GNRs on silica particles using electrostatic interaction and subsequent coating of silica with controllable thickness were made by Wang et al. (276).

5.1.8 Assembly on substrates

Highly aligned Au NRs grown directly on a NH_2-functionalized Si (100) were reported by Mieszawska et al. (277). A remarkable degree of parallel alignment is observed over large areas. They did not find any arrangement when similar reaction was done on amorphous glass. But since the alignment direction changes throughout the sample showing no direct correlation with the arrangement of Si atoms, they concluded that the crystallinity of the substrate is not the critical factor of the assembly. The mechanism of the assembly is still not

well understood. The alignment was not observed on mercaptopropyltri-methoxysilane (MPTMS)- and aminopropyltriethoxysilane (APTES)-functionalized or bare Si(100). This indicates that surface chemistry plays a major role, but the role of the amidation reaction on the alignment is not clear. Surface hydrophobicity does not affect the alignment that was evident since acetic and succinic acid surfaces both showed alignment (277). Honda et al. showed end-to-end alignment of phosphatidylcholine-passivated GNRs adsorbed on polyanion-modified glass substrates (277). A patterned silicon substrate with hydrophobic stripes was successfully applied for growing gold NR superlattices by Zhang and Imae (279). The formation of perpendicular superlattices was also possible through this method. The substrate surface was found to be a crucial factor for the assembly. The NRs should be either positively attracted or not repelled by hydrophobic surfaces for forming a well-defined assembly. When the silicon substrate was hydrophilic, NRs preferred to stay in the solvent. The uniformity of particles without shape

difference is essential for the assembly. A protocol to directly grow end-to-end assembled structures on a substrate into long chains attached on top of a mixed self-assembled monolayer (SAM) that has been functionalized with streptavidin was reported by Zareie et al. (280). They were able to get assemblies that extend over a micrometer in length with 5 nm inter-rod separation.

5.1.9 Assembling by polymer tethering
Fava et al. (281) and Nie et al. (282, 283) reported a new way of self-organizing GNRs into a predefined pattern by attaching multiple polymer arms termed as 'pom-poms' (281–283). In the DMF/water mixtures, NRs end-terminated with polystyrene (PS) molecules self-assembling into higher order structures. The ordering is determined by the length and distribution of PS molecules between the ends of NRs and the longitudinal facet of NRs. The assembly was controlled by changing the structure of the polymer pom-poms. The variation in the molecular weight of the polymer molecules and their relative location with respect to the long side of the NRs resulted in different kinds of NR assemblies namely bundles, bundled chains, and chains involving side-by-side and end-to-end assembly. The change from one form to another can also be controlled by changing the concentration of water in the system. They found that the evolution of self-assembled structures of GNRs end terminated with polystyrene molecules takes place through competition between side-to-side and end-to-end assembly. Different solubilities of the polystyrene and the CTAB-coated metal blocks in the solvent mixture give rise to this competition. Tendency toward side-to-side aggregation was found to be dominant over most of the compositional range. At high DMF or water content and at very low THF/DMF weight ratios, this tendency gets reduced significantly (281–283).

5.1.10 Layer-by-layer assembly of gold nanorods into gold nanorod films
A strategy for assembling GNRs into 2D arrays at a water/hexane interface without the aid of any linker molecule was reported by Yun et al. (284). In this method, the film thickness can be controlled systematically and they obtained aggregates of GNRs with a relatively clean surface with controlled NR density. Hydrophilic nanoparticles have a contact angle of <90° at a water/hexane interface and will be suspended in the aqueous phase. But the particles tended to adsorb to the water/hexane interface when their contact angle is approximately equal to 90°. A medium having high dielectric constant can separate the charged particles from each other. When a miscible solvent with a lower dielectric constant is added into this, the dielectric constant of the medium gets decreased. The surface charge of the particles also decreases progressively as a function of the amount of the miscible solvent added. Upon the addition of ethanol to water/hexane interface, the surface charge density of the nanoparticles decreases. So the nanoparticles are brought to the interface. The driving force for the entrapment of nanoparticles is the reduction in interfacial energy at the water/oil interface upon the reduction of the dielectric constant of water. The thickness-dependent SERS of the adsorbed molecules on this NR films were studied and found that NR films have an order of magnitude stronger SERS enhancement than the nanosphere films under similar experimental conditions (284).

5.1.11 Gold nanorod assembly by surface anchored crown ethers
Assembly of GNRs end functionalized with crown ethers and initiated by the addition of specific metal ions was reported by Nakashima et al. (285). Two thiol-modified crown ethers, 2-((6-mercaptohexyl)oxy)methyl-15-crown-5 (15-crown-5-SH) and 2-((6-mercaptohexyl)oxy)methyl-12-crown-4 (12-crown-4-SH) were synthesized. These were added to the purified NR solutions upon which the crown ethers get attached covalently onto the end-faces of the NR through the thiol moieties. Addition of specific metal ions corresponding to the anchored crown ethers resulted in the assembly of NRs. The structure of the GNR aggregates, assembled side-to-side and end-to-end, was found to be dependent on the concentrations of crown ethers and cations added. Corresponding changes were observed in the absorption spectrum as well. The longitudinal absorption intensity of the NRs gradually decreased and the peak was initially red-shifted and then blue-shifted. When K^+ was added into the solution, it formed a 2:1 sandwich complex between the 15-crown-5 moiety and coupling of the plasmon absorbance occurred. The changes in the spectral features were used for the specific detection of metal ions.

5.1.12 Gold nanorod assembly induced by magnetic field
Pt-doped GNRs were homogeneously coated with metallic Ni through hydrazine reduction in aqueous solutions, leading to quasi-epitaxial growth of Ni shell on GNRs (Fig. 33A and B) (286). Pt acts as a 'nucleation agent' and because of its higher redox potential, it can be much more easily reduced than nickel, leading to the formation of small nuclei on which Ni is catalytically reduced. The Ni coated GNRs (Au@Ni NR) were allowed to dry on a TEM grid under the influence of an external magnetic field (0.2 T), and the NRs tend to align in a chain-like structure in the direction of the applied field (Fig. 33C). The orientation of individual rods within the chains was not found to be the same and both the 'side-to-side' and 'end-to-end' assembly was found to be co-existing. This reveals the complex magnetic response of the system (286).
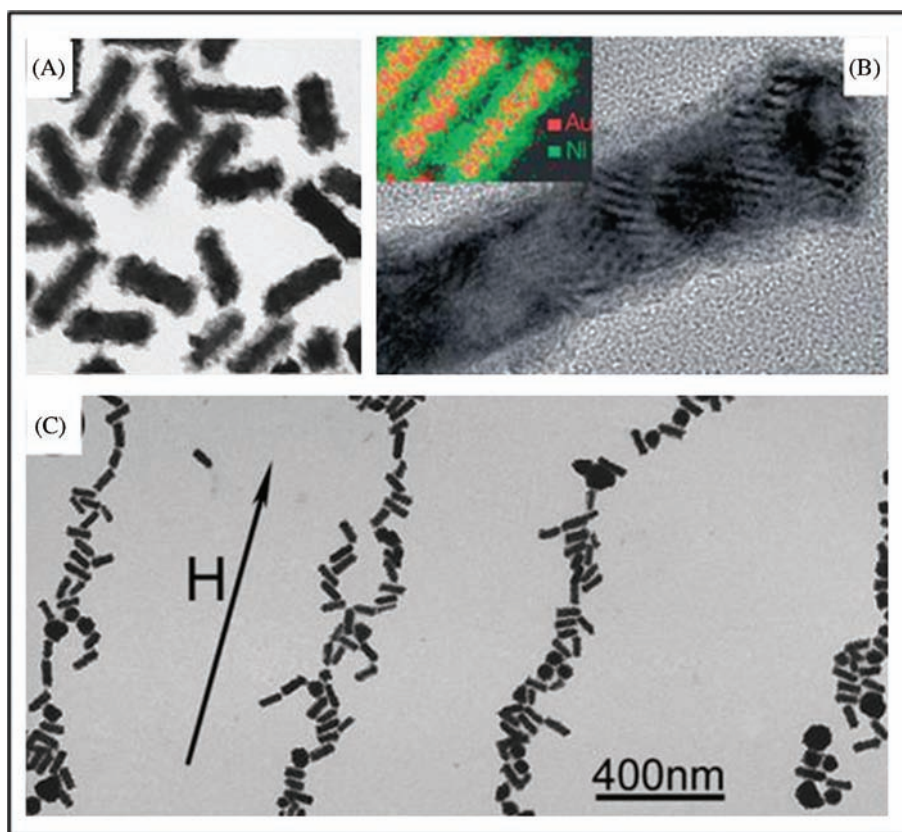
*Fig. 33.* (A) Large area TEM of nickel-coated GNRS in the absence of magnetic field. (B) High magnification image of a single Au@Ni NR. Inset shows STEM–EDAX (scanning transmission electron–energy dispersive analysis of X-rays) analysis of Au@Ni NRs, showing the relative distribution of the elements (Au = red; Ni = green). (C) Au@Ni NRs, dried on the TEM grid under an external magnetic field (0.2 T). Reproduced with permission from Reference (286). Wiley-VCH, Copyright (2007).

5.2 Assembly of various anisotropic nanostructures of silver

Anisotropic nanostructures of silver are more diverse compared to gold. But the synthesis of these structures in a monodisperse fashion is often a tedious job. The advancement in nanotechnology has enabled us now to prepare these particles either in a monodisperse manner or size select and separate the nanostructures post-synthetically to yield highly monodisperse samples. Since all these synthetic strategies involves surfactants to cap the formed nanostructures and to avoid them getting aggregated, the surfactant induced assembly of these structures upon solvent evaporation is highly probable similar to GNRs. Following a similar strategy to that used for making GNRs, Jana et al. (287) devised a seed-mediated growth approach for the preparation of silver NRs of varied aspect ratios. They found that after shape separation, these rods self-assemble in a 2D smectic liquid crystal-like manner upon slow solvent evaporation (Fig. 34A) (287). Recently, Pietrobon et al. (288) reported a new method to produce monodisperse size-controlled faceted pentagonal silver NRs by thermal regrowth of decahedral silver nanoparticles using citrate as the reducing agent. Because of its monodispersity, these

NRs showed great tendency to self-assemble into smectic mesophases like densely packed rafts and 3D arrays upon drying the dispersions (Fig. 34B–H). Even though the NRs are having fivefold symmetry, the 3D arrays followed a hexagonal arrangement. They found that slower solvent evaporation (>5 min) as well as a NR concentration in the range of 2 and 5 mM (in terms of silver) is favorable for the assembly. They also found that the order between the layers can be disturbed very easily but within a single layer the arrangement is always consistent. Here, the fivefold symmetry of the constituent NRs is always over-ridden by the long-range hexagonal order within the layers. This might be because fivefold symmetry is not compatible with close packing that result from evaporation-induced self-assembly. They also studied the dependence of aspect ratio of the participating NR on the assembly and found that well-defined layered structures start to be observed for the pentagonal AgNRs with an aspect ratio of 2. When the aspect ratio reached 4, there was not enough mobility for the NRs to self-assemble and only local ordering was found. An aspect ratio of 2.5 was found to be optimum for the best possible assembly (288).
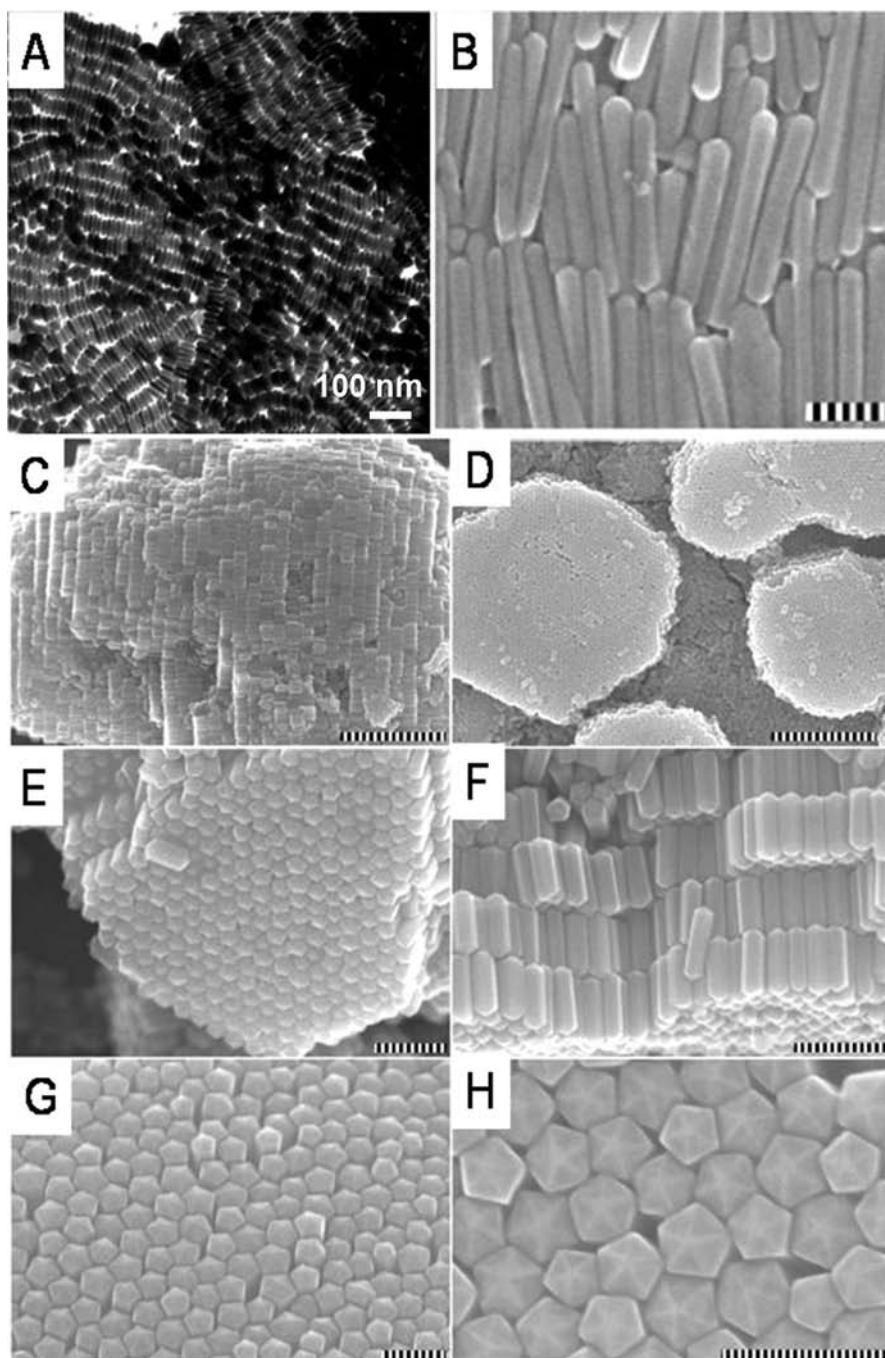
Fig. 34. (A) TEM image of shape-separated silver NRs self-assembled on TEM grids. Reproduced with permission from Reference (287). Royal Society of Chemistry, London, Copyright (2001). (B) SEM images of longer pentagonal faceted rod AgNRs aligned on a glass plate. (C)–(F) SEM images of self-assembled packing of monodisperse faceted pentagonal rod AgNRs with different aspect ratio forming 3D superlattices. The scale bars in B–H are 1 μm. Reproduced with permission from Reference (288). by the American Chemical Society, Copyright (2009).

The Langmuir-Blodgett (LB) technique is one of the most used methods to assemble a large-area monolayer of nanosystems. Using this technique, NWs that are ∼50 nm diameters and 2–3 μm length were assembled into a large area of about 20 cm^2 by Tao et al. (289) (Fig. 35). The PVP capping of the as prepared NWs were changed with 1-hexadecanethiol ligands, making them hydrophobic.

The hydrophobic NWs redispersed in chloroform were then dispersed onto a water surface of the LB trough and were assembled through the LB method. The NWs were aligned side-by-side over large areas, similar to a nematic 2D ordering of a liquid crystal. These aligned NW areas exhibited alternating extinction patterns when the sample was rotated every 45° (289). Following a similar
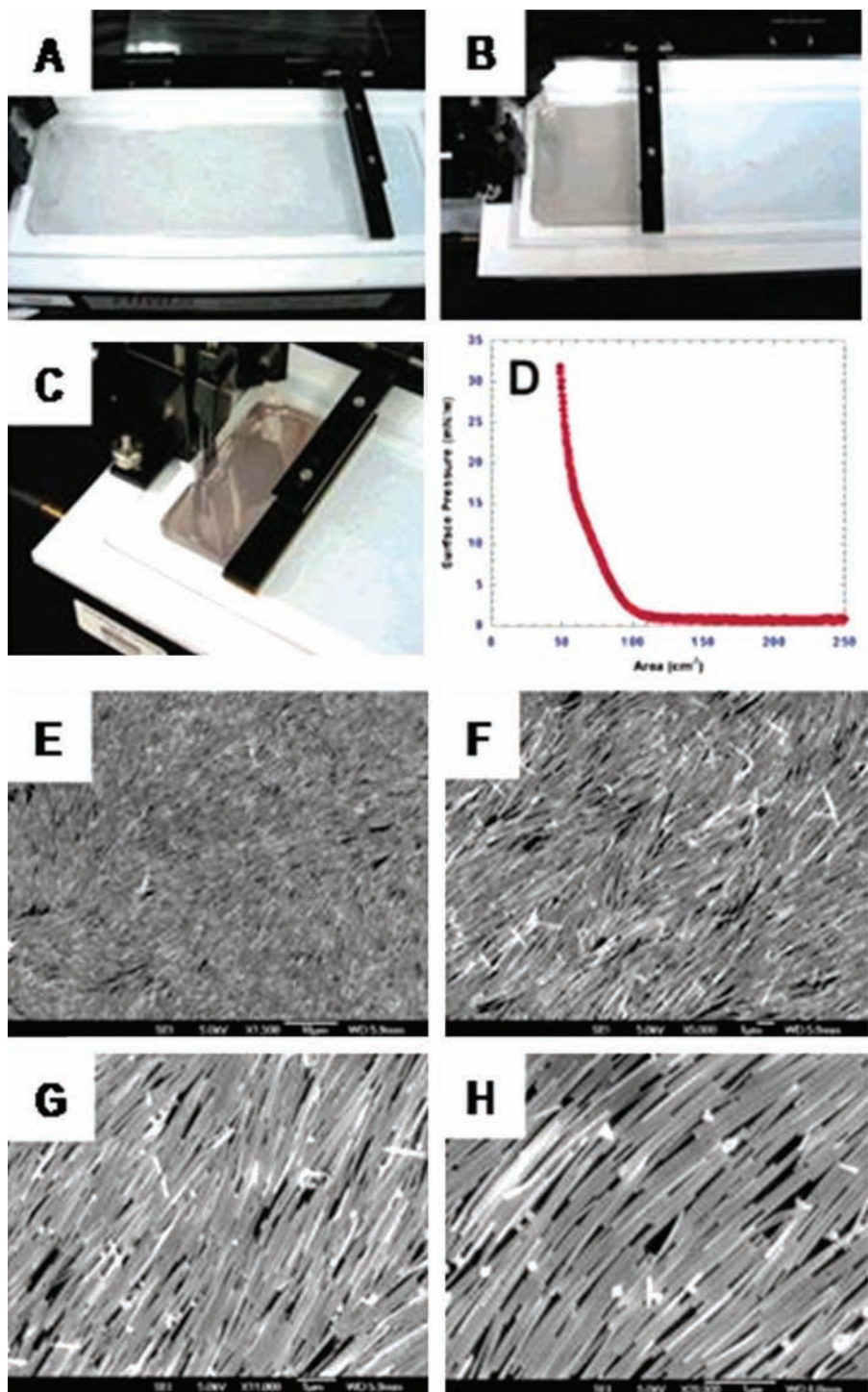
Fig. 35. (A–C) Photographs of LB NW assembly process at different compression stages. (D) Surface pressure curve recorded during the process. (E–H) SEM images (at different magnifications) of the silver NW monolayer deposited on a silicon wafer. Reproduced with permission from Reference (289). American Chemical Society, Copyright (2003).

methodology, the same group was able to create novel superlattice architectures composed of different polyhedral building blocks such as truncated cubes, cuboctahedra, and octahedra of Ag nanocrystals (290). They found

that the choice of nanocrystal building blocks determines their packing and dimensions of the assemblies created. Truncated cubes formed a square lattice by assembling in a face-to-face manner. More truncated polyhedral
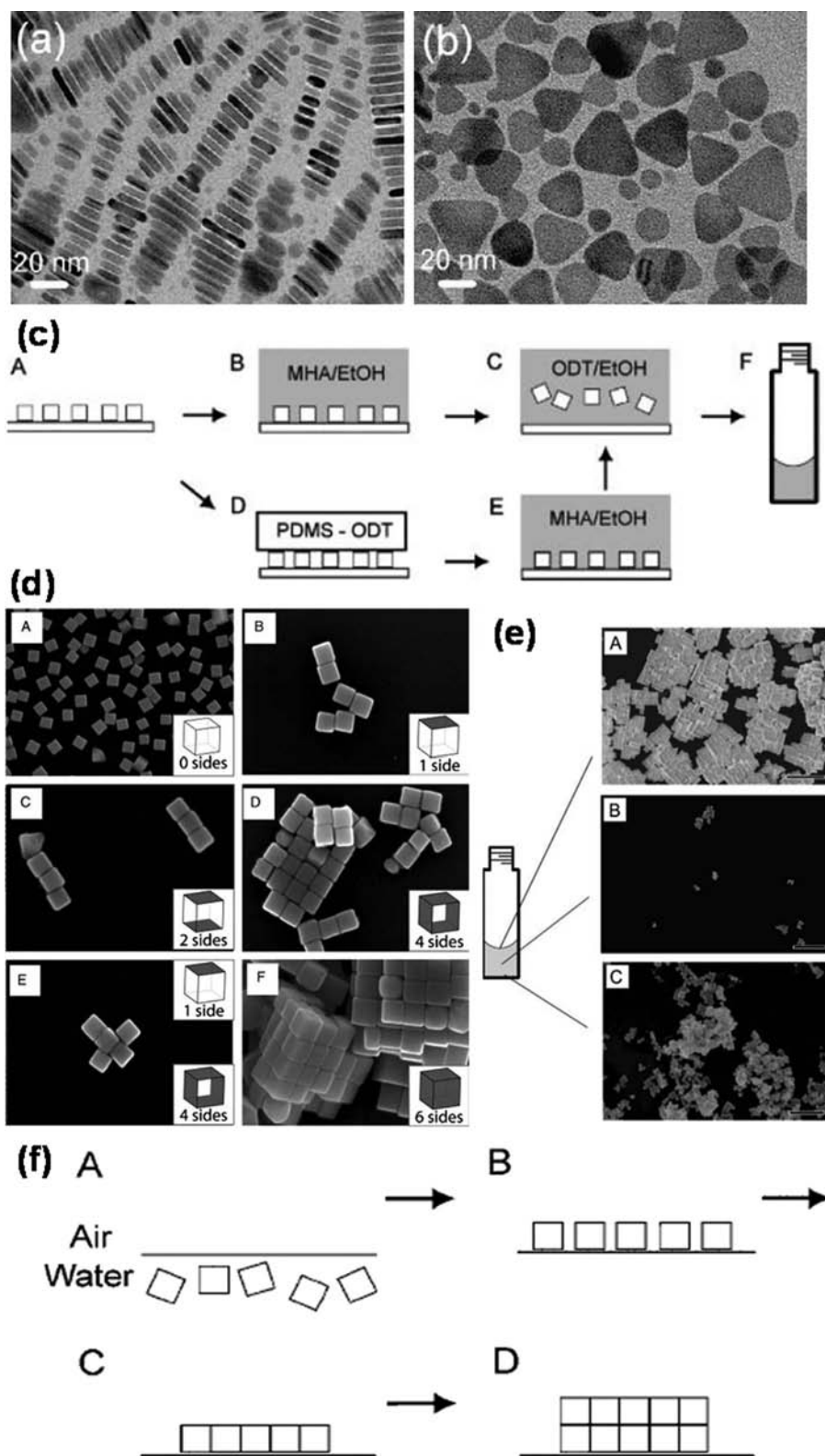
Fig. 36. TEM images of assembly A (A) and B (B). Reproduced with permission from Reference (291). American Chemical Society, Copyright (2008). (C) A schematic representation of specific functionalization of Ag nanocube faces. (D) SEM images of Ag nanocubes and the assemblies dependent upon the functionalization. (E) SEM images of ODT-functionalized Ag nanocubes sampled at different parts in a reaction vessel. (F) Schematic depicting the mechanism of formation of self-assembly at the air-water interfaces. Reproduced with permission from Reference (292). Wiley-VCH, Copyright (2008).

particles like cuboctahedra are arranged to form a rhombohedral unit cell, which is getting formed by the shears experienced by the square lattice (290).

The assembly of Ag nanoprisms (Fig. 36A and B) was reported by Bae et al. (291). They were able to assemble the prisms with anisotropic orientation and studied the orientation-dependent properties of these assemblies. Two kinds of assembled structures were fabricated. One was fabricated simply by dropping Ag nanoprism solution onto clean substrates like glass, ITO glass, Si, and TEM grid and solvent was allowed to evaporate slowly (Assembly A). They found that upon solvent evaporation, nanoprisms tend to stack face-to-face in rows with their edges perpendicular to the substrate. The nature of the substrate used did not have any effect on the alignment of the nanoprisms and they assembled with upright orientation on all the substrates. This is explained to be due to the higher attractive force between nanoprism faces than that between the face and substrate. The second kind of assembly was made by using the interfacial entrapment method (Assembly B). In this, a crown ether derivative that can transfer Ag nanoprisms from water to the water/oil interface was used. This leads to the self-assembly of nanoprisms at the liquid/liquid interface in face-down fashion (291).

Assembly of Ag nanocubes by the selective functionalization of each face selectively was reported by Rycenga et al. (292). Five distinct SAM-modified Ag nanocubes were prepared from the possible combinations of hydrophobic and hydrophilic faces and were assembled into four different nanostructures and one microstructure (Fig. 36C–F). The assembly was explained on the basis of hydrophobic interaction and solvation-free energy. Due to a hydrophobic driving force that is proportional to the solvation-free energy of the water surrounding the SAM-functionalized Ag nanocubes, they are brought together with their hydrophobic faces adjacent and parallel to form assembled structures. Depending upon the number of hydrophobic and hydrophilic faces present on each cube, the enthalpy or the solvation-free energy will be varied. The self-assembly is facilitated by the drive to reduce solvation-free energy by reducing their hydrophobic surface area exposed to the solvent, in this case, water. The procedure adopted for the selective functionalization of Ag cube faces is given in Fig. 36C. The selective functionalization was carried out by protecting Ag nanocube faces in contact with a clean Si substrate and functionalizing other faces sequentially with solutions of alkanethiols and PDMS inked with alkanethiols. An aqueous suspension of nanocubes is dispersed onto a plasma-cleaned Si substrate and dried. The sample was immersed in a mercaptohexadecanoic acid (MHA) solution for 1 h, removed from it and washed with ethanol. This functionalizes all the exposed five faces with MHA. This was immersed in octadecanethiol (ODT) and the

sample was sonicated in order to detach the nanocubes from the substrate and the sixth face gets functionalized with ODT giving five hydrophilic and one hydrophobic faces. Another set of substrates containing the aqueous suspension of nanocubes is printed with a PDMS stamp inked with ODT in ethanol and then thoroughly washed with ethanol. Here the top face of the Ag nanocube gets functionalized. This was immersed in MHA solution and the four exposed faces get functionalized with MHA. This was then immersed in ODT solution and sonicated upon which the nanocubes from the substrate and the sixth face get functionalized with ODT giving four hydrophilic and two hydrophobic faces. Unfunctionalized cubes did not show any kind of assembly. When only one face of the nanotube was functionalized with hydrophobic ODT, the nanocubes tend to form dimers, joined at the hydrophobic faces in order to try and move this face away from water. Nanocubes with two opposing faces functionalized with ODT formed linear chains. Cubes having four ODT functionalized faces are assembled in a sheet-like manner. Ag nanocubes with four hydrophobic faces and one hydrophobic face were mixed at 1:4 ratio and star-shaped structures were obtained. When all the six faces were functionalized, they formed 3D superlattices. A schematic depicting the self-assembly of Ag nanocubes, completely functionalized with a hydrophobic SAM, at the air-water interface is given in Fig. 36F (292).

5.3 Assembly of anisotropic nanostructures of CdS/CdSe

After gold and silver, Cd-based materials are the most studied nanostructures owing to their properties. These materials are interesting because it is possible to design unique electronic structure inside the nanocrystals and make them interesting candidates for use in nanoelectronic devices. The assembly of these materials is well studied. A few interesting examples are given here. The liquid crystalline arrangement of rod-like CdSe NRs with orientational order and positional disorder was reported by Li et al. (293). Macroscopic alignment of CdSe NRs was reported in 2003 by Li and Alivisatos (294). They reported alignment into a nematic liquid-crystalline phase, and to some extent superlattice structures were formed when these are deposited on a substrate. The formation of a superlattice was found to be determined by the liquid-crystalline phase that formed prior to complete evaporation of the solvent (294). Talapin et al. in 2004 reported the self-assembly of CdSe NRs into nematic, smectic, and crystalline solids (295). The versatility of the method was demonstrated by using CdSe NRs of varying diameters and lengths as well as utilizing highly luminescent CdSe/CdS NR heterostructures for the assembly. Layered colloidal crystals obtained by the assembly exhibited anisotropic optical properties with characteristic birefringence, which was assigned to spe-

cific spherulite-like texture of each NR assembly. The crystals were grown by the slow destabilization of a nanocrystal solution upon allowing the diffusion of a non-solvent into the colloidal solution of nanocrystals. This can be considered as the first report to induce the organization of NR building blocks into highly luminescent 3D superlattices (295).

Perpendicular arrays of semiconductor NRs have potential applications in photovoltaic, field emission, and data storage devices. Several attempts were done to organize CdS/CdSe NRs in a perpendicular fashion. Gupta et al. reported 'self-corralling' NRs under an applied electric field where ligand-functionalized CdSe NRs in a polymer matrix phase separate under an applied electric field (296). They showed that the combined forces of an applied external field and interfacial energy can control the orientation of NRs and can form dense packing of CdSe NRs. Because of the permanent dipole moment of CdSe NRs and due to the inherent dielectric properties, these NRs in solution will drive the alignment along their long axis, parallel to the field lines of the external field. They got densely packed hexagonal arrays of NRs aligned along the direction of the applied field. The 'corralling' of the NR was driven in order to minimize the interfacial energy between the array of NRs and the surrounding polymers (296).

A similar method was adopted by Ryan et al. to align CdS NRs into superlattices (297). They found that the combination of a DC electric field and slow evaporation of solvent like toluene can be used to generate superlattices of II-VI semiconductor NRs (CdS) with perpendicular orientation (297). A non-electric field induced self-assembly of CdS NRs into perpendicular monolayers was reported by Ahmed and Ryan (298). They used highly oriented pyrolytic graphite (HOPG) as a template to produce the perpendicular assembly. On a variety of substrates, hexagonal oriented domains of the size range of 2 μm^2 were created by this method (298). Millimeter long smectic assembly composed of CdSe NRs was achieved rapidly under non-equilibrium conditions utilizing the capillary flow in a drying droplet (of a pinned droplet) was reported by Querner et al. (299). This method is important since this did not need any particular synthesis or solvent, pre-treatment of the substrate or NRs, or external fields. Many NR tracks are obtained in the flow due to the strong NR–NR interactions where NRs are assembled in a side-by-side manner and to the edge of the droplet forming a coffee ring. When the NR arrays reach droplet perimeter, the capillary pressure that is directed radially outward from the droplet drive the NR tracks to stack side-by-side concentrically.

Recently, Kang et al. (300) reported a strategy to make micrometer long 2D self-bundled CdS NRs without the aid of an external directing process. CdS NRs tri-n-octylphosphine (TOP) and tetradecylphosphonic acid (TDPA) capping having the optimum ratio were prepared. The as-prepared CdS NRs started to pack together when the concentration was higher than 2.0 wt% in toluene. As the solvent evaporates, the concentration of the solid increases. This results in the decrease of the interfacial energy of the NRs by interlacing the alkyl chains of surfactants. The first portion of NRs, standing normal to the substrate, serves as a nucleation site. Hence the other incoming NRs tend to assemble in the same direction with the assistance of the hydrocarbon chains on surfactants. Therefore, the self-assembly have leaning bundles at the outer edges and hexagonal packing perpendicular to the substrate inside (300).

Carbone et al. recently developed a seeded-growth approach for the synthesis of CdS NRs in which CdSe nanoparticles were used as seeds to produce asymmetric core-shell CdSe/CdS NRs (301). This on solvent evaporation at the toluene/water interface or under the applied electric field produced large area perpendicularly aligned NR arrays. A theoretical study to understand the force that operates in the assembly of NRs and binds them together was done by Ghezelbash et al. (302). They calculated the dipole–dipole attractive force and van der Waals attraction for the self-alignment CdS NRs and found that side-by-side alignment was more favorable than the end-to-end mode of alignment. But the experimental studies by the same group showed that end-to-end stripes are getting formed instead of side-by-side assembly. So they concluded that formation of stripes was kinetically controlled and mediated by solvent evaporation (302). Self-assembly of CdSe NRs at the oil-toluene-water interface using drying droplet was reported by He et al. (303). The interfacial tension, in-plane compression, and the decrease in surface due to the solvent evaporation was concluded to be the operating forces of the assembly. A method to synthesis cylindrical crystalline CdSe/CdS NRs supercrystals (SCs) that exhibit linearly polarized photoluminescence along their axial direction were reported recently by Zhuang et al. (304). They found that the anisotropic interparticle interactions between NRs as well as solvophobic interactions between an SC and the surrounding solvent play major roles in controlling the shape of the SCs. Supercrystals adopt the single- or multi-layered structures depending upon their volume (304).

The incorporation of different materials such as metals and semiconductors to form composite nanostructures is an interesting area of research because it increases functionality many folds. Synergetic properties can arise from the individual properties of constituent NRs or from the combination of the properties of these components. One such material is hybrid metal-tipped semiconductor NRs termed nanodumbbells (NDBs). Many examples exist and Au tipped CdSe NRs is one of them.

Assembling them into well-ordered structures is interesting because they may give several new properties. The use of gold tips as anchoring points for the self-assembly using simple dithiol molecules that preferentially binds onto the gold tips resulting in NR chains was reported by Salant et al. (305). The same group using a similar approach created dimers and trimer chains of NDBs. A biochemical linking strategy was followed in this study. The strong and specific avidin-biotin interaction was utilized to construct head-to-tail assemblies of NDBs. Using disulfide modified biotin, where the disulfide end conjugates to the gold tip, biotin was available for further conjugation with avidin. Avidin can conjugate up to four biotins that results in a flower-like assembly of the NDBs.

A solution-based side-by-side self-assembly of Au-tipped CdSe NRs into large 2D superlattices over a micrometer area was reported by Zhao et al. (306). In the hybrid NR, the CdSe segment was coated with a mixture of octadecylphosphonic acid (ODPA) and hexylphosphonic acid (HPA) termed as side ligands (SLs). The Au tips were stabilized with dodecylamine and didodecyldimethylammonium bromide (DDAB) termed as tip ligands (TLs). The presence of alkyl chains in SLs and TLs make these structures easily soluble in non-polar solvents and insoluble in polar solvents. The TLs were selectively replaced with 11-mercaptoundecanoic acid (MUA) to render difference in solubilities. The MUA was added in a polar solvent and was used for ligand exchange and self-assembly was made in a mixed solvent (dimethylformamide-toluene). In order to minimize the exposure of non-polar SLs with the polar solvents, NRs underwent side-by-side assembly. The MUAs present on the tip stabilized the assembled superstructure by intermolecular hydrogen bonding through carboxylic groups of MUA attached to neighboring NRs (306).

5.4 Assembly of anisotropic structures of other materials

The scope of this review does not allow the complete description of the assembly of all anisotropic structures reported. A few examples pointing toward the diversity of materials and their assembly is given in this section. Pt nanocrystals are important because of their catalytic activity. The self-assembled structures are believed to be ideal catalysts for reducing pollutant gases from the exhausts of automobiles, producing hydrogen from methane, in direct methanol fuel cells, and so on. The 2D self-assembly or 3D structured superlattices of these materials provide opportunity of fabricating nanodevices and creating templates for the assembly of other structures. The self-assembly of Pt nanoparticles of various shapes was studied by Petroski et al. in 2001 (307). They reported that the addition of dodecanethiol to acrylic acid capped Pt nanoparticle samples containing various shapes and sizes leads to self-assembly. The assembled

structures followed an *hcp* structure. Nanocubes are the most studied system in case of Pt. Ren and Tilley in 2007 reported a strategy to synthesize mondisperse Pt nanocubes, which due to its high degree of mondispersity can be readily arranged into 2D long range arrays (308). The shape-controlled platinum nanocubes and their assembly into 2D and 3D superlattices were reported by Demortière et al. (309). Assembly of bimetallic Pt-based cubes has also been reported. Oriented assembly of FePt cubes was reported by Chen et al. (310). They prepared FePt nanocrystal superlattice arrays with controlled texture and magnetic alignment. Palladium nanostructures are important since they show high hydrogen solubility and can act as an effective catalyst for Stille, Heck, and Suzuki reactions. Niu et al. recently reported a versatile seed-mediated method for the preparation of Pd nanocubes with a high degree of monodispersity (311). Because of the monodispersity, they tend to self-assemble into *ccp* arrays on the scanning electron microscopy (SEM) plate (311). The monodispersed synthesis and self-assembly of Pd nanobricks was reported by Umar and Oyama (312). Assembling icosahedral Pd nanoparticles into superlattice structures were reported by Zhang et al. recently (313). Recently, formation of long chains of Au/Ni and Au/Co MFs by a magnetic field induced self-assembly process was reported by Sajanlal and Pradeep (314).

Cu_2S, commonly known as chalcocite, is a p-type semiconductor with a bulk band gap of 1.2 eV. It has been widely used in solar cells, cold cathodes, nanoscale switches, and so on. The anisotropic hexagonal crystal structure of Cu_2S can be utilized to adjust the growth rate along (001) and (100) directions to obtain shape controlled nanocrystals. A solventless synthesis for the preparation of Cu_2S crystals of shape ranging from circular to hexagonal plates was reported first by Larsen et al. (315). They found that these sterically stabilized colloidal copper sulfide nanodisks spontaneously assemble with face-to-face close packing when the solvent is evaporated from concentrated dispersions to form a columnar assembly. The long range orientational order was confirmed by SAXS and grazing-incidence small-angle X-ray scattering (GISAXS). Time-resolved SAXS showed phase transition from the isotropic-to-columnar phase upon solvent evaporation and GISAXS proved that the columns orient perpendicular to the substrate. They also found that hexagonal close-packed ordering of the columns is relatively extensive, but within the column the disks were not periodic (315, 316). Zhuang et al. reported a water-oil interface confined method to synthesize monodisperse Cu_2S nanocrystals and their multilayer superlattice assemblies (317). The phase-selective synthesis of monodisperse CuS and $Cu_{1.75}S$ nanodisks with controlled sizes and shapes by high-temperature chemical reaction of $CuCl_2$ and S in oleylamine and their

self-assembly into monolayer or multi-layer ribbon-like nanostructures by face-to-face stacking was reported by Zhang et al. (318). Through simple solution-phase thermolysis of the copper dodecanethiolate polymer precursor, Cu_2S nanocrystals and superlattices were synthesized by Du et al. (318). Cu_2S nanodisks, spheres, and hexagonal nanoplates were assembled into super-structures through this method. They believed that the assembled structures are closely related to the lamellar structure of the copper thiolate precursor (319).

ZnO, an n-type semiconductor with a wide band gap energy of 3.3 eV and high exciton binding energy of 59 meV is an important material that can act as a component in ultraviolet light emitting diodes and as an electron-transporting layer in organic and dye sensitized solar cells and sensors. Liu et al. reported a process to fabricate films of hexagonal ZnO NR arrays on Si surfaces modified with HF etching and SAMs (320). An aqueous solution based wet chemical method has been reported for synthesizing ZnO NR arrays with control-lable diameter and lengths on different substrates by Chen and Gao (321). Through thermal decomposition of zinc acetate, a thin film of ZnO nanocrystals was coated on the substrate. This was used as a seed layer for the subsequent growth of NRs in aqueous solutions at low temperature. Highly ordered NR films spread over a large area were fabricated using this method (321). Hexagon-ally patterned, vertically aligned ZnO NR arrays using nanosphere lithography technique was reported by Liu et al. (322). A polystyrene microsphere SAM was first prepared and hexagonal patterns of gold particles were prepared on it through wet-etching method. This acts as a catalyst for the NR growth. Through catalyst-initiated epitaxy, ZnO NRs were grown on each of these catalyst sites, preserving the original hexagonal pattern (322). Lee et al. reported a seed-layer based solution chemistry route to make tunable arrays of ZnO needles and NRs (322). They studied the effect of pH and 1,3-diaminopropane additive concentration on the morphology of ZnO NR and nanoneedle arrays (323). Izaki et al. reported a room temperature electrochemical method for the electrophor-esis deposition of anionic polystyrene spheres on a conductive glass substrate followed by the electrodeposi-tion of ZnO in aqueous solutions to fabricate arrays of nano-cauliflower shaped ZnO nanoparticles (324).

ZnS is one of the most important II-VI semiconduc-tors. Pradhan and Efrima reported a method to synthesis highly uniform ZnS NRs and NWs of extremely small widths and assemble supercrystals of uniform NRs and ordered assemblies of NWs (325). Through a synchro-nous end-to-end attachment process of NRs, NWs were made. They found that after synthesis, NRs and wires spontaneously self-assemble into highly ordered crystal-line phases. Using capping agents of varying alkyl chain lengths, the interparticle spacing in these supercrystals

can be tuned. The assembly can be obtained in various substrates through various techniques. The NWs were assembled into large-scale parallel superstructures and crossed-wire, grid-like two-layer arrays (325). A phase-controlled synthesis of ZnS nanocrystals and the ordered assembly NRs and nanodots (NDs) was reported by Li et al. (326). The mechanism and the strategies of assembling 1D ZnS NRs on a 2D scale were also discussed in this report. Upon deposition of a drop of dilute solution of NRs on substrate, the solvent evapora-tion makes the concentration to increase with time. The free volume available to each rod also decreases as the solvent gets evaporated. This makes the rods to aggregate or align side-by-side under the influence of directional capillary force and van der Waals attraction. This results in the increase in the viscosity and finally freezes the local liquid-like structure to form a lyotropic crystalline phase. The concentration of the NRs in solution, the nature of the capping molecules, and the evaporation rate of the solvent are three main factors that can affect the quality as well as the range of the assembly (326).

Trigonal-tellurium, a p-type semiconductor, has a very narrow band gap and has attracted a great deal of interest because of its good photoconductivity, photoelectricity, thermoelectricity, catalysis, non-linear optical properties, and high piezoelectricity. Self-assembly of Te NRs to Te microrods was reported by Batabyal et al. (327). Te NRs were prepared by reducing bulk Te powder using an aqueous solution of sodium dithionite and then oxidizing the solution in air to get Te NRs. Centimeter long rods were made by controlling the airflow, upon which these NRs self-assemble to give the microstructure (327). The self-organization of Te NRs to V-shaped assemblies was reported by Tang et al. (328). They found that in a suspension of Te NRs, short NRs of length 50 nm tend to form V-shaped or checkmark-like assemblies while long NRs of length 2,200 nm remained as such. Using Brownian dynamics simulations, they modeled this ob-servation and explained the experimental observations (328, 329). Alignment of Te NRs on a solid substrate via the magnetization-alignment-demagnetization process was reported by Yuan et al. (330). Te NRs covered with a shell of poly(tert-butyl methacrylate) was prepared and they were made magnetic by the treatment with magnetite nanoparticles that assembles on the surface of the rods through a hydrophobic interaction in THF to form magnetic nanocylinders. This upon interaction with magnetic field aligns in the direction of the magnetic field. On acid etching, the magnetic nanoparticles are etched away leaving the assembled nanostructures behind (330).

Titanium dioxide is a useful material, having numerous potential applications in diverse areas such as photo-catalysis, solar cells, and electroluminescent hybrid de-vices. Assembly of anisotropic TiO_2 based systems has
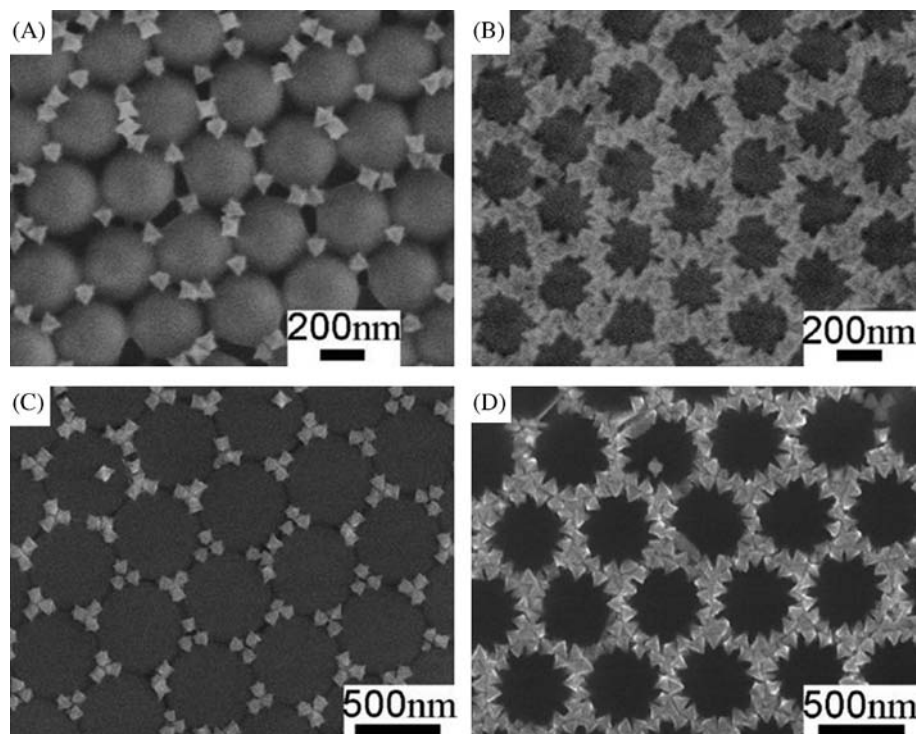
Fig. 37. SEM images of patterned arrays of PbS nanostars assembled on the 340 nm (A, B) and 500 nm (C, D) MCC templates with varying packing densities. Reproduced with permission from Reference (333). American Chemical Society, Copyright (2010).

been well studied. Self-assembled end-to-end structure of oligomeric TiO_2 NRs using the biotin-avidin interaction was reported by Dimitrijevic et al. (331). One of the recent studies was on the 2D self-assembly of TiO_2 nanoleaves via supramolecular interactions. It was found that the assembly happens in a facet-selective manner. The single-crystalline TiO_2 nanoleaves were functionalized with catechol-group-terminated Zn(II)-porphyrin that was coordinated with EB. Trans-2,2′-ethylene 4, 4′-bipyridyl (EB) cross-links the adjacent TiO_2 nanoleaves along the (101) face, resulting in a face-selective, self-assembled, 2D stacking structure in a 'side-by-side' fashion (332).

Self-assembly of star-shaped PbS nanocrystals into close-packed arrays and patterned arrays was demonstrated by Huang et al. recently (333). Through drop-coating or vertical deposition method 3D or 2D *hcp* arrays of PbS nanostars were fabricated on clean Si substrate (Fig. 37). Through vertical deposition method and monolayer colloidal crystals (MCC) and inverted MCC as the template, various non-close-packed (ncp) controllable patterns were also made. The ncp arrays of (111)-oriented PbS nanostars leading to the formation of novel star-sphere binary colloidal crystals where three horns stands on the template was prepared. Using IMCC template, (001)-oriented PbS nanostars were arranged into an ncp array with a single horn stretched vertically upward. Using MCC/IMCC templates with larger peri-

odic spacings, several novel ncp arrays were fabricated and found that in template-assisted assembly, the long-range hexagonal order from the initial MCC template is inherited in the obtained PbS ncp arrays.

Barium chromate ($BaCrO_4$) nanoparticles were assembled into different structures by Li et al. (334). They demonstrated that $BaCrO_4$ can be organized into complex structures through the interfacial activity of reverse micelles and microemulsions. The interdigitation of surfactant molecules attached to specific nanoparticle crystal faces the driving force for the assembly. They produced linear chains, rectangular superlattices, and long filaments of $BaCrO_4$ nanocrystals as a function of reactant molar ratio, which influences the fusing of reverse micelles and microemulsion droplets (334). Two-dimensional NR monolayer assembly of $BaCrO_4$ using LB technique was reported by Kim et al. (335). Pressure-induced isotropic-nematic-smectic phase transitions and transformation from monolayer to multi-layer NR assembly were also discussed in this work (335). Rare-earth nanocrystals have drawn great interest owing to their unique physical and chemical properties and potential applications in the fields of luminescence devices, biochemical probes, and medical diagnostics. Evaporation-induced self-assembly of rare-earth oxide nanopolyhedra, nanoplates, and nanodisks was reported by Si et al. (336). Self-assembly of LaF_3 triangular nanoplates was also reported by the same group (337).

They also reported the self-assembly of sodium rare-earth fluoride nanocrystals of various shapes (338). All these assemblies were of short range order. the LB mediated controllable assembly of diverse rare-earth nanocrystals was reported by the same group recently (339). Using this technique, large-area films of various nanoparticles like NaYF$_4$, Yb, Er spherical nanoparticles, LiYF$_4$ nanopolyhedra, triagonal-shaped LaF$_3$, square shaped CaF$_2$, and hexagonal EuF$_3$ nanoparticles were assembled (339). The LB assembly of vanadium dioxide (VO$_2$) NWs functionalized with stearic acid and CTAB was reported by Mai et al. (340). Zheng et al. reported the self-assembly and self-orientation of truncated octahedral magnetite nanocrystals (341). External magnetic field induced self-assembly of octahedral magnetite nanocrystals was recently reported by Qi et al. (342). The self-assembly of lead zirconate titanate cubes into single crystal like microcrystals was reported by Liu et al. (343). A method to prepare transparent WO$_3$ NR film through the assembled coating of WO$_3$ NR suspension onto ITO coated glass was reported by Wang et al. (344). The assembly was dependent on the drying rate of the film, the concentration of suspension, and the aspect ratio of NRs but independent of the surface properties of substrates. The assembly occurred through an aggregation-deposition process (344). The β-ferric oxyhydroxide (β-FeOOH) is an interesting iron-based material that shows a tunnel-type structure in which the iron atoms are strongly bonded to the framework forming the tunnels and is reported to be a promising candidate for an active iron-based material for lithium batteries. Zocher (345), Zocher and Heller (346), and Watson et al. (347) reported the formation of 'Schiller layers' in the stable sol sediments containing ordered structures and found that they exhibit brilliant interference colors from β-FeOOH. The assembly of this system has been very well studied. The atomic force microscopic investigation of smectic, or multi-layer, structures in dry sol sediments of β-FeOOH was reported by Maeda and Maeda (348). They found that the smectic structure locally has an in-layer square morphology (348). A longer-ranged bond-orientational order will exist even after the defects destroy the 2D crystallinity. The co-existence of several smectic domains, each of which has a distinct orientation, and mono- and several-folded layers confined in the sols was also observed (348).

6. Applications of anisotropic nanomaterials

Due to the size and shape dependent physical and chemical properties, anisotropic nanomaterials have been used for various applications. A few of the important applications of different kinds of nanostructures are mentioned below. This section does not cover a comprehensive review of the literature. However, we have

mentioned specific reviews or references in the appropriate sections to guide an interested reader.

6.1 Bioconjugation and labeling

Nanoparticles can be easily functionalized with biological molecules for targeting cancer cells. Gold nanorods have been stabilized, conjugated to antibodies, and characterized for biological applications by Liao and Hafner (349). They replaced the stabilizing surfactant bilayer that surrounds gold nanorods by thiol terminated methoxypoly(ethylene glycol). Gold nanorod bioconjugation was accomplished with a heterobifunctional cross-linker, with antibody activity confirmed by a strip plate assay. Pissuwan et al. (350) used antibody functionalized nanorods to conjugate them to murine macrophage cells in their photothermal studies. Takahashi et al. reported the bioconjugation of gold nanorods with phosphatidylcholine for the controlled release of plasmid DNA by NIR radiation (351). Gold nanocage can also be functionalized with biological molecules such as antibodies, nucleic acids, and small-molecule inhibitors can be used to target cancer cells for early-stage diagnostics and thermal therapy of tumors (352). Schematic illustration of the protocol used by Chen et al. to conjugate antibodies to the surface of Au nanocages is shown in Fig. 38A. A breast cancer cell line, SK-BR-3, which overexpresses epidermal growth factor receptor 2 (EGFR2 or HER2), has been used to test the molecular specific binding of bioconjugated gold nanocages (353). In a typical process, primary antibodies (monoclonal anti-HER2 antibody from mouse) were immobilized on the cancer cells by incubating the SK-BR-3 cells in anti-HER2 antibodies. Gold nanocages were conjugated with a secondary antibody such as anti-mouse immunoglobulin G or IgG, following the conventional (Fig. 38) protocol. Finally, a buffer solution containing IgG-conjugated gold nanocages was applied to SK-BR-3 cells bound with anti-HER2 antibodies. After that, a fluorescence image was taken. The cells revealed a uniform green color indicating a homogeneous distribution of the primary anti-HER2 antibody on the cell surface (Fig. 38B).

6.2 Optical contrast agent

The strong SPR, biocompatibility, easiness in bioconjugation, and large scattering cross-section make anisotropic nanoparticles an attractive contrast agent for NIR imaging applications (7, 92). Au nanocage is an attractive contrast agents because of their strong, tunable SPR peaks in the near-infrared and comparatively smaller size (353). The utility of gold nanocages as an optical contrasting agent has been demonstrated by performing an optical coherence tomography (OCT) imaging on phantom samples with and without nanocages. The OCT imaging (Fig. 21C) was conducted using a 7-fs Ti:sap-
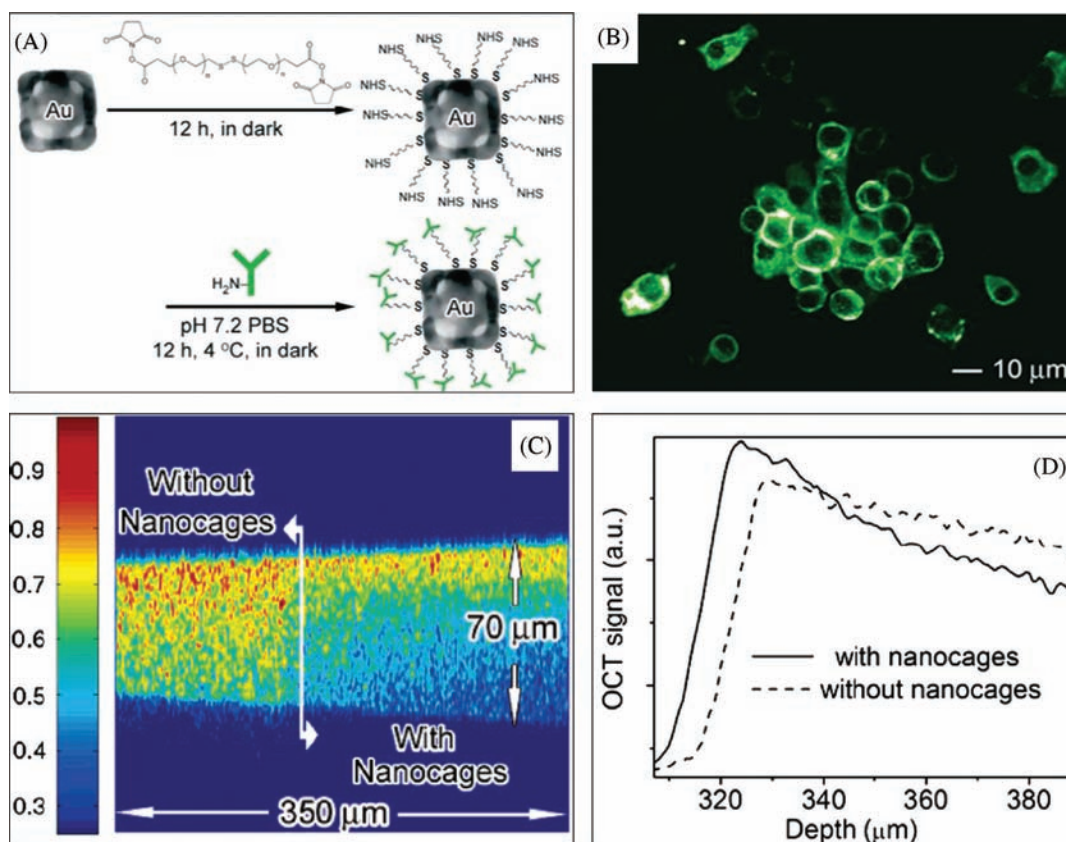
Fig. 38. (A) Schematic illustration of the protocol used to conjugate antibodies to the surface of Au nanocages. (B) A fluorescence image of SK-BR-3 cells whose surfaces were treated with the anti-HER2 antibodies, followed by incubation with fluorescence-labeled IgG. (C) OCT image of a gelatin phantom embedded with TiO$_2$, and the concentration of TiO$_2$ was controlled at 1 mg/mL to mimic the background scattering of soft tissues. (D) Plots of the OCT signals on a log scale as a function of depth. Reproduced with permission from Reference (353). American Chemical Society, Copyright (2005).

phire laser with a center wavelength at 825 nm and a bandwidth of 155 nm. Preliminary studies show significantly improved spectroscopic image contrast for tissue phantoms containing Au nanocages. Gold nanocages showed an absorption cross-section of 2.90×10^{-20} m^2 at 800 nm, about five orders of magnitude stronger than conventional dye indocyanine green. The results suggest that gold nanocages can be used as good absorption contrast agents for OCT imaging. The log of the OCT signal as a function of depth is plotted in Fig. 38D.

6.3 Photothermal therapy

Living cells are highly sensitive to the temperature and rises of a few degrees can lead to cell death. The NIR absorption and related photothermal effect is another important feature of plasmonic nanoparticles (87). Compared to the other non-metallic photothermal absorbers, the anisotropic nanoparticles enable dual imaging/therapy functions. It has been demonstrated the NIR absorbing capacity of several anisotropic nanomaterials such as nanorods, nanocages, nanoshells, and nanostars can be used for the photothermal therapy (349–360). In biological systems, the Au nanocages are

capable of producing a local temperature rise that can provide a therapeutic effect on cancer cells that are selectively targeted by bioconjugated Au nanocages (349–358). Due to the large absorption cross-sections of Au nanocages, the absorbed photons are converted into phonons and can increase the temperature of the system. It is shown that extremely high lattice temperatures can be attained by Ag nanocages by the ultrafast laser-induced heating process (358). Such therapy is less invasive than chemotherapy or surgery and holds strong promise as a new form of cancer treatment. The photothermal destruction of breast cancer cells *in vitro* by using immuno-targeted Au nanocages has been demonstrated by Skrabalak et al. (355). Gold nanocages with an average edge length of 65±7 nm (absorption peak at 800 nm) were conjugated with anti-HER2, a monoclonal antibody, to target breast cancer cells (SK-BR-3) through the epidermal growth factor receptor (356–358). Then the targeted cells were irradiated with a pulsed near-infrared laser. By varying the power density, the duration of laser exposure, and the time of response after irradiation, it is possible to optimize the treatment conditions to achieve effective destruction of the cancer
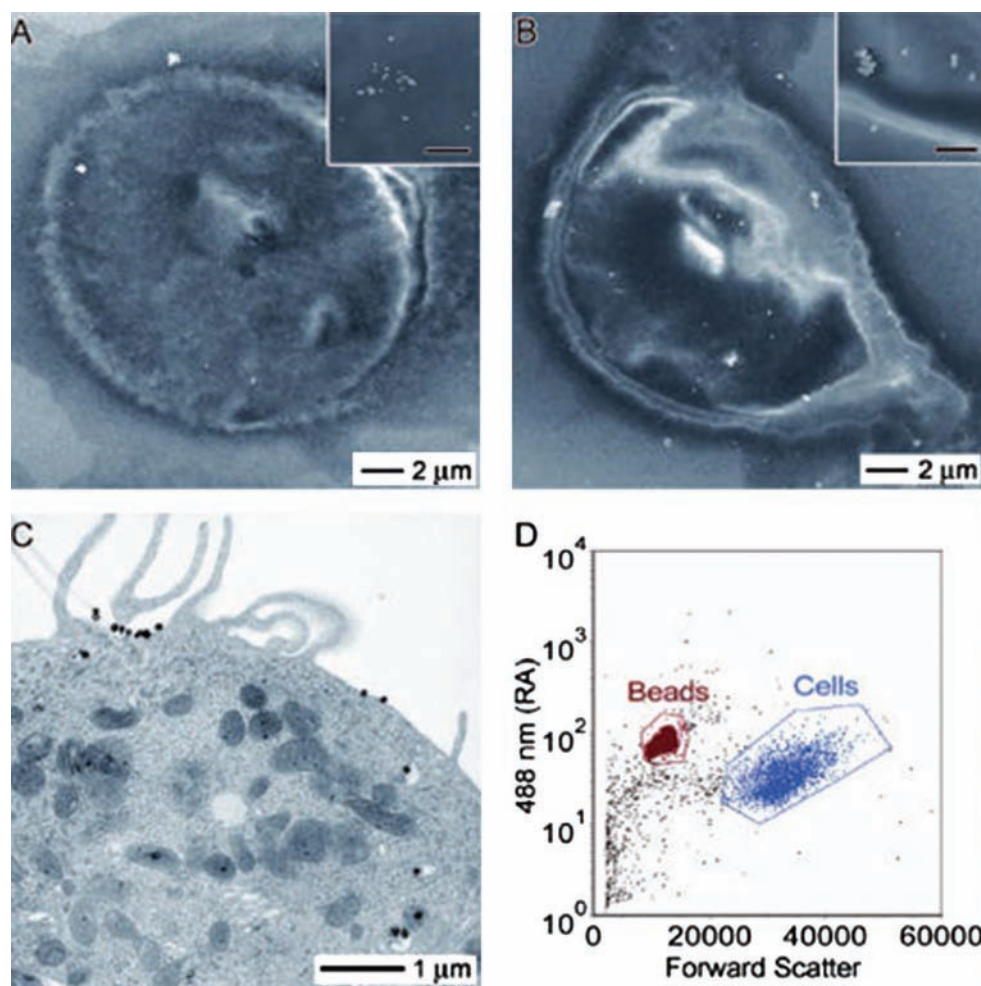
Fig. 39. SEM images of SK-BR-3 cells targeted with immuno Au nanospheres (A) and nanocages (B). SEM images at higher magnification (insets) reveal that the bright spots in the SEM images are indeed nanospheres and nanocages, respectively. The scale bar in the insets represents 500 nm. (C) TEM image of a microtomed SK-BR-3 cell conjugated with immuno Au nanocages. (D) Typical flow cytometry graph indicating how the forward scatter (x-axis) and right angle scatter (y-axis) can be used to differentiate the size difference between beads and cells. Reproduced with permission from Reference (356). American Chemical Society, Copyright (2008).

cells. It was found that cells targeted with the immuno-Au nanocages responded immediately to laser irradiation and cellular damage was happening irreversibly at power densities greater than 1.6 W/cm^2 (Fig. 39). The percentage of dead cells increased with increasing exposure time.

Using multi-segmented metal nanorods, Salem et al. have demonstrated a new non-viral gene therapy approach (85, 86). Nanotriangle is another candidate that can be used for cancer cell treatment. The large near-infrared absorption of the nanoparticle has potential applications in hyperthermic treatment of cancer cells. The flat nature of the nanotriangle would facilitate thermal contact between the nanoparticle and cancer cells; thereby letting us reduce the exposure times. Nanotriangles can also be used to target specific delivery

to the cancer cells, resulting in low dosage requirement and thus reducing the metal toxicity.

6.4 Cancer cell imaging

The strong SPR of metal nanoparticles enable one to image individual particle location with various optical microscopic techniques such as dark-field optical microscopy and TPL microscopy. Gold nanoparticles are well suited for biomedical imaging, since the scattering cross-section of gold nanoparticles is much stronger than that of conventional fluorescent dye molecules (88). The GNRs are ideal candidates for cancer cell imaging due to strong absorption and scattering in the near infrared region (650–900 nm) (84–92, 361). Huang et al. (361) have synthesized gold NRs (aspect ratio of 3.9) and were centrifuged in order to remove other ions and excess
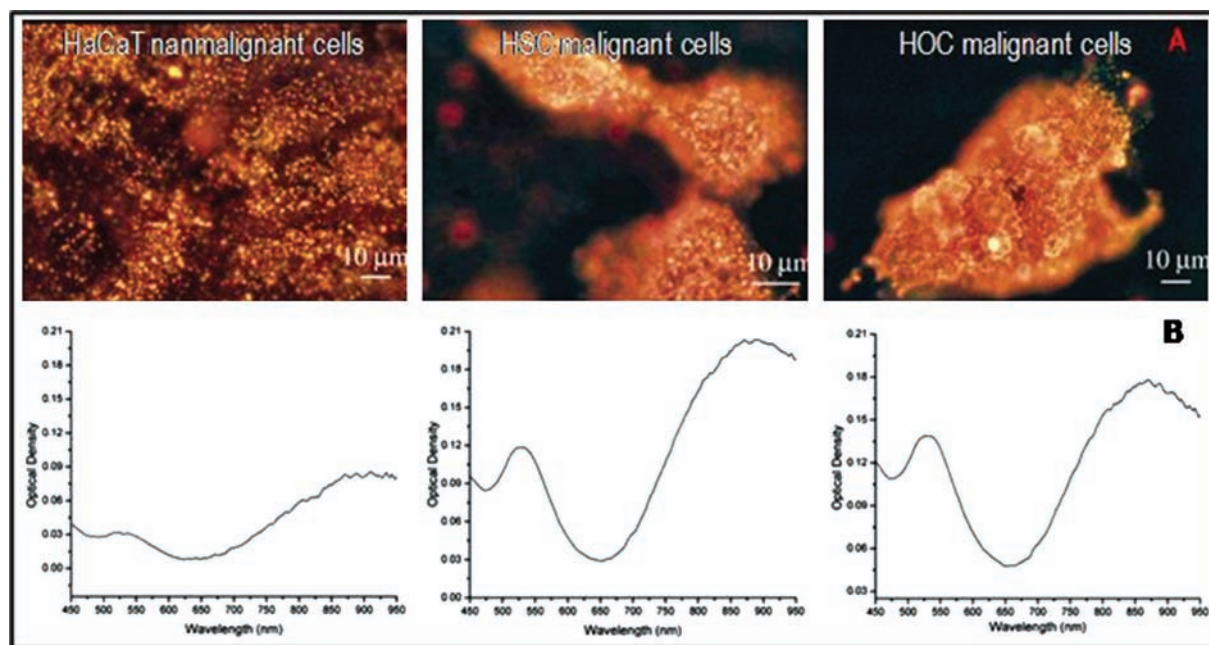
Fig. 40. (A) Light scattering images of anti-EGFR conjugated Au NRs after incubation with cells for 30 min at room temperature. (B) Average extinction spectra of anti-EGFR conjugated Au NRs from 20 different single cells for each kind. Reprinted with permission from Reference (361). American Chemical Society, Copyright (2006).

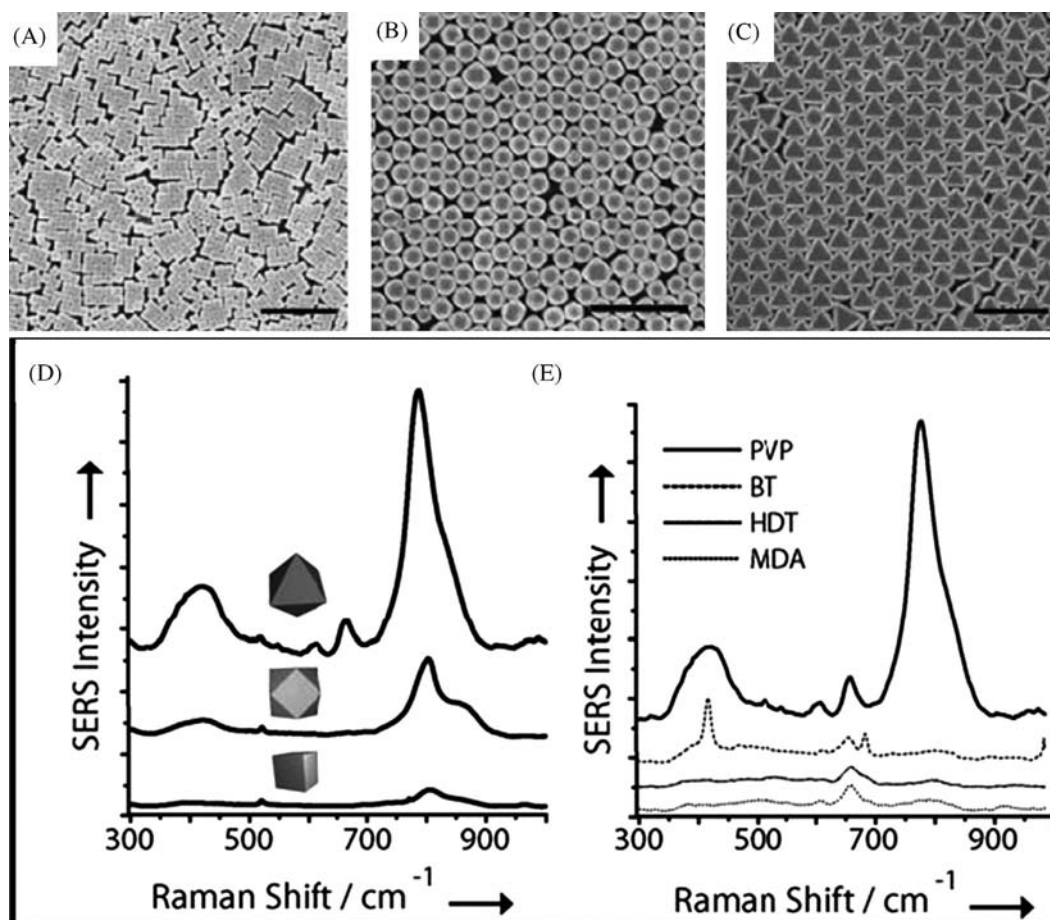cationic surfactant, CTAB. Subsequently, the NR surface was modified by negatively charged PSS and were mixed with an antibody solution in 4-(2-hydroxyethyl)-1-piperazineethanesulfonic acid (HEPES) buffer. The NRs conjugated to anti-epidermal growth factor receptor (anti-EGFR) monoclonal antibodies are incubated in the cell culture. Two malignant cells such as HOC 313 clone 8 and HSC 3 and one non-malignant HaCat cell were used in the experiment. The anti-EGFR antibody-conjugated NRs bind specifically to the surface of the malignant type cells, with a much higher affinity due to the over expressed EGFR on the cytoplasmic membrane of the malignant cells.

Fig. 40 shows the light scattering images of anti-EGFR conjugated GNRs after binding to malignant and non-malignant cells. The orange color of the GNR is the most dominant, which corresponds to the surface plasmonic enhancement of the longitudinal oscillation in the near-infrared region. Anti-EGFR conjugated GNRs have specific interaction to cancerous cell, HOC 313 clone 8 and HSC 3 and non-specific interaction to the non-cancerous cell, HaCat. The nature of interaction is distinguished through the light scattering imaging. Fig. 40 shows the quantity of NRs bound to the cell. From the extinction spectra, it is clear that the intensity of the cancerous cells is around double of the non-cancerous cells. It is due to the nature of interaction between anti-EGFR conjugated GNRs and cells: specific interaction to the malignant cells and non-specific interaction to non-malignant cells. Wang et al. demonstrated that a Au nanorod with a LSPR peak at 820 nm, when excited at

820 nm using a two-photon scheme, could produce photoluminescence signals 58 times that of the fluorescence signals from a rhodamine molecule (132). The use of Au nanorods as contrast agents for two-photon luminescence imaging of cancer cells has also been demonstrated by Durr et al. (133) and Black et al. (134). Gold nanocages are a new class of material that exhibits a broad two-photon photoluminescence band extending from 450 to 650 nm when it is excited by a Ti:sapphire laser at 800 nm. Recently, Au et al. have demonstrated that Au nanocages can be used as optical imaging agents for two-photon microscopy. In that work, they have demonstrated the use of two-photon microscopy as a convenient tool to directly examine the uptake of antibody-conjugated and PEGylated Au nanocages by U87MGwtEGFR cells (354).

6.5 Surface-enhanced Raman scattering substrate

Since, SERS is a well-established technique and an attractive analytical tool for trace level chemical detection due to its ultrahigh sensitivity and specificity, a number of fine reviews are available on this topic in the literature (104–117). The sensitivity of this technique strongly depends on the shape of the nanoparticles (106, 107). Using this technique, Mulvihill et al. demonstrated that LB assemblies of various polyhedral Ag nanocrystals (Fig. 41A–C), made by the polyol process, can detect arsenate and arsenite in aqueous solutions with a detection limit of 1 ppb (Fig. 41D), an order of magnitude below the standard set by the World Health Organization (WHO; 362–366). The high SERS response

of octahedra LB arrays coated with various organic species such as benzenethiol, hexadecanethiol, mercapto-decanoic acid is shown in Fig. 41E. The development of a reliable, portable, and simple-to-use device for detecting arsenic in groundwater is urgently needed in developing nations, where contaminated groundwater is at the root of a public health crisis. This SERS substrate is reliable, reproducible, highly portable, and could be easily implemented in field detection. Gold nanoflower (AuNF) is another SERS substrate nanoparticle that exhibit strong SERS activity. The AuNF particles could be developed into Raman-active tags by packaging RhB@AuNF particles with denatured bovine serum albumin (BSA) molecules. The application of these Raman-active tags in living cells was demonstrated by using the RAW264.7 macrophage cell line (367).

Real-time detection of biomolecules using SERS has also been reported (111, 112). Yang et al. (113) reported a higher SERS activity of triangular plates due to its sharper corners and edges. It is also demonstrated that silver nanoplates in its aggregated form detects molecule with larger enhancement than single Ag nanoplates, due to strong electromagnetic coupling between neighboring nanoplates (363, 364). The high SERS activity of the anisotropic metal nanoparticles can be understood in terms of their unusual LSPR properties and the sharp corners on the surface of a nanoparticle being able to create a greater localized electric field in comparison to spherical ones (365, 366).

6.6 Superhydrophobic surface

The wettability of a surface is an important feature governed by the chemical composition and the morphology of the surface of the materials. The surface hydrophobicity can be increased by creating a local geometry with a large geometric area relative to the projected area or by using roughness combined with hydrophobic coatings. Superhydrophobic surfaces exhibit very high water-repellent properties. Water droplets that are in contact with a superhydrophobic surfaces (contact angle
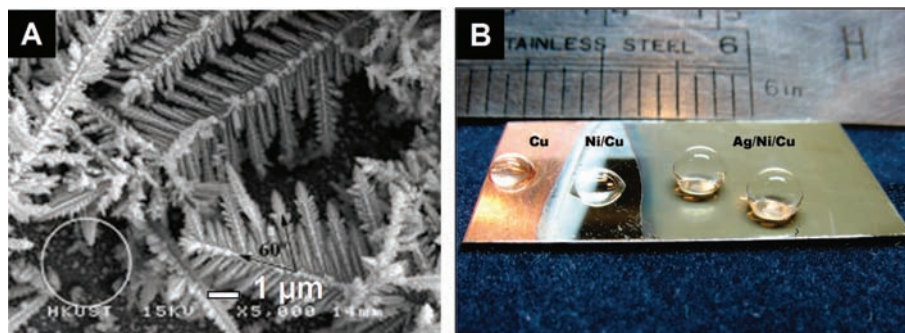
Fig. 42. (A) SEM image of Ag crystallites. (B) Photograph of water droplets on the Ag dendritic film surface, Ni surface, and Cu surface. All surfaces were modified with n-dodecanethiol. Reproduced with permission from Reference (227). American Chemical Society, Copyright (2008).

$>150°$) form nearly spherical beads. Inorganic or organic contaminants on such self-cleaning surfaces are picked up by water droplets or adhere to the droplet and will be removed from the surface when the water droplets roll off. Anisotropic nanomaterials can be used in this regard for making superhydrophobic surfaces. A dendritic film of single-crystalline Ag having a thickness of about 10 μm with a SAM of n-dodecanethiol yields a superhydrophobic surface with a contact angle of $154.5 \pm 1.0°$ and a tilt angle lower than $2°$ (227, 228). From the contact angle measurements, it was found that the presence of Ag crystallites on a particular substrate make substantial improvement in the hydrophobicity compared to the other substrates without Ag crystallites (Fig. 42). The GaAs substrates on which Ag nanoplates were grown through direct reaction between aqueous solutions of $AgNO_3$ and GaAs surfaces exhibit the 'Lotus' effect (228). In order to decrease the surface energy of Ag, the as-grown Ag nanoplates were coated with 1-hexadecanethiol molecules. The wettability of the resulting Ag nanoplate/GaAs composite surfaces could be easily tuned by controlling the dimensions and nanoscale surface roughness of individual nanoplates, by appropriate variation of reaction conditions.

6.7 Mercury sensor

Mercury is a known environmental pollutant released from various sources such as power plants, burning fossil fuels, and so on. It is important to monitor Hg levels in the aquatic ecosystem as human exposure to high Hg levels can harm the brain, heart, kidneys, lungs, and immune systems of people of all ages. Gold nanorods are capable for sensing mercury in tap water samples at the parts-per-trillion (ppt) level (368). Selectivity and sensitivity of mercury is due to the amalgamation of mercury and gold. The entire sensing process takes place in less than 10 minutes, with no sample separation. Ultralow levels of Hg have been detected. Fig. 43 shows the schematic representation and experimental evidence of the amalgamation of Hg with GNRs. The aspect ratio of GNRs decreases with increasing the concentration of Hg^{2+} at constant $NaBH_4$ concentration. The direct correlation between the wavelength shift and mercury concentration makes quantitative analysis (Fig. 43). In tap water, the detection limit was 6.6×10^{-13} g.L^{-1}.
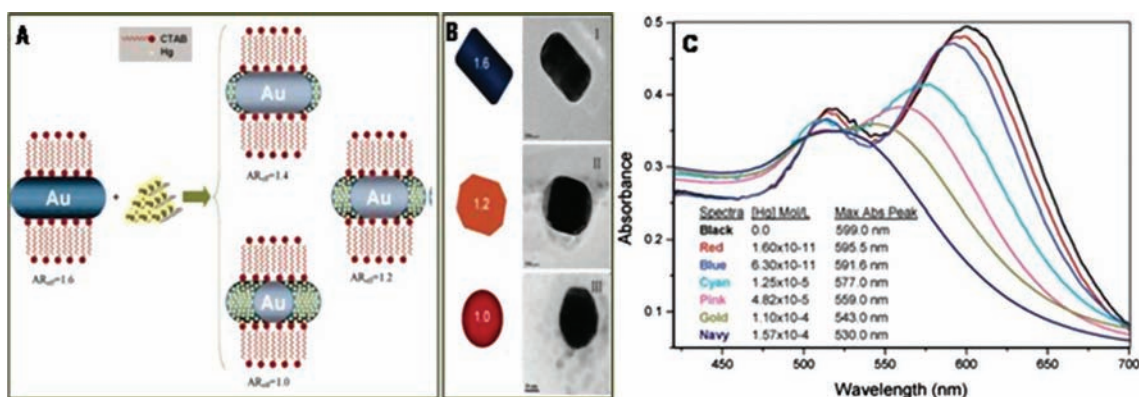
Fig. 43. (A) Schematic representation of the amalgamation of Hg with GNRs. (B) TEM images of GNRs in the absence and the presence of Hg. (I) no Hg, (II) 1.25×10^{-5} M, and (III) 1.57×10^{-4} M of Hg^{2+}. (C) UV-vis absorption shift in the concentration range between 1.6×10^{-11} and 6.3×10^{-11} M of Hg(II). Reproduced with permission from Reference (368). American Chemical Society, Copyright (2006).

6.8 Infrared absorbing material

It has been recognized that NIR absorbing films based on gold can be used as an alternative to reflective coatings for blocking IR radiation. Nanoparticle-based approaches are highly efficient and can be economically viable than other methods. The NIR-IR absorption exhibited by the certain nanomaterials has been used for the development of infrared filters. Using a proto-typical device, it was demonstrated that gold MFs can absorb a significant amount of heat thereby reducing the temperature rise in an enclosure exposed to daylight (169). The heat absorption measurements were done with a monolayer and a bilayer of MF-coated glass slides along with a blank glass substrate as the control. Compared with the blank glass substrate, the MF-coated glass gave an average temperature inside the cardboard box that was lower by 2°C, whereas the bilayer-coated substrate showed a reduction of 4.3°C. It is also suggested that the NIR-IR absorbing property of gold nanotriangle can be used as heat-absorbing optical coatings for windows (164, 169, 187).

6.9 Plasmonic waveguide

Nanomaterials are interesting in photonic device applications because, through careful fabrication, it is possible to guide electromagnetic energy with a lateral mode confinement below the diffraction limit of light, which is not possible through conventional waveguides or photonic crystals. It can be achieved along chains of closely spaced metal nanoparticles that convert the optical mode into non-radiating surface plasmons. These arrays can be prepared through electron beam lithography or self-assembly techniques. Maier et al. showed experimentally that through closely spaced silver NRs, electromagnetic energy can be transported from a localized sub-wavelength source to a localized detector over distances of about 0.5 μm (369). The individual rods in the waveguide structures consist of 90 nm long Ag NRs (30 nm × 30 nm width/thickness) and an interparticle spacing of 50 nm between adjacent particles. The long axes of the individual NRs were oriented perpendicular to the waveguide chain axis that allows an increased near-field coupling between the particles. Using the tip of a near-field scanning optical microscope, the waveguide was excited by laser light from a dye laser at a wavelength of 570 nm, corresponding to the single-particle resonance, and using fluorescent nanospheres (carboxyl-coated polystyrene nanospheres filled with fluorescent molecules), the energy transport through the waveguide was probed. The local excitation subsequently propagates along the nanoparticle structure and excites a fluorescent nanosphere placed on top of a waveguide at a distance from the excitation source. Energy transport through the waveguide results in dye emission from the fluorescent particle that proves the energy transfer. Energy attenuation lengths of several hundred nanometers propose the use of these plasmon waveguides as functional end-structures in integrated optical devices (370).

6.10 Biosensor

The SPR exhibited by anisotropic nanomaterials provides great opportunity to monitor the changes of the local environment and it can be used for sensing (371). Due to the high-value shape factor (surface curvature), GNRs are highly suited for plasmon sensing. Yu and Irudayaraj (372) have demonstrated a multi-plex biosensor assay using gold nanorods to different targets. Human, rabbit, and mouse IgG were conjugated to gold nanorods of different aspect ratios via a 11-mercaptoundecanoic acids linker, and the binding events of these probes to their respective complements (anti-IgGs) were monitored by the shifts in the SPR wavelength of the nanorods. They could also detect the multi-plex surface markers of breast cancer cells by using the antibody-conjugated gold nanorod molecular probes (373). Huang et al. recently reported a molecularly mediated assembling strategy to fabricate a layered superstructure of gold nano-octahedra (374). They used this assembled structure as the host matrix for a glucose sensor. Single-layered Au nano-octahedra/GOx (glucose oxidase) system and spherical particles/GOx system were compared to check the performance of the sensor. Au nano-octahedra system exhibited a greater voltammetric response compared to the spherical particle system under the same conditions showing the dependence of the sensor activity on the shape of the Au particles used. Au nano-octahedra-based glucose biosensor showed a high level of sensitivity in the range of 0.349 μA mM^{-1}. The system gave a fast response (within several seconds) and a wide response range (from 0.125 to 12 mM) also (374).

6.11 Photovoltaic device

Nanocrystals of inorganic semiconductors such as CdSe also act as good electron acceptors from conjugated polymers; however, the efficiency of photovoltaic devices made with spherical nanocrystals is limited by the problem of electron extraction through the nanocrystal network 5, 6. The use of nanorods instead of spherical nanocrystals has been shown to give significantly higher efficiencies because of the smaller number of interparticle hops necessary for electrons to leave the device 7, 8. Wei et al. fabricated an array of TiO$_2$ NR assemblies on a flat TiO$_2$ surface via a low temperature sol-gel reaction in a reverse micelle system (375). Conjugated with a semi-conducting polymer, these arrays were used for constructing photovoltaic devices. They found that these TiO$_2$ NR assemblies can function as an efficient exciton collector in polymer photovoltaic devices. This resulted in improved power conversion efficiency (PCE) with a relatively high fill factor. Since these structures are projected from the

flat TiO_2 substrate, they can provide direct pathways for electron transport making them ideal for photovoltaic applications. For a simulated solar light irradiation of 100 mW/cm^2, a short circuit current density (Isc) of 0.33 mA/cm^2, an open circuit voltage (Voc) of 0.87 V, and a fill factor (FF) of 0.49 were seen, resulting in a PCE of 0.14% for the device with flat TiO_2 alone. But for the device containing the nanoassembled structure, an increased performance was obtained. A PCE up to 0.39% and Isc of 0.95 mA/cm^2, Voc of 0.88 V, and FF of 0.47 was also obtained. External quantum efficiency (EQE) plots showed that EQE is maximum under 510 nm radiation and under a monochromatic light of 510 nm wavelength (0.2 mW/cm^2), the FF for the device reached as high as 0.64. Such a high FF of the device with the TiO_2 nanostructures was explained as due to the effective electron transport within the TiO_2 NRs, because of their single crystalline nature and good connection with the flat TiO_2 layer (375).

Ju et al. through a low temperature strategy inserted oriented ZnO nanopillars into organic photovoltaic devices based on a blend of poly(3-hexylthiophene) and fullerene (376). The dependence of ZnO morphology on the photovoltaic performance on was also studied. The stability of the device was also studied. The photovoltaic performance of devices with a ZnO layer was enhanced compared to that without a ZnO layer. The performance improved further when an oriented ZnO porous nanopillar structure was used. This photovoltaic cell demonstrated a high efficiency, a monochromatic EQE of over 50% at the peak wavelength, an Isc of 5.79 mA cm^{-2}, a Voc of 0.43 V, an FF of 49%, and a PCE of 1.22% under an illumination intensity of 100 mW/cm^2. They found that the oriented ZnO nanopillar array plays an important role in collecting photogenerated electrons and acts as a conducting path to the electrode (376).

7. Summary and future outlook

This review summarizes recent progress in the area of anisotropic nanomaterials. We have presented an overview of various chemical methods to synthesize anisotropic nanomaterials, various methods to assemble them to create structures, and indicated their important properties. Although a variety of materials are known, only a few of them have been explored for interesting properties. Tuning of the morphologies of nanomaterials by various synthetic approaches has been explored. We have also pointed out certain aspects on the growth mechanism of anisotropic nanomaterials. Giving consideration to the large implications of assembled nanostructures, assemblies of diverse anisotropic nanomaterials of various metals have been reviewed in detail. Description of various forces inducing the formation of assembled anisotropic superstructures is presented. Even though various factors responsible for the growth of

nanoparticles are known, an exact growth mechanism for their evolution is lacking in the literature. Anisotropic nanomaterials provide an interesting system for the study of growth mechanism of materials in the nanoregime and will also be useful for the investigation of the fundamental size- and shape-dependent properties of matter. In order to get an exact mechanism of nanoparticle growth, it is important to monitor various aspects such as different stages of nanoparticle growth, formation of fluctuating nuclei, defect formation in seeds, diffusion and deposition of metal ions onto the seed surfaces, surface–interface interactions of specific species in the medium, and so on. More precise kinetic theory is yet to develop, which can predict not only the evolution of a single nanoparticle, but also provide an insight into the influence of various parameters on the anisotropic growth of nanoparticles under a range of conditions. This will indeed give new insight into the possibility of making anisotropic nanoparticles of various possible elements in the periodic table. Properties of these materials are studied only to a limited extent. Although there are many promising avenues in terms of their medical and materials science applications, more work is needed to bring these into reality. In parallel, the study of cytotoxicity of nanoparticles as a function of its size, shape, and surface coating may find much attention in future.

Conflict of interest and funding

There is no conflict of interest in the present study for any of the authors.

References

1. Wang H, Brandl DW, Nordlander P, Halas NJ. Plasmonic nanostructures: artificial molecules. Acc Chem Res 2007; 40: 53–62.
2. Burda C, Chen X, Narayanan R, El-Sayed MA. Chemistry and properties of nanocrystals of different shapes. Chem Rev 2005; 105: 1025–102.
3. El-Sayed MA. Small is different. Shape-, size-, and composition-dependent properties of some colloidal semiconductor nanocrystals. Acc Chem Res 2004; 37: 326–33.
4. Alivisatos AP. Perspectives on the physical chemistry of semiconductor nanocrystals. J Phys Chem 1996; 100: 13226–39.
5. Tao AR, Habas S, Yang P. Shape control of colloidal metal nanocrystals. Small 2008; 4: 310–25.
6. Pileni MP. Control of the size and shape of inorganic nanocrystals at various scales from nano to macrodomains. J Phys Chem C 2007; 111: 9019–38.

7. Huang X, Neretina S, El-Sayed MA. Gold nanorods: from synthesis and properties to biological and biomedical applications. Adv Mater 2009; 21: 4880–910.

8. Daniel M-C, Astruc D. Gold nanoparticles: assembly, supramolecular chemistry, quantum-size-related properties, and applications toward biology, catalysis, and nanotechnology. Chem Rev 2003; 104: 293–346.

9. Iijima S. Helical microtubules of graphitic carbon. Nature 1991; 354: 56–8.

10. Perez-Juste J, Pastoriza-Santos I, Liz-Marzan LM, Mulvaney P. Gold nanorods: synthesis, characterization and applications. Coord Chem Rev 2005; 249: 1870–901.

11. Chang S-S, Shih C-W, Chen C-D, Lai W-C, Wang CRC. The shape transition of gold nanorods. Langmuir 1999; 15: 701–9.

12. Busbee BD, Obare SO, Murphy CJ. An improved synthesis of high-aspect-ratio gold nanorods. Adv Mater 2003; 15: 414–6.

13. Jana NR, Gearheart L, Murphy CJ. Seeding growth for size control of 5–40 nm diameter gold nanoparticles. Langmuir 2001; 17: 6782–6.

14. Jana NR, Gearheart L, Murphy CJ. Seed-mediated growth approach for shape-controlled synthesis of spheroidal and rod-like gold nanoparticles using a surfactant template. Adv Mater 2001; 13: 1389–93.

15. Chen HM, Liu R-S, Asakura K, Jang L-Y, Lee J-F. Controlling length of gold nanowires with large-scale. X-ray absorption spectroscopy approaches to the growth process. J Phys Chem C 2007; 111: 18550–7.

16. Caswell KK, Bender CM, Murphy CJ. Seedless, surfactantless wet chemical synthesis of silver nanowires. Nano Lett 2003; 3: 667–9.

17. Kim F, Sohn K, Wu J, Huang J. Chemical synthesis of gold nanowires in acidic solutions. J Am Chem Soc 2008; 130: 14442–3.

18. Hunyadi SE, Murphy CJ. Bimetallic silver-gold nanowires: fabrication and use in surface-enhanced Raman scattering. J Mater Chem 2006; 16: 3929–35.

19. Krichevski O, Markovich G. Growth of colloidal gold nanostars and nanowires induced by palladium doping. Langmuir 2007; 23: 1496–9.

20. Zhao Q, Hou L, Huang R, Li S. Controlled growth of gold nanowhiskers via a soft chemistry method. Mater Chem Phys 2004; 85: 180–3.

21. Chen J, Herricks T, Geissler M, Xia Y. Single-crystal nanowires of platinum can be synthesized by controlling the reaction rate of a polyol process. J Am Chem Soc 2004; 126: 10854–5.

22. Hu J, Odom TW, Lieber CM. Chemistry and physics in one dimension: synthesis and properties of nanowires and nanotubes. Acc Chem Res 1999; 32: 435–45.

23. Millstone JE, Park S, Shuford KL, Qin L, Schatz GC, Mirkin CA. Observation of a quadrupole plasmon mode for a colloidal solution of gold nanoprisms. J Am Chem Soc 2005; 127: 5312–3.

24. Sajanlal PR, Subramaniam C, Sasanpour P, Rashidian B, Pradeep T. Electric field enhancement and concomitant Raman spectral effects at the edges of a nanometre-thin gold mesotriangle. J Mater Chem 2010; 20: 2108–13.

25. Ah CS, Yun YJ, Park HJ, Kim W-J, Ha DH, Yun WS. Size-controlled synthesis of machinable single crystalline gold nanoplates. Chem Mater 2005; 17: 5558–61.

26. Jin R, Cao Y, Mirkin CA, Kelly KL, Schatz GC, Zheng JG. Photoinduced conversion of silver nanospheres to nanoprisms. Science 2001; 294: 1901–3.

27. Kan C, Zhu X, Wang G. Single-crystalline gold microplates: synthesis, characterization, and thermal stability. J Phys Chem B 2006; 110: 4651–6.

28. Sajanlal PR, Pradeep T. Growth of anisotropic gold nanostructures on conducting glass surfaces. J Chem Sci 2008; 120: 79–85.

29. Kim F, Connor S, Song H, Kuykendall T, Yang P. Platonic gold nanocrystals. Angew Chem Int Ed 2004; 43: 3673–7.

30. Wang L, Chen X, Zhan J, Chai Y, Yang C, Xu L, et al. Synthesis of gold nano- and microplates in hexagonal liquid crystals. J Phys Chem B 2005; 109: 3189–94.

31. Chu H-C, Kuo C-H, Huang MH. Thermal aqueous solution approach for the synthesis of triangular and hexagonal gold nanoplates with three different size ranges. Inorg Chem 2006; 45: 808–13.

32. Sun X, Dong S, Wang E. High-yield synthesis of large single-crystalline gold nanoplates through a polyamine process. Langmuir 2005; 21: 4710–2.

33. Sun X, Dong S, Wang E. Large-scale synthesis of micrometer-scale single-crystalline Au plates of nanometer thickness by a wet-chemical route. Angew Chem Int Ed 2004; 43: 6360–3.

34. Swami A, Kumar A, Selvakannan PR, Mandal S, Pasricha R, Sastry M. Highly oriented gold nanoribbons by the reduction of aqueous chloroaurate ions by hexadecylaniline Langmuir monolayers. Chem Mater 2003; 15: 17–9.

35. Burgin J, Liu M, Guyot-Sionnest P. Dielectric sensing with deposited gold bipyramids. J Phys Chem C 2008; 112: 19279–82.

36. Henzie J, Kwak E-S, Odom TW. Mesoscale metallic pyramids with nanoscale tips. Nano Lett 2005; 5: 1199–202.

37. Xu Q, Tonks I, Fuerstman MJ, Love JC, Whitesides GM. Fabrication of free-standing metallic pyramidal shells. Nano Lett 2004; 4: 2509–11.

38. Lee J, Hasan W, Stender CL, Odom TW. Pyramids: a platform for designing multifunctional plasmonic particles. Acc Chem Res 2008; 41: 1762–71.

39. Nehl CL, Liao H, Hafner JH. Optical properties of star-shaped gold nanoparticles. Nano Lett 2006; 6: 683–8.

40. Burt JL, Elechiguerra JL, Reyes-Gasga J, Montejano-Carrizales JM, Jose-Yacaman M. Beyond archimedean solids: star polyhedral gold nanocrystals. J Cryst Growth 2005; 285: 681–91.

41. Hao F, Nehl CL, Hafner JH, Nordlander P. Plasmon resonances of a gold nanostar. Nano Lett 2007; 7: 729–32.

42. Kumar PS, Pastoriza-Santos I, Rodriguez-Gonzalez B, de Abajo FJG, Liz-Marzan LM. Nanotechnology 2008; 19: 015606.

43. Sajanlal PR, Sreeprasad TS, Nair AS, Pradeep T. Wires, plates, flowers, needles, and core-shells: diverse nanostructures of gold using polyaniline templates. Langmuir 2008; 24: 4607–14.

44. Jena BK, Raj CR. Seedless, surfactantless room temperature synthesis of single crystalline fluorescent gold nanoflowers with pronounced SERS and electrocatalytic activity. Chem Mater 2008; 20: 3546–8.

45. Bakshi MS, Possmayer F, Petersen NO. Role of different phospholipids in the synthesis of pearl-necklace-type gold-silver bimetallic nanoparticles as bioconjugate materials. J Phys Chem C 2007; 111: 14113–24.

46. Li Y, Shi G. Electrochemical growth of two-dimensional gold nanostructures on a thin polypyrrole film modified ITO electrode. J Phys Chem B 2005; 109: 23787–93.

47. Jena BK, Raj CR. Synthesis of flower-like gold nanoparticles and their electrocatalytic activity towards the oxidation of methanol and the reduction of oxygen. Langmuir 2007; 23: 4064–70.

48. Wang W, Cui H. Chitosan-luminol reduced gold nanoflowers: from one-pot synthesis to morphology-dependent SPR and chemiluminescence sensing. J Phys Chem C 2008; 112: 10759–66.

49. Qian L, Yang X. Polyamidoamine dendrimers-assisted electro-deposition of gold-platinum bimetallic nanoflowers. J Phys Chem B 2006; 110: 16672–8.

50. Yang Z, Lin ZH, Tang CY, Chang HT. Preparation and characterization of flower-like gold nanomaterials and iron oxide/gold composite nanomaterials. Nanotechnology 2007; 18: 255–606.

51. Yuan H, Ma W, Chen C, Zhao J, Liu J, Zhu H, et al. Shape and SPR evolution of thorny gold nanoparticles promoted by silver ions. Chem Mater 2007; 19: 1592–600.

52. Hao E, Bailey RC, Schatz GC, Hupp JT, Li S. Synthesis and optical properties of "branched" gold nanocrystals. Nano Lett 2004; 4: 327–30.

53. Chen HM, Hsin CF, Liu R-S, Lee J-F, Jang L-Y. Synthesis and characterization of multi-pod-shaped gold/silver nanostructures. J Phys Chem C 2007; 111: 5909–14.

54. Bakr OM, Wunsch BH, Stellacci F. High-yield synthesis of multi-branched urchin-like gold nanoparticles. Chem Mater 2006; 18: 3297–301.

55. Chen J, Herricks T, Xia Y. Polyol synthesis of platinum nanostructures: control of morphology through the manipulation of reduction kinetics. Angew Chem 2005; 117: 2645–8.

56. Kuo C-H, Huang MH. Synthesis of branched gold nanocrystals by a seeding growth approach. Langmuir 2005; 21: 2012–6.

57. Liang H-P, Hu J-S, Cao A-M, Mu Y-Y, Wan L-J. Facile synthesis of Pt multipods nanocrystals. J Nanosci Nanotechnol 2006; 6: 2031–6.

58. Tsuji M, Jiang P, Hikino S, Lim S, Yano R, Jang S-M, et al. Toward to branched platinum nanoparticles by polyol reduction: a role of poly(vinylpyrrolidone) molecules. Colloids Surf A 2008; 317: 23–31.

59. Bakr OM, Wunsch BH, Stellacci F. High-yield synthesis of multi-branched urchin-like gold nanoparticles. Chem Mater 2006; 18: 3297–301.

60. Hu J, Zhang Y, Liu B, Liu J, Zhou H, Xu Y, et al. Synthesis and properties of tadpole-shaped gold nanoparticles. J Am Chem Soc 2004; 126: 9470–1.

61. Skrabalak SE, Au L, Li X, Xia Y. Facile synthesis of Ag nanocubes and Au nanocages. Nat Protoc 2007; 2: 2182–90.

62. Talley CE, Jackson JB, Oubre C, Grady NK, Hollars CW, Lane SM, et al. Surface-enhanced Raman scattering from individual Au nanoparticles and nanoparticle dimer substrates. Nano Lett 2005; 5: 1569–74.

63. Wang H, Brandl DW, Le F, Nordlander P, Halas NJ. Nanorice: a hybrid plasmonic nanostructure. Nano Lett 2006; 6: 827–32.

64. Teranishi T, Inoue Y, Nakaya M, Oumi Y, Sano T. Nano-acorns: anisotropically phase-segregated CoPd sulfide nanoparticles. J Am Chem Soc 2004; 126: 9914–5.

65. Sun Y, Mayers BT, Xia Y. Template-engaged replacement reaction: a one-step approach to the large-scale synthesis of metal nanostructures with hollow interiors. Nano Lett 2002; 2: 481–5.

66. Cobley CM, Campbell DJ, Xia Y. Tailoring the optical and catalytic properties of gold-silver nanoboxes and nanocages by introducing palladium. Adv Mater 2008; 20: 748–52.

67. Gunawidjaja R, Peleshanko S, Ko H, Tsukruk VV. Bimetallic nanocobs: decorating silver nanowires with gold nanoparticles. Adv Mater 2008; 20: 1544–9.

68. Metraux GS, Cao YC, Jin R, Mirkin CA. Triangular nanoframes made of gold and silver. Nano Lett 2003; 3: 519–22.

69. Huang C-C, Yang Z, Chang H-T. Synthesis of dumbbell-shaped Au-Ag core-shell nanorods by seed-mediated growth under alkaline conditions. Langmuir 2004; 20: 6089–92.

70. Eustis S, El-Sayed MA. Why gold nanoparticles are more precious than pretty gold: noble metal surface plasmon resonance and its enhancement of the radiative and nonradia-tive properties of nanocrystals of different shapes. Chem Soc Rev 2006; 35: 209–17.

71. Grzelczak M, Perez-Juste J, Mulvaney P, Liz-Marzan LM. Shape control in gold nanoparticle synthesis. Chem Soc Rev 2008; 37: 1783–91.

72. Sau TK, Rogach AL. Nonspherical noble metal nanoparticles: colloid-chemical synthesis and morphology control. Adv Mater 2010; 22: 1781–804.

73. Sau TK, Rogach AL, Jackel F, Klar TA, Feldmann J. Properties and applications of colloidal nonspherical noble metal nanoparticles. Adv Mater 2010; 22: 1805–25.

74. Elechiguerra JL, Reyes-Gasga J, Yacaman MJ. The role of twinning in shape evolution of anisotropic noble metal nanostructures. J Mater Chem 2006; 16: 3906–19.

75. Sharma V, Park K, Srinivasarao M. Colloidal dispersion of gold nanorods: historical background, optical properties, seed-mediated synthesis, shape separation and self-assembly. Materials Science and Engineering R Reports 2009; 65: 1–38.

76. Yong K-T, Swihart MT, Ding H, Prasad PN. Preparation of gold nanoparticles and their applications in anisotropic nanoparticle synthesis and bioimaging. Plasmonics 2009; 4: 79–93.

77. Myroshnychenko V, Rodriguez-Fernandez J, Pastoriza-Santos I, Funston AM, Novo C, Mulvaney P, et al. Modelling the optical response of gold nanoparticles. Chem Soc Rev 2008; 37: 1792–805.

78. El-Sayed MA. Some interesting properties of metals confined in time and nanometer space of different shapes. Acc Chem Res 2001; 34: 257–64.

79. O'Handley RC. Modern magnetic materials, principles and applications. New York: Wiley-Interscience Publication; 2000.

80. Goodman CM, McCusker CD, Yilmaz T, Rotello VM. Toxicity of gold nanoparticles functionalized with cationic and anionic side chains. Bioconjugate Chem 2004; 15: 897–900.

81. Lee KJ, Nallathamby PD, Browning LM, Osgood CJ, Xu XHN. In vivo imaging of transport and biocompatibility of single silver nanoparticles in early development of zebrafish embryos. ACS Nano 2007; 1: 133–43.

82. Hirsch LR, Stafford RJ, Bankson JA, Sershen SR, Rivera B, Price RE, et al. Nanoshell-mediated near-infrared thermal therapy of tumors under magnetic resonance guidance. Proc Natl Acad Sci USA 2003; 100: 13549–54.

83. Link S, Furube A, Mohamed MB, Asahi T, Masuhara H, El-Sayed MA. Hot electron relaxation dynamics of gold nanoparticles embedded in $MgSO_4$ powder compared to solution: the effect of the surrounding medium. J Phys Chem B 2002; 106: 945–55.

84. Link S, El-Sayed MA. Optical properties and ultrafast dynamics of metallic nanocrystals. Annu Rev Phys Chem 2003; 54: 331–66.

85. Salem AK, Searson PC, Leong KW. Multifunctional nanorods for gene delivery. Nat Mater 2003; 2: 668–71.

86. Salem AK, Hung CF, Kim TW, Wu TC, Searson PC, Leong KW. Multi-component nanorods for vaccination applications. Nanotechnology 2005; 16: 484–7.

87. Hu M, Chen J, Li Z-Y, Au L, Hartland GV, Li X, et al. Gold nanostructures: engineering their plasmonic properties for biomedical applications. Chem Soc Rev 2006; 35: 1084–94.

88. Jain PK, Eustis S, El-Sayed MA. Plasmon coupling in nanorod assemblies: optical absorption, discrete dipole approximation simulation, and exciton-coupling model. J Phys Chem B 2006; 110: 18243–53.

89. Lowery AR, Gobin AM, Day ES, Halas NJ. Immunonanoshells for targeted photothermal ablation of tumor cells. Int J Nanomed 2006; 1: 1–6.

90. Loo C, Lin A, Hirsch L, Lee M-H, Barton J, Halas N, et al. Nanoshell-enabled photonics-based imaging and therapy of cancer. Technol Cancer Res Treat 2004; 3: 33–40.

91. Mohamed MB, Temer SA, Link S, Braun M, El-Sayed MA. Hot electron and phonon dynamics of gold nanoparticles embedded in a gel matrix. Chem Phys Lett 2001; 343: 55–63.

92. Murphy CJ, Gole AM, Stone JW, Sisco PN, Alkilany AM, Goldsmith EC, et al. Gold nanoparticles in biology: beyond toxicity to cellular imaging. Acc Chem Res 2008; 41: 1721–30.

93. Arap W, Pasqualini R, Ruoslahti E. Cancer treatment by targeted drug delivery to tumor vasculature in a mouse model. Science 1998; 279: 377–80.

94. James WD, Hirsch LR, West JL, O'Neal PD, Payne JD. Application of INAA to the build-up and clearance of gold nanoshells in clinical studies in mice. J Radioanal Nucl Chem 2007; 271: 455–9.

95. Huang X, Qian W, El-Sayed IH, El-Sayed MA. The potential use of the enhanced nonlinear properties of gold nanospheres in photothermal cancer therapy. Lasers Med Sci 2007; 39: 747–53.

96. Loo C, Lowery A, Halas NJ, West J, Drezek R. Immunotargeted nanoshells for integrated cancer imaging and therapy. Nano Lett 2005; 5: 709–11.

97. Wang Y, Xie X, Wang X, Ku G, Gill KL, O'Neal DP, et al. Photoacoustic tomography of a nanoshell contrast agent in the in vivo rat brain. Nano Lett 2004; 4: 1689–92.

98. O'Neal DP, Hirsch LR, Halas NJ, Payne JD, West JL. Photothermal tumor ablation in mice using near infrared-absorbing nanoparticles. Cancer Lett 2004; 209: 171–6.

99. Elghanian R, Storhoff JJ, Mucic RC, Letsinger RL, Mirkin CA. Selective colorimetric detection of polynucleotides based on the distance-dependent optical properties of gold nanoparticles. Science 1997; 277: 1078–80.

100. Nam JM, Thaxton CC, Mirkin CA. Nanoparticles-based bio-bar codes for the ultrasensitive detection of proteins. Science 2003; 301: 1884–6.

101. Katz E, Willner I. Integrated nanoparticle-biomolecule hybrid systems: synthesis, properties, and applications. Angew Chem Int Ed 2004; 43: 6042–108.

102. Huang X, Jain PK, El-Sayed IH, El-Sayed MA. Gold nanoparticles: interesting optical properties and recent applications in cancer diagnostics and therapy. Nanomedicine 2007; 2: 681–93.

103. Willets KA, Van DRP. Localized surface plasmon resonance spectroscopy and sensing. Annu Rev Phys Chem 2007; 58: 267–97.

104. Kneipp K, Moskovits M, Kneipp H. Surface-enhanced Raman scattering: physics and applications. Berlin, New York: Springer; 2006.

105. Kneipp K, Kneipp H, Itzkan I, Dasari RR, Feld MS. Ultrasensitive chemical analysis by Raman spectroscopy. Chem Rev 1999; 99: 2957–75.

106. Orendorff CJ, Gole A, Sau TK, Murphy CJ. Surface-enhanced Raman spectroscopy of self-assembled monolayers: sandwich architecture and nanoparticle shape dependence. Anal Chem 2005; 77: 3261–6.

107. Hu J-Q, Chen Q, Xie Z-X, Han G-B, Wang R-H, Ren B, et al. A simple and effective route for the synthesis of crystalline silver nanorods and nanowires. Adv Funct Mater 2004; 14: 183–9.

108. Campion A, Kambhampati P. Surface-enhanced Raman scattering. Chem Soc Rev 1998; 27: 241–50.

109. Wang H, Levin CS, Halas NJ. Nanosphere arrays with controlled sub-10-nm gaps as surface-enhanced Raman spectroscopy substrates. J Am Chem Soc 2005; 127: 14992–3.

110. Nie S, Emory SR. Probing single molecules and single nanoparticles by surface-enhanced Raman scattering. Science 1997; 275: 1102–6.

111. O'Neal PD, Cote GL, Motamedi M, Chen J, Lin W-C. Feasibility study using surface-enhanced Raman spectroscopy for the quantitative detection of excitatory amino acids. J Biomed Opt 2003; 8: 33–9.

112. Sulk R, Chan C, Guicheteau J, Gomez C, Heyns JBB, Corcoran R, et al. Surface-enhanced Raman assays (SERA): measurement of bilirubin and salicylate. J Raman Spectrosc 1999; 30: 853–9.

113. Yang Y, Matsubara S, Xiong L, Hayakawa T, Nogami M. Solvothermal synthesis of multiple shapes of silver nanoparticles and their SERS properties. J Phys Chem C 2007; 111: 9095–104.

114. Haes AJ, Haynes CL, McFarland AD, Schatz GC, van Duyne RP, Zou S. Plasmonic materials for surface-enhanced sensing and spectroscopy. MRS Bull 2005; 30: 368–75.

115. Banholzer MJ, Millstone JE, Qin L, Mirkin CA. Rationally designed nanostructures for surface-enhanced Raman spectroscopy. Chem Soc Rev 2008; 37: 885–97.

116. Jensen L, Aikens CM, Schatz GC. Electronic structure methods for studying surface-enhanced Raman scattering. Chem Soc Rev 2008; 37: 1061–73.

117. Willets KA, Van Duyne RP. Localized surface plasmon resonance spectroscopy and sensing. Annu Rev Phys Chem 2007; 58: 267–97.

118. Ray PC. Size and shape dependent second order nonlinear optical properties of nanomaterials and their application in biological and chemical sensing. Chem Rev 2010; 110: 5332–65.

119. Segets D, Tomalino LM, Gradl J, Peukert WJ. Real-time monitoring of the nucleation and growth of ZnO nanoparticles using an optical Hyper-Rayleigh scattering method. J Phys Chem C 2009; 113: 11995–2001.

120. Neely A, Perry C, Varisli B, Singh A, Arbneshi T, Senapati D, et al. Ultrasensitive and highly selective detection of Alzheimer's disease biomarker using two-photon Rayleigh scattering properties of gold nanoparticle. ACS Nano 2009; 3: 2834–40.

121. Wang G, Sun WJ. Optical limiting of gold nanoparticle aggregates induced by electrolytes. J Phys Chem B 2006; 110: 20901–5.

122. Kneipp J, Kneipp H, Wittig B, Kneipp K. One- and two-photon excited optical pH probing for cells using Surface-Enhanced Raman and Hyper-Raman nanosensors. Nano Lett 2007; 7: 2819–23.

123. Duboisset I, Russier-Antoine E, Benichou G, Jonin BC, Brevet PF. Single metallic nanoparticle sensitivity with Hyper Rayleigh Scattering. J Phys Chem C 2009; 113: 13477–81.

124. Singh AK, Senapati D, Wang S, Griffin J, Neely A, Candice P, et al. Gold nanorod based selective identification of escherichia coli bacteria using two-photon Rayleigh Scattering Spectroscopy. ACS Nano 2009; 3: 1906–12.

125. Nath N, Chilkoti A. Label-free biosensing by surface plasmon resonance of nanoparticles on glass. Optimization of nanoparticle size. Anal Chem 2004; 76: 5370–8.

126. Orendorff CJ, Gole A, Sau TK, Murphy CJ. Surface-enhanced Raman spectroscopy of self-assembled monolayers: sandwich architecture and nanoparticle shape dependence. Anal Chem 2005; 77: 3261–6.

127. Hu J, Wang Z, Li J. Gold nanoparticles with special shapes: controlled synthesis, surface-enhanced Raman scattering, and the application in biodetection. Sensors 2007; 7: 3299–311.

128. He L, Musick MD, Nicewarner SR, Salinas FG, Benkovic SJ, Natan MJ, et al. Colloidal Au-enhanced surface plasmon resonance for ultrasensitive detection of DNA hybridization. J Am Chem Soc 2000; 122: 9071–7.

129. Maxwell DJ, Taylor JR, Nie SM. Self-assembled nanoparticle probes for recognition and detection of biomolecules. J Am Chem Soc 2002; 124: 9606–12.

130. Dickerson MB, Sandhage KH, Naik RR. Protein- and peptide-directed syntheses of inorganic materials. Chem Rev 2008; 108: 4935–78.

131. He W, Henne WA, Wei Q, Zhao Y, Doorneweerd DD, Wei A. Two-photon luminescence imaging of bacillus spores using peptide-functionalized gold nanorods. Nano Res 2008; 1: 450–6.

132. Wang H, Huff TB, Zweifel DA, He W, Low PS, Wei A, et al. In vitro and in vivo two-photon luminescence imaging of single gold nanorods. Proc Natl Acad Sci USA 2005; 102: 15752–6.

133. Durr NJ, Larson T, Smith DK, Korgel BA, Sokolov K, Ben-Yakar A. Two-photon luminescence imaging of cancer cells using molecularly targeted gold nanorods. Nano Lett 2007; 7: 941–5.

134. Black KC, Kirkpatrick ND, Troutman TS, Xu L, Vagner J, Gillies RJ, et al. Gold nanorods targeted to delta opioid receptor: plasmon-resonant contrast and photothermal agents. Mol Imaging 2008; 7: 50–7.

135. Liz Marzán LM. (Non-carbon) anisotropic nanomaterials. J Mater Chem 2006; 16: 3891–2.

136. Teo BK, Sun XH. Classification and representations of low-dimensional nanomaterials: terms and symbols. J Clust Sci 2007; 18: 346–57.

137. Sun XH, Wong NB, Li CP, Lee ST, Sham TK. Chainlike silicon nanowires: morphology, electronic structure and luminescence studies. J Appl Phys 2004; 96: 3447–51.

138. Sun XH, Li CP, Wong NB, Lee CS, Lee ST, Teo BK. Reductive growth of nanosized ligated metal clusters on silicon nanowires. Inorg Chem 2002; 41: 4331–6.

139. Sun X-H, Li C-P, Wong N-B, Lee C-S, Lee S-T, Teo B-K. Templating effect of hydrogen-passivated silicon nanowires in the production of hydrocarbon nanotubes and nanoonions via sonochemical reactions with common organic solvents under ambient conditions. J Am Chem Soc 2002; 124: 14856–7.

140. Li CP, Teo BK, Sun XH, Wong NB, Lee ST. Hydrocarbon and carbon nanostructures produced by sonochemical reactions of organic solvents on hydrogen-passivated silicon nanowires under ambient conditions. Chem Mater 2005; 17: 5780–8.

141. Hu J, Ouyang M, Yang P, Lieber CM. Controlled growth and electrical properties of heterojunctions of carbon nanotubes and silicon nanowires. Nature 1999; 399: 48–51.

142. Teo BK, Li CP, Sun XH, Wong NB, Lee ST. Silicon-silica nanowires, nanotubes, and biaxial nanowires: inside, outside, and side-by-side growth of silicon versus silica on zeolite. Inorg Chem 2003; 42: 6723–8.

143. Jung Y, Ko D-K, Agarwal R. Synthesis and structural characterization of single-crystalline branched nanowire heterostructures. Nano Lett 2007; 7: 264–8.

144. Ogino T, Hibino H, Homma Y, Kobayashi Y, Prabhakaran K, Sumitomo K, et al. Fabrication and integration of nanostructures on Si surfaces. Acc Chem Res 1999; 32: 447–54.

145. Hochbaum AI, Fan R, He R, Yang P. Controlled growth of Si nanowire arrays for device integration. Nano Lett 2005; 5: 457–60.

146. Schaffler F. High-mobility Si and Ge structures. Semicond Sci Technol 1997; 12: 1515–49.

147. Whall TE, Parker EHC. SiGe—heterostructures for CMOS technology. Thin Solid Films 2000; 367: 250–9.

148. Whall TE, Parker EHC. Si-Ge heterostructures for FET applications. J Phys D Appl Phys 1998; 31: 1397–416.

149. Brunner K. Si/Ge nanostructures. Rep Prog Phys 2002; 65: 27–72.

150. Xia Y, Rogers JA, Paul KE, Whitesides GM. Unconventional methods for fabricating and patterning nanostructures. Chem Rev 1999; 99: 1823–48.

151. Rao CNR, Kulkarni GU, Thomas PJ, Edwards PP. Metal nanoparticles and their assemblies. Chem Soc Rev 2000; 29: 27–35.

152. Tao AR, Huang J, Yang P. Langmuir-blodgettry of nanocrystals and nanowires. Acc Chem Res 2008; 41: 1662–73.

153. Pileni MP. Self-assemblies of nanocrystals: fabrication and collective properties. J Phys Chem B 2001: 105: 3358–71

154. Harfenist SA, Wang ZL, Alvarez MM, Vezmar I, Whetten RL. Highly oriented molecular Ag nanocrystal arrays. J Phys Chem 1996; 100: 13904–10.

155. Leontidis E, Kleitou K, Kyprianidou-Leodidou T, Bekiari V, Lianos P. Gold colloids from cationic surfactant solutions. 1. Mechanisms that control particle morphology. Langmuir 2002; 18: 3659–68.

156. Berhault G, Bausach M, Bisson L, Becerra L, Thomazeau C, Uzio D. Seed-mediated synthesis of Pd nanocrystals: factors influencing a kinetic- or thermodynamic-controlled growth regime. J Phys Chem C 2007; 111: 5915–25.

157. Murphy CJ, Sau TK, Gole A, Orendorff CJ. Surfactant-directed synthesis and optical properties of one-dimensional plasmonic metallic nanostructures. MRS Bull 2005; 30: 349–55.

158. Bogels G, Meekes H, Bennema P, Bollen D. Growth mechanism of vapor-grown silver crystals: relation between twin formation and morphology. J Phys Chem B 1999; 103: 7577–83.

159. Lofton C, Sigmund W. Mechanisms controlling crystal habits of gold and silver colloids. Adv Func Mater 2005; 15: 1197–208.

160. Zsigmondy R. The chemistry of colloids. New York: John Wiley; 1917.

161. Jana NR, Gearheart L, Murphy CJ. Wet chemical synthesis of high aspect ratio cylindrical gold nanorods. J Phys Chem B 2001; 105: 4065–7.

162. Ha TH, Koo H-J, Chung BH. Shape-controlled syntheses of gold nanoprisms and nanorods influenced by specific adsorption of halide ions. J Phys Chem C 2006; 111: 1123–30.

163. Millstone JE, Metraux GS, Mirkin CA. Controlling the edge length of gold nanoprisms via a seed-mediated approach. Adv Funct Mater 2006; 16: 1209–14.

164. Sajanlal PR, Pradeep T. Electric-field-assisted growth of highly uniform and oriented gold nanotriangles on conducting glass substrates. Adv Mater 2008; 20: 980–3.

165. Chen S, Carroll DL. Silver nanoplates. Size control in two dimensions and formation mechanisms. J Phys Chem B 2004; 108: 5500–6.

166. Fan F-R, Liu D-Y, Wu Y-F, Duan S, Xie Z-X, Jiang Z-Y, et al. Epitaxial growth of heterogeneous metal nanocrystals: from gold nano-octahedra to palladium and silver nanocubes. J Am Chem Soc 2008; 130: 6949–51.

167. Cho EC, Camargo PHC, Xia Y. Synthesis and characterization of noble-metal nanostructures containing gold nanorods in the center. Adv Mater 2010; 22: 744–8.

168. Sau TK, Murphy CJ. Room temperature, high-yield synthesis of multiple shapes of gold nanoparticles in aqueous solution. J Am Chem Soc 2004; 126: 8648–9.

169. Sajanlal PR, Pradeep T. Mesoflowers: a new class of highly efficient surface-enhanced Raman active and infrared-absorbing materials. Nano Res 2009; 2: 306–20.

170. Murphy CJ, Sau TK, Gole AM, Orendorff CJ, Gao J, Gou L, et al. Anisotropic metal nanoparticles: synthesis, assembly, and optical applications. J Phys Chem B 2005; 109: 13857–70.

171. Johnson CJ, Dujardin E, Davis SA, Murphy CJ, Mann S. Growth and form of gold nanorods prepared by seed-mediated, surfactant-directed synthesis. J Mater Chem 2002; 12: 1765–70.

172. Perez-Juste J, Liz-Marzan LM, Carnie S, Chan DYC, Mulvaney P. Electric-field-directed growth of gold nanorods in aqueous surfactant solutions. Adv Funct Mater 2004; 14: 571–9.

173. Samal A, Sreeprasad T, Pradeep T. Investigation of the role of $NaBH_4$ in the chemical synthesis of gold nanorods. J Nanopart Res 2010; 12: 1777–86.

174. Fievet F, Lagier JP, Figlarz M. Preparing monodisperse metal powders in micrometer and submicrometer sizes by the polyol process. MRS Bull 1989; 14: 29–34.

175. Viau G, Fievet-Vincent F, Fievet F. Nucleation and growth of bimetallic CONI and FENI monodisperse particles prepared in polyols. Solid State Ionics 1996; 84: 259–70.

176. Sun Y, Yin Y, Mayers BT, Herricks T, Xia Y. Uniform silver nanowires synthesis by reducing AgNo3 with ethylene glycol in the presence of seeds and poly(vinyl pyrrolidone). Chem Mater 2002; 14: 4736–45.

177. Wiley B, Sun Y, Mayers B, Xia Y. Shape-controlled synthesis of metal nanostructures: the case of silver. Chem Eur J 2005; 11: 454–63.

178. Lu X, Rycenga M, Skrabalak SE, Wiley B, Xia Y. Chemical synthesis of novel plasmonic nanoparticles. Annu Rev Phys Chem 2009; 60: 167–92.

179. Wiley B, Sun Y, Xia Y. Synthesis of silver nanostructures with controlled shapes and properties. Acc Chem Res 2007; 40: 1067–76.

180. Sun Y, Xia Y. Shape-controlled synthesis of gold and silver nanoparticles. Science 2002; 298: 2176–9.

181. Im SH, Lee YT, Wiley B, Xia Y. Large-scale synthesis of silver nanocubes: the role of HCl in promoting cube perfection and monodispersity. Angew Chem Int Ed 2005; 44: 2154–7.

182. Xiong Y, Siekkinen AR, Wang J, Yin Y, Kim MJ, Xia Y. Synthesis of silver nanoplates at high yields by slowing down the polyol reduction of silver nitrate with polyacrylamide. J Mater Chem 2007; 17: 2600–2.

183. Seo D, Park JC, Song H. Polyhedral gold nanocrystals with OH symmetry: from octahedra to cubes. J Am Chem Soc 2006; 128: 14863–70.

184. Li C, Shuford KL, Chen M, Lee EJ, Cho SO. A facile polyol route to uniform gold octahedra with tailorable size and their optical properties. ACS Nano 2008; 2: 1760–9.

185. Yu SH. Bio-inspired crystal growth by synthetic templates. Top Curr Chem 2007; 271: 79–118.

186. Klaus T, Joerger R, Olsson E, Granqvist C-G. Silver-based crystalline nanoparticles, microbially fabricated. Proc Natl Acad Sci USA 1999; 96: 13611–4.

187. Brown S, Sarikaya M, Johnson E. A genetic analysis of crystal growth. J Mol Biol 2000; 299: 725–35.

188. Shankar SS, Rai A, Ankamwar B, Singh A, Ahmad A, Sastry M. Biological synthesis of triangular gold nanoprisms. Nat Mater 2004; 3: 482–8.

189. Shankar SS, Rai A, Ahmad A, Sastry M. Controlling the optical properties of lemongrass extract synthesized gold nanotriangles and potential application in infrared-absorbing optical coatings. Chem Mater 2005; 17: 566–72.

190. Ankamwar B, Chaudhary M, Sastry M. Gold nanotriangles biologically synthesized using tamarind leaf extract and potential application in vapor sensing. Synth React Inorg Me 2005; 35: 19–26.

191. Smitha SL, Philip D, Gopchandran KG. Green synthesis of gold nanoparticles using cinnamomum zeylanicum leaf broth. Spectrochim Acta A 2009; 74: 735–9.

192. Liu B, Xie J, Lee JY, Ting YP, Chen JP. Optimization of high-yield biological synthesis of single-crystalline gold nanoplates. J Phys Chem B 2005; 109: 15256–63.

193. Xie J, Lee JY, Wang DIC, Ting YP. Silver nanoplates: from biological to biomimetic synthesis. ACS Nano 2007; 1: 429–39.

194. Xie J, Lee JY, Wang DIC, Ting YP. Identification of active biomolecules in the high-yield synthesis of single-crystalline gold nanoplates in algal solutions. Small 2007; 3: 672–82.

195. He S, Zhang Y, Guo Z, Gu N. Biological synthesis of gold nanowires using extract of rhodopseudomonas capsulate. Biotechnol Prog 2008; 24: 476–80.

196. Nair B, Pradeep T. Coalescence of nanoclusters and formation of submicron crystallites assisted by lactobacillus strains. Cryst Growth Des 2002; 2: 293–8.

197. Lu C, Qi L, Yang J, Tang L, Zhang D, Ma J. Hydrothermal growth of large-scale micropatterned arrays of ultralong ZnO nanowires and nanobelts on zinc substrate. Chem Commun 2006: 3551–3.

198. Cansell F, Chevalier B, Demourgues A, Etourneau J, Even C, Garrabos Y, et al. Supercritical fluid processing: a new route for materials synthesis. J Mater Chem 1999; 9: 67–75.

199. Adams BD, Wu G, Nigro S, Chen A. Facile synthesis of Pd-Cd nanostructures with high capacity for hydrogen storage. J Am Chem Soc 2009; 131: 6930–1.

200. Yuan J, Li W-N, Gomez S, Suib SL. Shape-controlled synthesis of manganese oxide octahedral molecular sieve three-dimensional nanostructures. J Am Chem Soc 2005; 127: 4184–5.

201. Li Y-J, Wang C-Y, Lu M-Y, Li K-M, Chen L-J. Electrode-posited hexagonal ringlike superstructures composed of hexagonal Co-doped ZnO nanorods with optical tuning and high-temperature ferromagnetic properties. Cryst Growth Des 2008; 8: 2598–602.

202. Shen G, Chen D. Self-coiling of $Ag_2V_4O_{11}$ nanobelts into perfect nanorings and microloops. J Am Chem Soc 2006; 128: 11762–3.

203. Tian L, Tan HY, Vittal JJ. Morphology-controlled synthesis of Bi_2S_3 nanomaterials via single- and multiple-source approaches. Cryst Growth Des 2008; 8: 734–8.

204. Chang C-C, Wu H-L, Kuo C-H, Huang MH. Hydrothermal synthesis of monodispersed octahedral gold nanocrystals with five different size ranges and their self-assembled structures. Chemistry of Materials 2008; 20: 7570–4.

205. Lu Q, Gao F, Komarneni S. Biomolecule-assisted reduction in the synthesis of single-crystalline tellurium nanowires. Adv Mater 2004; 16: 1629–32.

206. Wang Z, Wang L, Wang H. Peg-mediated hydrothermal growth of single-crystal tellurium nanotubes. Cryst Growth Des 2008; 8: 4415–9.

207. Brenner A, Riddell GE. Nickel plating on steel. Good-quality deposits by chemical reaction. J Res Natl Bur Stand (US) 1946; 37: 31–4.

208. Sun Y. Direct growth of dense, pristine metal nanoplates with well-controlled dimensions on semiconductor substrates. Chem Mater 2007; 19: 5845–7.

209. Aizawa M, Cooper AM, Malac M, Buriak JM. Silver nano-inukshuks on germanium. Nano Lett 2005; 5: 815–9.

210. Fang, Fang J, You H, Kong P, Yi Y, Song X, Ding B. Dendritic silver nanostructure growth and evolution in replacement reaction. Cryst Growth Des 2007; 7: 864–7.

211. Fang J, Ma X, Cai H, Song X, Ding B. Nanoparticle-aggregated 3D monocrystalline gold dendritic nanostructures. Nanotechnology 2006; 17: 5841–5.

212. Sun Y, Xia Y. Mechanistic study on the replacement reaction between silver nanostructures and chloroauric acid in aqueous medium. J Am Chem Soc 2004; 126: 3892–901.

213. Au L, Chen Y, Zhou F, Camargo PHC, Lim B, Li Z-Y, et al. Synthesis and optical properties of cubic gold nanoframes. Nano Res 2008; 1: 441–9.

214. Xiong Y, Wiley BJ, Chen J, Li Z-Y, Yin Y, Xia Y. Corrosion-based synthesis of single-crystal Pd nanoboxes and nanocages and their surface plasmon properties. Angew Chem Int Ed 2005; 44: 7913–7.

215. Kim D, Park J, An K, Yang N-K, Park J-G, Hyeon T. Synthesis of hollow iron nanoframes. J Am Chem Soc 2007; 129: 5812–3.

216. Sun Y, Xia Y. Multiple-walled nanotubes made of metals. Adv Mater 2004; 16: 264–8.

217. Esumi K, Matsuhisa K, Torigoe K. Preparation of rodlike gold particles by UV irradiation using cationic micelles as a template. Langmuir 1995; 11: 3285–7.

218. Kim F, Song JH, Yang P. Photochemical synthesis of gold nanorods. J Am Chem Soc 2002; 124: 14316–7.

219. Kundu S, Liang H. Photochemical synthesis of electrically conductive CDS nanowires on DNA scaffolds. Adv Mater 2008; 20: 826–31.

220. Luoa X, Imae T. Photochemical synthesis of crown-shaped platinum nanoparticles using aggregates of G4-NH2 PAMAM dendrimer as templates. J Mater Chem 2007; 17: 567–71.

221. Jin R, Cao YC, Hao E, Métraux GS, Schatz GC, Mirkin CA. Controlling anisotropic nanoparticle growth through plasmon excitation. Nature 2003; 425: 487–90.

222. Huang W-C, Chen Y-C. Photochemical synthesis of polygonal gold nanoparticles. J Nanopart Res 2008; 10: 697–702.

223. Reetz MT, Helbig W. Size-selective synthesis of nanostructured transition metal clusters. J Am Chem Soc 1994; 116: 7401–2.

224. Huang C-J, Chiu P-H, Wang Y-H, Chen WR, Mee TH. Synthesis of the gold nanocubes by electrochemical technique. J Electrochem Soc 2006; 153: D129–33.

225. Yu Y-Y, Chang S-S, Lee C-L, Wang CRC. Gold nanorods: electrochemical synthesis and optical properties. J Phys Chem B 1997; 101: 6661–4.

226. Tian N, Zhou Z-Y, Sun S-G, Cui L, Ren B, Tian Z-Q. Electrochemical preparation of platinum nanothorn assemblies with high surface enhanced Raman scattering activity. Chem Commun 2006; 4090–2.

227. Gu C, Zhang T-Y. Electrochemical synthesis of silver poly-hedrons and dendritic films with superhydrophobic surfaces. Langmuir 2008; 24: 12010–6.

228. Sun Y, Qiao R. Facile tuning of superhydrophobic states with Ag nanoplates. Nano Res 2008; 1: 292–302.

229. Liang H-W, Liu S, Yu S-H. Controlled synthesis of one-dimensional inorganic nanostructures using pre-existing one-dimensional nanostructures as templates. Adv Mater 2010; 22: 3925–37.

230. Meng, GW, Han, FM, Zhao, X L, Chen, BS, Yang, DC, Liu, JX, Xu, QL, Kong, MG, Zhu, XG, Jung, YJ, et al. A general synthetic approach to interconnected nanowire/nanotube and nanotube/nanowire/nanotube heterojunctions with branched topology. Angew Chem Int Ed 2009; 48: 7166–70.

231. Foss CA Jr, Hornyak GL, Stockert JA, Martin CR. Optical properties of composite membranes containing arrays of nanoscopic gold cylinders. J Phys Chem 1992; 96: 7497–9.

232. Martin CR. Nanomaterials: a membrane-based synthetic approach. Science 1994; 266: 1961–6.

233. Hulteen JC, Martin CR. A general template-based method for the preparation of nanomaterials. J Mater Chem 1997; 7: 1075–87.

234. van der Zande B, Böhmer MR, Fokkink LGJ, Schönenberger C. Colloidal dispersions of gold rods. Synthesis and optical properties. Langmuir 2000; 16: 451–8.

235. Brus L. Noble metal nanocrystals: plasmon electron transfer photochemistry and single-molecule Raman spectroscopy. Accounts of Chemical Research 2008; 41: 1742–9.

236. Noguez C. Surface plasmons on metal nanoparticles: the influence of shape and physical environment. J Phys Chem C 2007; 111: 3806–19.

237. Kreibig U, Vollmer M. Optical properties of metal clusters. Berlin: Springer; 1995.

238. Nelayah J, Kociak M, Stephan O, Garcia de Abajo FJ, Tence M, Henrard L, et al. Mapping surface plasmons on a single metallic nanoparticle. Nat Phys 2007; 3: 348–53.

239. Bohren C, Huffmann D. Absorption and scattering of light by small particles. New York: John-Wiley; 1983.

240. Wokaun A, Gordon JP, Liao PF. Radiation damping in surface-enhanced Raman scattering. Phys Rev Lett 1982; 48: 1974–4.

241. Xu H, Aizpurua J, Kall M, Apell P. Electromagnetic contributions to single-molecule sensitivity in surface-enhanced Raman scattering. Phys Rev E 2000; 62: 4318–24.

242. Liao PF, Wokaun A. Lightning rod effect in surface enhanced Raman scattering. J Chem Phys 1982; 76: 751–2.

243. Gersten J, Nitzan A. Electromagnetic theory of enhanced Raman scattering by molecules adsorbed on rough surfaces. J Chem Phys 1980; 73: 3023–37.

244. Jang NH, Suh JS, Moskovits M. Effect of surface geometry on the photochemical reaction of 1,10-phenanthroline adsorbed on silver colloid surface. J Phys Chem B 1997; 101: 8279–85.

245. Lu X, Tuan H-Y, Chen J, Li Z-Y, Korgel BA, Xia Y. Mechanistic studies on the galvanic replacement reaction between multiply twinned particles of Ag and HAuCl$_4$ in an organic medium. J Am Chem Soc 2007; 129: 1733–42.

246. Yin Y, Erdonmez C, Aloni S, Alivisatos AP. Faceting of nanocrystals during chemical transformation: from solid silver spheres to hollow gold octahedral. J Am Chem Soc 2006; 128: 12671–3.

247. Lee I, Morales R, Albiter MA, Zaera F. Synthesis of heterogeneous catalysts with well shaped platinum particles to control reaction selectivity. Proc Natl Acad Sci USA 2008; 105: 15241–6.

248. Fukuoka A, Higashimoto N, Sakamoto Y, Inagaki S, Fukushima Y, Ichikawa M. Preparation and catalysis of Pt and Rh nanowires and particles in FSM-16. Microporous Mesoporous Mater 2001; 48: 171–9.

249. Telkar MM, Rode CV, Chaudhari RV, Joshi SS, Nalawade AM. Shape-controlled preparation and catalytic activity of metal nanoparticles for hydrogenation of 2-butyne-1,4-diol and styrene oxide. Appl Catal A Gen 2004; 273: 11–9.

250. Nikoobakht B, Wang ZL, El-Sayed MA. Self-assembly of gold nanorods. J Phys Chem B 2000; 104: 8635–40.

251. Dimitrov AS, Nagayama K. Continuous convective assembling of fine particles into two-dimensional arrays on solid surfaces. Langmuir 1996; 12: 1303–11.

252. Sau TK, Murphy CJ. Self-assembly patterns formed upon solvent evaporation of aqueous cetyltrimethylammonium bromide-coated gold nanoparticles of various shapes. Langmuir 2005; 21: 2923–9.

253. Dujardin E, Hsin L-B, Wang CRC, Mann S. DNA-driven self-assembly of gold nanorods. Chem Commun 2001; 14: 1264–5.

254. Pan B, Ao L, Gao F, Tian H, He R, Cui D. End-to-end self-assembly and colorimetric characterization of gold nanorods and nanospheres via oligonucleotide hybridization. Nanotechnology 2005; 16: 1776–80.

255. Chang J-Y, Wu H, Chen H, Ling Y-C, Tan W. Oriented assembly of Au nanorods using biorecognition system. Chem Commun 2005; 8: 1092–4.

256. Wang C, Chen Y, Wang T, Ma Z, Su Z. Biorecognition-driven self-assembly of gold nanorods: a rapid and sensitive approach toward antibody sensing. Chem Mater 2007; 19: 5809–11.

257. Caswell KK, Wilson JN, Bunz UHF, Murphy CJ. Preferential end-to-end assembly of gold nanorods by biotin-streptavidin connectors. J Am Chem Soc 2003; 125: 13914–5.

258. Wang Y, Li YF, Wang J, Sanga Y, Huang CZ. End-to-end assembly of gold nanorods by means of oligonucleotide-mercury (II) molecular recognition. Chem Commun 2010; 46: 1332–4.

259. Joseph STS, Ipe BI, Pramod P, Thomas KG. Gold nanorods to nanochains: mechanistic investigations on their longitudinal assembly using α, ω-alkanedithiols and interplasmon coupling. J Phys Chem B 2006; 110: 150–7.

260. Thomas KG, Barazzouk S, Ipe BI, Joseph STS, Kamat PV. Uniaxial plasmon coupling through longitudinal self-assembly of gold nanorods. J Phys Chem B 2004; 108: 13066–8.

261. Ni W, Mosquera RA, Pérez-Juste J, Liz-Marzan LM. Evidence for hydrogen-bonding-directed assembly of gold nanorods in aqueous solution. J Phys Chem Lett 2010; 1: 1181–5.

262. Sudeep PK, Joseph STS, Thomas KG. Selective detection of cysteine and glutathione using gold nanorods. J Am Chem Soc 2005; 127: 6516–7.

263. Zhang S, Kou X, Yang Z, Shi Q, Stucky GD, Sun L, et al. Nanonecklaces assembled from gold rods, spheres, and bipyramids. Chem Commun 2007; 18: 1816–8.

264. Kawamura G, Yang Y, Nogami M. End-to-end assembly of CTAB-stabilized gold nanorods by citrate anions. J Phys Chem C 2008; 112: 10632–6.

265. Orendorff CJ, Hankins PL, Murphy CJ. pH-triggered assembly of gold nanorods. Langmuir 2005; 21: 2022–6.

266. Sreeprasad TS, Samal AK, Pradeep T. One-, two-, and three-dimensional superstructures of gold nanorods induced by dimercaptosuccinic acid. Langmuir 2008; 24: 4589–99.

267. Mitamura K, Imae T, Saito N, Takai O. Fabrication and self-assembly of hydrophobic gold nanorods. J Phys Chem B 2007; 111: 8891–8.

268. Nakashima H, Furukawa K, Kashimura Y, Torimitsu K. Self-assembly of gold nanorods induced by intermolecular interactions of surface-anchored lipids. Langmuir 2008; 24: 5654–8.

269. Walker DA, Gupta VK. Reversible end-to-end assembly of gold nanorods using a disulfide-modified polypeptide. Nanotechnology 2008; 435–603.

270. Chan Y-T, Li S, Moorefield CN, Wang P, Shreiner CD, Newkome GR. Self-assembly, disassembly, and reassembly of gold nanorods mediated by bis(terpyridine)-metal connectivity. Chem Eur J 2010; 16: 4164–8.

271. Correa-Duarte MA, Pérez-Juste J, Sánchez-Iglesias A, Giersig M, Liz-Marzán LM. Aligning Au nanorods by using carbon nanotubes as templates. Angew Chem Int Ed 2005; 44: 4375.–8

272. Correa-Duarte MA, Liz-Marzán LM. Carbon nanotubes as templates for one-dimensional nanoparticle assemblies. J Mater Chem 2006; 16: 22–5.

273. Khanal BP, Zubarev ER. Rings of nanorods. Angew Chem Int Ed 2007; 46: 2195–8.

274. Kumar VRR, Samal AK, Sreeprasad TS, Pradeep T. Gold nanorods grown on microgels leading to hexagonal nanostructures. Langmuir 2007; 23: 8667–9.

275. Das M, Mordoukhovski L, Kumacheva E. Sequestering gold nanorods by polymer microgels. Adv Mater 2008; 20: 2371–5.

276. Wang C, Chen Y, Wang T, Ma Z, Su Z. Monodispersed gold nanorod-embedded silica particles as novel Raman labels for biosensing. Adv Funct Mater 2008; 18: 355–61.

277. Mieszawska AJ, Slawinski GW, Zamborini FP. Directing the growth of highly aligned gold nanorods through a surface chemical amidation reaction. J Am Chem Soc 2006; 128: 5622–3.

278. Honda K, Niidome Y, Nakashima N, Kawazumi H, Yamada S. End-to-end assemblies of gold nanorods adsorbed on a glass substrate modified with polyanion polymers. Chem Lett 2006; 35: 854–5.

279. Zhang X, Imae T. Perpendicular superlattice growth of hydrophobic gold nanorods on patterned silicon substrates via evaporation-induced self-assembling. J Phys Chem C 2009; 113: 5947–51.

280. Zareie MH, Xu X, Cortie MB. In situ organization of gold nanorods on mixed self-assembled-monolayer substrates. Small 2007; 3: 139–45.

281. Fava D, Nie Z, Winnik MA, Kumacheva E. Evolution of self-assembled structures of polymer-terminated gold nanorods in selective solvents. Adv Mater 2008; 20: 4318–22.

282. Nie Z, Fava D, Kumacheva E, Zou S, Walker GC, Rubinstein M. Self-assembly of metal-polymer analogues of amphiphilic tri-block copolymers. Nat Mater 2007; 6: 609–14.

283. Nie Z, Fava D, Rubinstein M, Kumacheva E. Supramolecular assembly of gold nanorods end-terminated with polymer pom-poms: effect of pom-pom structure on the association modes. J Am Chem Soc 2008; 130: 3683–9.

284. Yun S, Park Y-K, Kim SK, Park S. Linker-molecule-free gold nanorod layer-by-layer films for surface-enhanced Raman scattering. Anal Chem 2007; 79: 8584–9.

285. Nakashima H, Furukawa K, Kashimura Y, Torimitsu K. Anisotropic assembly of gold nanorods assisted by selective ion recognition of surface-anchored crown ether derivatives. Chem Commun 2007; 10: 1080–2.

286. Grzelczak M, Rodríguez-González B, Pérez-Juste J, Liz-Marzán LM. Quasi-epitaxial growth of Ni nanoshells on Au nanorods. Adv Mater 2007; 19: 2262–6.

287. Jana NR, Gearheart L, Murphy CJ. Wet chemical synthesis of silver nanorods and nanowires of controllable aspect ratio. Chem Commun 2001; 7: 617–8.

288. Pietrobon B, McEachran M, Kitaev V. Synthesis of size controlled faceted pentagonal silver nanorods with tunable plasmonic properties and self-assembly of these nanorods. ACS Nano 2009; 3: 21–6.

289. Tao A, Kim F, Hess C, Goldberger J, He R, Sun Y, et al. Langmuir-Blodgett silver nanowire monolayers for molecular sensing using surface-enhanced Raman spectroscopy. Nano Lett 2003; 3: 1229–33.

290. Tao A, Sinsermsuksakul P, Yang P. Tunable plasmonic lattices of silver nanocrystals. Nat Nanotechnol 2007; 2: 435–40.

291. Bae Y, Kim NH, Kim M, Lee KY, Han SW. Anisotropic assembly of Ag nanoprisms. J Am Chem Soc 2008; 130: 5432–3.

292. Rycenga M, McLellan JM, Xia Y. Controlling the assembly of silver nanocubes through selective functionalization of their faces. Adv Mater 2008; 20: 2416–20.

293. Li L-S, Walda J, Manna L, Alivisatos AP. Semiconductor nanorod liquid crystals. Nano Lett 2002; 2: 557–60.

294. Li L-S, Alivisatos AP. Semiconductor nanorod liquid crystals and their assembly on a substrate. Adv Mater 2003; 15: 408–11.

295. Talapin DV, Shevchenko EV, Murray CB, Kornowski A, Forster S, Weller H. CdSe and CdSe/CdS nanorod solids. J Am Chem Soc 2004; 126: 12984–8.

296. Gupta S, Zhang Q, Emrick T, Russell TP. Self-corralling nanorods under an applied electric field. Nano Lett 2006; 6: 2066–9.

297. Ryan KM, Mastroianni A, Stancil KA, Liu H, Alivisatos AP. Electric-field-assisted assembly of perpendicularly oriented nanorod superlattices. Nano Lett 2006; 6: 1479–82.

298. Ahmed S, Ryan KM. Self-assembly of vertically aligned nanorod supercrystals using highly oriented pyrolytic graphite. Nano Lett 2007; 7: 2480–5.

299. Querner C, Fischbein MD, Heiney PA, Drndic M. Millimeter-scale assembly of CdSe nanorods into smectic superstructures by solvent drying kinetics. Adv Mater 2008; 20: 2308–14.

300. Kang C-C, Lai C-W, Peng H-C, Shyue J-J, Chou P-T. 2D self-bundled CdS nanorods with micrometer dimension in the absence of an external directing process. ACS Nano 2008; 2: 750–6.

301. Carbone L, Nobile C, De Giorgi M, Sala FD, Morello G, Pompa P, et al. Synthesis and micrometer-scale assembly of colloidal CdSe/CdS nanorods prepared by a seeded growth approach. Nano Lett 2007; 7: 2942–50.

302. Ghezelbash A, Koo B, Korgel BA. Self-assembled stripe patterns of CdS nanorods. Nano Lett 2006; 6: 1832–6.

303. He J, Zhang Q, Gupta S, Emrick T, Russell TP, Thiyagarajan P. Drying droplets: a window into the behavior of nanorods at interface. Small 2007; 3: 1214–7.

304. Zhuang J, Shaller AD, Lynch J, Wu H, Chen O, et al. Cylindrical superparticles from semiconductor nanorods. J Am Chem Soc 2009; 131: 6084–5.

305. Salant A, Amitay-Sadovsky E, Banin U. Directed self-assembly of gold-tipped CdSe nanorods. J Am Chem Soc 2006; 128: 10006–7.

306. Zhao N, Liu K, Greener J, Nie Z, Kumacheva E. Close-packed superlattices of side-by-side assembled Au-CdSe nanorods. Nano Lett 2009; 9: 3077–81.

307. Petroski JM, Green TC, El-Sayed MA. Self-assembly of platinum nanoparticles of various size and shape. J Phys Chem A 2001; 105: 5542–7.

308. Ren J, Tilley RD. Preparation, self-assembly, and mechanistic study of highly monodispersed nanocubes. J Am Chem Soc 2007; 129: 3287–91.

309. Demortière A, Launois P, Goubet N, Albouy PA, Petit C. Shape-controlled platinum nanocubes and their assembly into two-dimensional and three-dimensional superlattices. J Phys Chem B 2008; 112: 14583–92.

310. Chen M, Kim J, Liu JP, Fan H, Sun S. Synthesis of FePt nanocubes and their oriented self-assembly. J Am Chem Soc 2006; 128: 7132–3.

311. Niu W, Li Z-Y, Shi L, Liu X, Li H, Han S, et al. Seed-mediated growth of nearly monodisperse palladium nanocubes with controllable sizes. Cryst Growth Des 2008; 8: 4440–4.

312. Umar AA, Oyama M. Synthesis of palladium nanobricks with atomic-step defects. Cryst Growth Des 2008; 8: 1808–11.

313. Zhang Q, Xie J, Yang J, Lee JY. Monodisperse icosahedral Ag, Au, and Pd nanoparticles: size control strategy and superlattice formation. ACS Nano 2009; 3: 139–48.

314. Sajanlal PR, Pradeep T. Magnetic mesoflowers: synthesis, assembly, and magnetic properties. J Phys Chem C 2010; 114: 16051–9.

315. Larsen TH, Sigman M, Ghezelbash A, Doty RC, Korgel BA. Solventless synthesis of copper sulfide nanorods by thermolysis of a single source thiolate-derived precursor. J Am Chem Soc 2003; 125: 5638–9.

316. Saunders AE, Ghezelbash A, Smilgies D-M, Sigman MB, Korgel BA. Columnar self-assembly of colloidal nanodisks. Nano Lett 2006; 6: 2959–63.

317. Zhuang Z, Peng Q, Zhang B, Li Y. Controllable synthesis of Cu2S nanocrystals and their assembly into a superlattice. J Am Chem Soc 2008; 130: 10482–3.

318. Zhang H, Zhang Y, Yu J, Yang D. Phase-selective synthesis and self-assembly of monodisperse copper sulfide nanocrystals. J Phys Chem C 2008; 112: 13390–4.

319. Du X-S, Mo M, Zheng R, Lim S-H, Meng Y, Mai Y-W. Shape-controlled synthesis and assembly of copper sulfide nanoparticles. Cryst Growth Des 2008; 8: 2032–5.

320. Liu C, Masuda Y, Wu Y, Takai O. A simple route for growing thin films of uniform ZnO nanorod arrays on functionalized Si surfaces. Thin Solid Films 2006; 503: 110–4.

321. Chen Z, Gao L. A facile route to ZnO nanorod arrays using wet chemical method. J Cryst Growth 2006; 293: 522–7.

322. Liu DF, Xiang YJ, Wu XC, Zhang ZX, Liu LF, Song L, et al. Periodic ZnO nanorod arrays defined by polystyrene microsphere self-assembled monolayers. Nano Lett 2006; 6: 2375–8.

323. Lee Y-J, Sounart TL, Liu J, Spoerke ED, McKenzie BB, Hsu JWP, et al. Tunable arrays of ZnO nanorods and nanoneedles via seed layer and solution chemistry. Cryst Growth Des 2008; 8: 2036–40.

324. Izaki M, Watanabe M, Aritomo H, Yamaguchi I, Asahina S, Shinagawa T, et al. Zinc oxide nano-cauliflower array with room temperature ultraviolet light emission. Cryst Growth Des 2008; 8: 1418–21.

325. Pradhan N, Efrima S. Supercrystals of uniform nanorods and nanowires, and the nanorod-to-nanowire oriented transition. J Phys Chem B 2004; 108: 11964–70.

326. Li Y, Li X, Yang C, Li Y. Ligand-controlling synthesis and ordered assembly of ZnS nanorods and nanodots. J Phys Chem B 2004; 108: 16002–11.

327. Batabyal SK, Basu C, Das AR, Sanyal GS. Self-assembly of tellurium nanorods. Proceedings of 5th IEEE Conference on Nanotechnology 2005; 2: 627–30.

328. Tang Z, Wang Y, Shanbhag S, Giersig M, Kotov NA. Spontaneous transformation of CdTe nanoparticles into angled Te nanocrystals: from particles and rods to checkmarks, X-marks, and other unusual shapes. J Am Chem Soc 2006; 128: 6730–6.

329. Shanbhag S, Tang Z, Kotov NA. Self-organization of Te nanorods into V-shaped assemblies: a Brownian dynamics study and experimental insights. ACS Nano 2007; 1: 126–32.

330. Yuan J, Gao H, Schacher F, Xu Y, Richter R, Tremel W, et al. Alignment of tellurium nanorods via a Magnetization-Alignment-Demagnetization ("MAD") process assisted by an external magnetic field. ACS Nano 2009; 3: 1441–50.

331. Dimitrijevic NM, Saponjic ZV, Rabatic BM, Rajh T. Assembly and charge transfer in hybrid TiO2 architectures using biotin-avidin as a connector. J Am Chem Soc 2005; 127: 1344–5.

332. Yang C, Yang Z, Gu H, Chang CK, Gao P, Xu B. Facet-selective 2D self-assembly of TiO2 nanoleaves via supramolecular interactions. Chem Mater 2008; 20: 7514–20.

333. Huang T, Zhao Q, Xiao J, Qi L. Controllable self-assembly of PbS nanostars into ordered structures: close-packed arrays and patterned arrays. ACS Nano 2010; 4: 4707–16.

334. Li M, Schnablegger H, Mann S. Coupled synthesis and self-assembly of nanoparticles to give structures with controlled organization. Nature 1999; 402: 393–5.

335. Kim F, Kwan S, Akana J, Yang P. Langmuir-Blodgett nanorods assembly. J Am Chem Soc 2001; 123: 4360–1.

336. Si R, Zhang Y-W, You L-P, Yan C-H. Rare-earth oxide nanopolyhedra, nanoplates, and nanodisks. Angew Chem Int Edit 2005; 44: 3256–60.

337. Zhang Y-W, Sun X, Si R, You L-P, Yan C-H. Single-crystalline and monodisperse LaF3 triangular nanoplates from a single-source precursor. J Am Chem Soc 2005; 127: 3260–1.

338. Mai H-X, Zhang Y-W, Si R, Yan Z-G, Sun L-D, You L-P, et al. High-quality sodium rare-earth fluoride nanocrystals: controlled synthesis and optical properties. J Am Chem Soc 2006; 128: 6426–36.

339. Si R, Zhang Y-W, Zhou H-P, Sun L-D, Yan C-H. Controlled-synthesis, self-assembly behavior, and surface-dependent opti-

cal properties of high-quality rare-earth oxide nanocrystals. Chem Mater 2007; 19: 18–27.

340. Mai L, Gu Y, Han C, Hu B, Chen W, Zhang P, et al. Orientated Langmuir-Blodgett assembly of VO_2 nanowires. Nano Lett 2009; 9: 826–30.

341. Zheng RK, Gu H, Xu B, Fung KK, Zhang XX, Ringer SP. Self-assembly and self-orientation of truncated octahedral magnetite nanocrystals. Adv Mater 2006; 18: 2418–21.

342. Qi H, Chen Q, Wang M, Wen M, Xiong J. Study of self-assembly of octahedral magnetite under an external magnetic field. J Phys Chem C 2009; 113: 17301–5.

343. Liu X, McCandlish EF, McCandlish LE, Mikulka-Bolen K, Ramesh R, Cosandey F, et al. Single-crystal-like materials by the self-assembly of cube-shaped lead zirconate titanate (PZT) microcrystals. Langmuir 2005; 21: 3207–12.

344. Wang J, Khoo E, Lee PS, Ma J. Synthesis, assembly, and electrochromic properties of uniform crystalline WO_3 nanorods. J Phys Chem C 2008; 112: 14306–12.

345. Zocher H. Spontaneous structure formation in sols; a new kind of anisotropic liquid media. Anorg Allg Chem 1925; 147: 91–110.

346. Zocher H, Heller W. Iridescent strata produced by the slow hydrolysis of iron chloride. Anorg Allg Chem 1930; 186: 75–96.

347. Watson JHL, Cardell RR, Heller W. The internal structure of colloidal crystals of β-FeOOH and remarks on their assemblies in Schiller layers. J Phys Chem 1962; 66: 1757–63.

348. Maeda H, Maeda Y. Atomic force microscopy studies for investigating the smectic structures of colloidal crystals of β-FeOOH. Langmuir 1996; 12: 1446-52.

349. Liao H, Hafner JH. Gold nanorod bioconjugates. Chem Mater 2005; 17: 4636–41.

350. Pissuwan D, Valenzuela SM, Killingsworth MC, Xu X, Cortie MB. Targeted destruction of murine macrophage cells with bioconjugated gold nanorods. J Nanopart Res 2007; 9: 1109–24.

351. Takahashi H, Niidome Y, Yamada S. Controlled release of plasmid DNA from gold nanorods induced by pulsed near-infrared light. Chem Commun 2005: 2247–9.

352. Chen J, Yang M, Zhang Q, Cho EC, Cobley CM, Kim C, et al. Gold nanocages: a novel class of multifunctional nanomaterials for theranostic applications. Adv Func Mat 2010; 20: 3684–94.

353. Chen J, Saeki F, Wiley BJ, Cang H, Cobb MJ, Li Z-Y, et al. Gold nanocages: bioconjugation and their potential use as optical imaging contrast agents. Nano Lett 2005; 5: 473–7.

354. Au L, Zhang Q, Cobley CM, Gidding M, Schwartz AG, Chen J, et al. Quantifying the cellular uptake of antibody-conjugated Au nanocages by two-photon microscopy and inductively coupled plasma mass spectrometry. ACS Nano 2009; 4: 35–42.

355. Skrabalak SE, Chen J, Sun Y, Lu X, Au L, Cobley CM, et al. Gold nanocages: synthesis, properties, and applications. Adv Mater 2007; 19: 3177–84.

356. Au L, Zheng D, Zhou F, Li Z-Y, Li X, Xia Y. A quantitative study on the photothermal effect of immuno gold nanocages targeted to breast cancer cells. ACS Nano 2008; 2: 1645–52.

357. Hrelescu C, Sau TK, Rogach AL, Jackel F, Feldmann J. Single gold nanostars enhance Raman scattering. Appl Phys Lett 2009; 94: 153113 1–3.

358. Hu M, Petrova H, Chen J, McLellan JM, Siekkinen AR. Ultrafast laser studies of the photothermal properties of gold nanocages. J Phys Chem B 2006; 110: 1520–4.

359. Liao H, Nehl CL, Hafner JH. Biomedical applications of plasmon resonant metal nanoparticles. Nanomedicine 2006; 1: 201–8.

360. Skrabalak SE, Au L, Lu X, Li X, Xia Y. Gold nanocages for cancer detection and treatment. Nanomedicine (London) 2007; 2: 657–68.

361. Huang X, El-Sayed IH, Qian W, El-Sayed MA. Cancer cell imaging and photothermal therapy in the near-infrared region by using gold nanorods. J Am Chem Soc 2006; 128: 2115–20.

362. Mulvihill M, Tao A, Benjauthrit K, Arnold J, Yang P. Surface-enhanced Raman spectroscopy for trace arsenic detection in contaminated water. Angew Chem Int Ed 2008; 47: 6456–60.

363. Zou X, Dong S. Surface-enhanced Raman scattering studies on aggregated silver nanoplates in aqueous solution. J Phys Chem B 2006; 110: 21545–50.

364. Wang Y, Zou X, Ren W, Wang W, Wang E. Effect of silver nanoplates on Raman spectra of p-aminothiophenol assembled on smooth macroscopic gold and silver surface. J Phys Chem C 2007; 111: 3259–65.

365. Mock JJ, Barbic M, Smith DR, Schultz DA, Schultz S. Shape effects in plasmon resonance of individual colloidal silver nanoparticles. J Chem Phys 2002; 116: 6755–9.

366. Hao E, Schatz GC. Electromagnetic fields around silver nanoparticles and dimers. J Chem Phys 2004; 120: 357–66.

367. Xie J, Zhang Q, Lee JY, Wang DIC. The synthesis of SERS-active gold nanoflower tags for in vivo applications. ACS Nano 2008; 2: 2473–80.

368. Rex M, Hernandez FE, Campiglia AD. Pushing the limits of mercury sensors with gold nanorods. Anal Chem 2005; 78: 445–51.

369. Maier SA, Kik PG, Atwater HA, Meltzer S, Harel E, Koel BE, et al. Local detection of electromagnetic energy transport below the diffraction limit in metal nanoparticle plasmon waveguides. Nat Mater 2003; 2: 229–32.

370. Sanyal A, Bala T, Ahmed S, Singh A, Piterina AV, McGloughlin TM, et al. Water dispersible semiconductor nanorod assemblies via a facile phase transfer and their application as fluorescent biomarkers. J Mater Chem 2009; 19: 8974–81.

371. Aslan K, Lakowicz JR, Geddes CD. Plasmon light scattering in biology and medicine: new sensing approaches, visions and perspectives. Curr Opin Chem Biol 2005; 9: 538–44.

372. Yu C, Irudayaraj J. Quantitative evaluation of sensitivity and selectivity of multiplex nanoSPR biosensor assays. Biophys J 2007; 93: 3684–92.

373. Yu C, Nakshatri H, Irudayaraj J. Identity profiling of cell surface markers by multiplex gold nanorod probes. Nano Lett 2007; 7: 2300–6.

374. Huang X-J, Li C-C, Gu B, Kim J-H, Cho S-O, Chio Y-K. Controlled molecularly mediated assembly of gold nanooctahedra for a glucose biosensor. J Phys Chem C 2008; 112: 3605–11.

375. Wei Q, Hirota K, Tajima K, Hashimoto K. Design and synthesis of TiO_2 nanorod assemblies and their application for photovoltaic devices. Chem Mater 2006; 18: 5080–7.

376. Ju X, Feng W, Varutt K, Hori T, Fujii A, Ozaki M. Fabrication of oriented ZnO nanopillar self-assemblies and their application for photovoltaic devices. Nanotechnology 2008; 19: 435706 1–6.

*Thalappil Pradeep
DST Unit of Nanoscience (DST UNS)
Department of Chemistry
Indian Institute of Technology Madras
Chennai 600 036, India
Fax: + 91-44 2257-0545
Email: pradeep@iitm.ac.in

Abbreviations

1D	One-dimensional
2D	Two-dimensional
3D	Three-dimensional
APTES	Aminopropyltriethoxysilane
AuNF	Gold nanoflower
bcc	Body centered cubic
BSA	Bovine serum albumin
BSPP	Bis(p-sulfonatophenyl) phenylphosphine dihydrate dipotassium
BT	Benzenethiol
ccp	Cubic close packing
CNT	Carbon nanotube
CTAB	Cetyltrimethylammonium bromide
DDA	Discrete dipole approximation
DDAB	Didodecyldimethylammonium bromide
DMF	N,N-dimethylformamide
DMSA	Dimercaptosuccinic acid
DPPTE	1,2-dipalmitoyl-sn-glycero-3- phosphothioethanol
EB	Trans-2,2′-ethylene 4, 4′-bipyridyl
EDAX	Energy dispersive analysis of X-rays
EGFR	Epidermal growth factor receptor
EQEs	External quantum efficiency
fcc	Face-centered cubic
FESEM	Field-emission scanning electron microscopy
FF	Fill factor
GISAX	Grazing-incidence small-angle X-ray scattering
GNR	Gold nanorod
GOx	Glucose oxidase
hcp	Hexagonal close packing
HDT	Hexadecanethiol
HEPES	4-(2-hydroxyethyl)-1-piperazineethanesulfonic acid
HF	Hydrofluoric acid
HPA	Hexylphosphonic acid
HRTEM	High-resolution transmission electron microscopy
HOPG	Highly oriented pyrolytic graphite
Ig	Immunoglobulin
ITO	Indium tin oxide
LB	Langmuir-Blodgett
LSP	Longitudinal surface plasmon
LSPR	Localized surface plasmon resonance
MCC	Monolayer colloidal crystals
MDA	Mercaptodecanoic acid
MF	Mesoflower
MHA	Mercaptohexadecanoic acid
MPS	Mercaptopropyltrimethoxysilane
MPTMS	Mercaptopropyltri-methoxysilane
MUA	11-mercaptoundecanoic acid
MWNT	Multi-walled carbon nanotube
ND	Nanodot
NDBs	Nanodumbbells
NIR	Near-infrared
NLO	Non-linear optical
ncp	Non-close-packed
NW	Nanowire
ODPA	Octadecylphosphonic acid
OCT	Optical coherence tomography
ODS	Octadecyltrimethoxysilane
ODT	Octadecanethiol
PAM	Polyacrylamide
PAMAM	Polyamidoamine
PCE	Power conversion efficiency
PDDA	Poly-(diallyldimethylammonium) chloride
PEG	Poly(ethylene glycol)
PNIPAm	Poly(N-isopropyl acrylamide)
ppt	Parts-per-trillion
PS	Polystyrene
PSS	Polystyrene sulfonate
PVP	Poly(vinylpyrrolidone)
SAED	Selected area electron diffraction
SAM	Self-assembled monolayer
SAXS	Small angle X-ray scattering
SCs	Supercrystals
SEM	Scanning electron microscopy
SERS	Surface-enhanced Raman spectroscopy
SLs	Side ligands
SPR	Surface plasmon resonance
STEM	Scanning transmission electron
TA	Thioctic acid
TAA	Thioacetamide
TDPA	Tetradecylphosphonic acid
TEM	Transmission electron microscopy
TLs	Tip ligands
TOP	Tri-n-octylphosphine
TPL	Two-photon luminescence
TSP	Transverse surface plasmon
WHO	World health organization